

Vasileios Ramopoulos

**Energy-efficient, scalable and
modular industrial microwave
applicator for high temperature
alkaline hydrolysis of PET**



Scientific
Publishing

Vasileios Ramopoulos

**Energy-efficient, scalable and modular industrial
microwave applicator for high temperature alkaline
hydrolysis of PET**

Karlsruher Forschungsberichte aus dem
Institut für Hochleistungsimpuls- und Mikrowellentechnik

Herausgeber: Prof. Dr.-Ing. John Jelonnek

Band 16

Energy-efficient, scalable and modular industrial microwave applicator for high temperature alkaline hydrolysis of PET

by
Vasileios Ramopoulos

Karlsruher Institut für Technologie
Institut für Hochleistungsimpuls- und Mikrowellentechnik

Energy-efficient, scalable and modular industrial microwave
applicator for high temperature alkaline hydrolysis of PET

Zur Erlangung des akademischen Grades eines Doktors der Ingenieurwissen-
schaften von der KIT-Fakultät für Elektrotechnik und Informationstechnik des
Karlsruher Instituts für Technologie (KIT) genehmigte Dissertation

von Vasileios Ramopoulos

Tag der mündlichen Prüfung: 21. Januar 2021
Erster Gutachter: Prof. Dr.-Ing. John Jelonnek
Zweiter Gutachter: Prof. Dr.-Ing. Thorsten Gerdes

Diese Publikation wurde im Rahmen des Fördervorhabens 16TOA022 mit
Mitteln des Bundesministeriums für Bildung und Forschung im Open Access
bereitgestellt.

Impressum



Karlsruher Institut für Technologie (KIT)
KIT Scientific Publishing
Straße am Forum 2
D-76131 Karlsruhe

KIT Scientific Publishing is a registered trademark
of Karlsruhe Institute of Technology.
Reprint using the book cover is not allowed.

www.ksp.kit.edu



*This document – excluding parts marked otherwise, the cover, pictures and graphs –
is licensed under a Creative Commons Attribution-Share Alike 4.0 International License
(CC BY-SA 4.0): <https://creativecommons.org/licenses/by-sa/4.0/deed.en>*



*The cover page is licensed under a Creative Commons
Attribution-No Derivatives 4.0 International License (CC BY-ND 4.0):
<https://creativecommons.org/licenses/by-nd/4.0/deed.en>*

Print on Demand 2023 – Gedruckt auf FSC-zertifiziertem Papier

ISSN 2192-2764
ISBN 978-3-7315-1099-4
DOI 10.5445/KSP/1000131787

Foreword of the Editor

Polyethylene terephthalate (PET) is one of the most widely used plastics, with an annual primary global production of 33 million tons in 2015. However, only a small fraction of the used and mostly contaminated PET material is recycled to date. Even more, today the process of recycling leads to a steady deterioration in quality of the material. Excluding a costly color presorting process, the only known recycling process of contaminated PET is the chemical recycling. However, this is a costly and energy-intensive process. On the other hand, alkaline hydrolysis of PET would be a promising recycling method. In alkaline hydrolysis, PET is hydrolyzed into sodium hydroxide NaOH, producing the disodium salt $\text{Na}_2[\text{PTA}]$ and monoethyleneglycol. New PET can be produced from the two resulting substances the para-terephthalic acid (PTA) and the monoethylene glycol (MEG). In this frame, the microwave-assisted alkaline hydrolysis of PET would add significantly to an energy efficient recycling process. By using dielectric heating, a significant reduction of the reaction time from about 3 hours to less than 10 minutes is possible while, at the same time, the reaction takes place at lower temperatures. This work presented here bases on a simple microwave applicator at laboratory scale that already existed. Developed by the company Gr3n, two household microwave ovens were modified and connected to each other.

The aim of this work is to develop an energy-efficient modular-type and scalable microwave applicator to support the depolymerisation reaction, with a minimum capacity of 12.5 kg/h PET and a continuous operation by means of an Archimedean screw. To enable an efficient microwave process, all materials involved in the reaction are dielectrically characterized. The dielectric properties are systematically used in the design of the microwave applicator. A systematic investigation of the chemical reaction is done to make a statement regarding the reaction enthalpy. In order to regulate the microwave applicator, the modelling of the reaction kinetics is done. With the help of that a highly efficient industrial microwave reactor could be proposed in this work.

In frame of his work, Vasileios Ramopoulos presents several different innovations. In the area of the dielectric measurements an innovative, in-situ dual mode resonator approach is presented which, in combination with numerical simulation, enables a significant expansion of the measurements ranges for materials with different dielectric constants and loss factors. By using a suitable sample container, measurements above the boiling point are realized. In the area of calorimetric measurements, a microwave calorimeter is presented that enable the determination of the reaction enthalpy and the heat capacity. The modelling of the reaction kinetics is also presented based on the measured dielectric losses. Finally, a novel industrial scale microwave applicator at 2.45 GHz with homogeneous field distribution is proposed.

Kurzfassung

Alleine im Jahr 2017 wurden 4,2 Millionen Tonnen Kunststoffabfälle von Europa, den USA und Kanada in Entwicklungsländer, wie zu Beispiel Malaysia, Indonesien und Indien exportiert, davon waren ca. 330 Kilotonnen PET (Polyethylenterephthalat). Meistens sind diese Zielländer nicht in der Lage diese Kunststoffabfälle sinnvoll weiterzuverarbeiten. Diese werden oft deponiert, landen im Meer oder werden durch Verbrennung energetisch verwertet. Dies führt zu einer nachhaltigen Beeinträchtigung des Lebensraums der Tiere und des Menschen. Die chemische Rückgewinnung der bei der Herstellung von PET verwendeten Monomere stellt die einzige Möglichkeit dar, PET vollständig zu recyceln. Insbesondere die alkalische Hydrolyse ist das einzige Recyclingverfahren, das auch für stark kontaminiertes PET wie Verpackungsfolien, PET-Flaschen oder Landwirtschaftsfolien geeignet ist [1]. Die Reaktionsprodukte der alkalischen Hydrolyse könne direkt zur Herstellung von neuem, reinem PET verwendet werden. Da dieses Verfahren einen langwierigen und energieintensiven Prozess darstellt, wird es nur selten eingesetzt. Im Unterschied dazu ist das Mikrowellenunterstützte Recycling (Depolymerisation) von PET eine vielversprechende Technologie, die die Reaktionszeit von ca. drei Stunden auf weniger als zehn Minuten reduziert. Dieses Verfahren macht das chemische PET- Recycling zum ersten Mal wirtschaftlich rentabel und attraktiv für die industrielle Anwendung.

In dieser Arbeit wurde ein absolut neuer und fortschrittlicher Mikrowellen-Applikator zur PET- Depolymerisation mittels Mikrowellen entwickelt. Der Applikator wurde für den industriellen Gebrauch im ISM- Frequenzband von 2,45 GHz ausgelegt. Bei der Entwicklung wurde Wert auf den modularen und skalierbaren Aufbau sowie die Energie-Effizienz des Systems gelegt. Die homogene Erwärmung des Reaktionsgemisches wurde mittels eines innovativen Wellenleiternetzwerks zur Verteilung der Mikrowellenleistung ermöglicht. Dieses Verteilnetzwerkkonzept ist konfigurierbar und lässt sich mit moderatem Aufwand auf andere Durchmesser als auch Längen des zu beheizenden Reaktors anpassen. Eine an das elektromagnetische Feld

angepasste archimedische Schraube erlaubt einen Durchlaufbetrieb mit flüssigen Proben bzw. Dispersionen. Der konzipierte Applikator erlaubt einen Durchsatz von mehr als 100 Tonnen PET bzw. 750 Tonnen Reaktionsgemisch pro Jahr im Dauerbetrieb und erreicht einen Wirkungsgrad von mindestens 97 % bezogen auf die installierte Mikrowellenleistung, wodurch er besonders energieeffizient ist. Je nach Anforderungen kann der Applikator modular als Kaskade realisiert werden, um eine längere Heizstrecke bzw. den Einsatz von mehreren Leistungsquellen zu ermöglichen. Um den oben genannten Durchsatz zu erreichen, werden beispielsweise fünf Module benötigt.

Um den Applikator auf die Depolymerisierungsreaktion abzustimmen, ist die genaue Kenntnis der dielektrischen Parameter des Reaktionsgemisches notwendig. Dafür wurde ein innovatives Messsystem, das auf einem Dual-Mode Resonator basiert, entwickelt. Dieses System beruht auf der Störkörpermethode, die eigentlich nur für kleine Störungen, d.h. für kleine Proben mit geringen dielektrischen Verlusten, geeignet ist. Aufgrund des Dual-Mode-Ansatzes und einer vollständigen numerischen 3D-Simulation des inversen Problems wird die Störkörpermethode erstmals für Proben mit sehr hohen Verlusten eingesetzt und ermöglicht die Vermessung von Flüssigkeiten mit hohen Verlusten unter Druck bis zu 20 bar. Es macht den Weg frei für in-situ temperatur- und zeitabhängige dielektrische und kalorimetrische Messungen im Mikrowellenbereich. Es lassen sich mittels Mikrowellenerwärmung verschiedene definierte Heizprofile in-situ untersuchen. Durch die kalorimetrischen Messungen ist eine Aussage bezüglich des exothermen oder endothermen Verhaltens der Reaktionskinetik möglich. Dies ist wichtig für die spätere Auslegung der installierten mikrowellenbasierten Leistungsquellen sowie des benötigten Kühlsystems für den finalen Mikrowellen-Applikator.

Des Weiteren wurde in dieser Arbeit ein Modell zur Reaktionskinetik unter Verwendung des dielektrischen Verlustfaktors entwickelt. Dieses Modell ermöglicht die spätere Optimierung der Prozessparameter.

Abstract

In 2017, 4.2 million tons of plastic waste, of which approximately 330 kilotons were PET (polyethylene terephthalate), were exported from Europe, the United States and Canada to developing countries such as Malaysia, Indonesia and India. Most of these target countries of plastic waste are unable to process them sensibly. These plastic wastes are often landfilled, end up in the ocean or are burned for energy. This leads to a continuous disturbance of the habitat of animals and humans. Chemical recycling of PET is the only way to fully recover the monomers used in the manufacture of PET. In particular, the alkaline hydrolysis is the only recycling process that is also suitable for highly contaminated PET such as packaging films, PET bottles or agricultural films [1]. The reaction products of the alkaline hydrolysis can be used directly for the production of new, virgin PET. Since this procedure is a lengthy and energy-intensive process, it is rarely used. In contrast to this, microwave-assisted recycling (depolymerization) of PET is a promising technology that reduces the processing time from around three hours to less than ten minutes. This process makes chemical PET recycling economically profitable and attractive for the industrial application.

In this work, a new microwave applicator for PET depolymerization on an industrial scale is demonstrated. The applicator is designed for industrial use on the ISM band frequency of 2.45 GHz. During the development, the focus is put on the modular and scalable design as well as the energy efficiency of the system. The homogeneous heating of the reaction mixture is made possible by an innovative microwave power distribution network. This distribution network concept is configurable. Both the diameter and the length can be adapted with little effort, depending on the dimensions of the reactor to be heated. An Archimedean screw adapted to the microwave field allows continuous operation with liquid samples and dispersions. The applicator enables a throughput of more than 100 tons of PET or 750 tons of reaction mixture per year in continuous operation. The power absorbed in the sample is more than 97 % compared to the installed microwave power, which makes it

very energy-efficient. Depending on the requirements, the applicator can be implemented as a modular cascade to enable a longer heating section or the use of several power sources. For example, five modules are required to achieve the throughput mentioned above.

To adapt the applicator to the depolymerization reaction, a precise knowledge of the dielectric parameters of the reaction mixture is necessary. A dual-mode cylindrical cavity is developed for this purpose. This system relies on the cavity perturbation method, which is actually only suitable for small perturbations, i.e. small samples with low dielectric losses. The dual-mode approach in combination with a full 3D numerical solution of the inverse problem allows the measurements of liquids with high losses under pressures up to 20 bar. At the same time, it allows in-situ temperature and time dependent dielectric and calorimetric measurements at 2.45 GHz. By means of microwave heating different defined heating profiles can be investigated in-situ. The calorimetric measurements provide information about the exothermic or endothermic behavior of the reaction kinetics. This is important for the later design of the installed microwave power sources as well as for the required cooling of the microwave final applicator.

Furthermore, in this thesis a model for the reaction kinetics using the dielectric loss tangent was developed. This model allows the optimization of the process parameters.

Contents

Foreword of the Editor	i
Kurzfassung	iii
Abstract	v
List of figures	xi
List of tables	xvii
List of abbreviations.....	xix
List of used symbols	xxi
1 Introduction	1
1.1 Dielectric heating using microwave power.....	1
1.2 Motivation	2
1.3 Objectives and structure of this work	5
2 Fundamentals.....	9
2.1 Definition of dielectric properties.....	9
2.1.1 Dielectric mixing rules	12
2.2 Dielectric measurement methods at microwave frequencies	13
2.2.1 Reflection method	13
2.2.2 Transmission-Reflection method.....	14
2.2.3 Resonance method.....	15
2.2.4 Microwave cavity	16
2.3 Alkaline hydrolysis of PET.....	24
3 Dielectric and calorimetric measurement systems.....	27
3.1 In-situ, high pressure and high precision measurement setup.....	27
3.1.1 Design methodology.....	27
3.1.2 Cavity design.....	30
3.1.3 Measurement setup.....	33

3.1.4	Calibration method	35
3.1.5	Error estimation	37
3.2	Microwave calorimetry	40
3.2.1	Measurement setup	41
3.2.2	Calibration method	41
3.2.3	Validation of the system performance	48
3.3	Combined dielectric and calorimetric measurements	52
3.3.1	Measurements setup	52
3.3.2	Automatic calibration and control system	52
3.4	Measurements using the coaxial probe	56
4	Dielectric and calorimetric measurement results	57
4.1	Sample preparation	57
4.2	Dielectric measurement results	58
4.2.1	Dielectric properties of the reaction mixture	58
4.2.2	Dielectric properties of the initial mixture	62
4.2.3	Dielectric properties of reactants measured with coaxial probe	65
4.3	Calorimetric measurement results	69
5	Modelling of the reaction kinetics based on $\tan \delta$	71
5.1	Data preparation for modelling	71
5.2	Reaction model	73
5.3	Verification and errors	79
6	Physical and technical design of an industrial μWave applicator	81
6.1	Concept	81
6.2	Archimedean screw geometry	81
6.3	Energy required for a specific volume	85
6.4	Estimation of the applicator segments	86
6.5	Applicator design	87
6.6	Performance of the fabricated applicator	95
6.6.1	Test set	95
6.6.2	Results	97
6.7	Process optimization	98

7 Conclusion and outlook..... 101

8 Appendix..... 105

Bibliography 111

List of own publications 123

Acknowledgment 125

List of figures

Figure 1.1:	Possible chemical reactions for the depolymerization of PET and the corresponding reaction products	3
Figure 2.1:	Dielectric permittivity over a wide frequency range [32]	11
Figure 2.2:	Mode chart of a cylindrical cavity [43]	17
Figure 2.3:	Normalized unloaded quality factor of a cylindrical resonator for various modes [43].....	20
Figure 2.4:	Calorimetric measurements under microwave heating conditions, proposed by Parker et al. [62]	26
Figure 3.1:	Sideview of cavity E-Field for $\epsilon'_r = 20$ and $\tan \delta = 0$: TE ₁₁₁ (top left) and TM ₀₁₀ (top right), E-Field stretch in the center of the cavity: TE ₁₁₁ (bottom left) and TM ₀₁₀ (bottom right) [64].....	28
Figure 3.2:	Simulated $\Delta f(\epsilon'_r)$ for $\tan \delta = 0.01$ (top) and $Q(\tan \delta)$ for $\epsilon'_r = 40$ (bottom) for a cylindrical sample with 3 mm in diameter in a cavity with 88.5 mm in diameter and a length of 90 mm [64]	29
Figure 3.3:	Dual-mode cavity simulated with CST Microwave Studio [64].....	31
Figure 3.4:	Simulated transmission between port 1 and port 3 of the dual-mode cavity.....	32
Figure 3.5:	Temperature distribution along the MUT by heating with the TM ₀₁₀ mode and taking into account the convection and conduction heat losses calculated with COMSOL multiphysics simulations	33

Figure 3.6:	Block diagram of the dielectric measurements system [64].....	34
Figure 3.7:	Test setup for the dielectric measurements	35
Figure 3.8:	Simulated and measured S_{21} -parameters for the TE_{111} -mode (top) and for the TM_{010} -mode (bottom) [64].....	36
Figure 3.9:	Block diagram of the power measurements system [69].....	41
Figure 3.10:	S-Parameters with excitation at port 1 of the power measurement system from Fig. 3.9	42
Figure 3.11:	S-parameters with excitation at port 2 of the power measurement system from Fig. 3.9	43
Figure 3.12:	Resonator model with the correspondings temperature variables	44
Figure 3.13:	Power calibration methodology	47
Figure 3.14:	Calorimetric monitoring of curing of epoxid resins	50
Figure 3.15:	Block diagram of the measurements system	52
Figure 3.16:	Scheme of the control of the dielectric and calorimetric measurements set up	53
Figure 3.17:	Example of temperature control with optimized PID controller parameters	55
Figure 3.18:	Measurement setup based on commercial coaxial probe HP85070B.....	56
Figure 4.1:	Temperature depending permittivity for all samples according to Table 4.1	59
Figure 4.2:	Temperature dependence of ϵ'_r for sample 'Reaction progress 100 %' according to Table 4.1 incl. re-heating	61
Figure 4.3:	D_p of the sample 'Reaction progress 0 %'	62
Figure 4.4:	Dielectric properties of PET.....	63
Figure 4.5:	Dielectric properties of MEG, H ₂ O and NaOH.....	64

Figure 4.6:	$\tan \delta$ of the unreacted mixture consisting of MEG, H ₂ O, NaOH and PET	65
Figure 4.7:	Measured dielectric loss tangent of MEG for six different temperatures.	65
Figure 4.8:	NaOH solution: loss tangent versus temperature for four NaOH concentrations	67
Figure 4.9:	NaOH, H ₂ O and MEG solution: loss tangent versus temperature for four NaOH concentrations.....	67
Figure 4.10:	Measured and fitted $\tan \delta$ from NaOH with water and MEG at room temperature	68
Figure 4.11:	Time dependence of absorbed power during the depolymerization of PET and of the reaction product according to Table 4.1	70
Figure 5.1:	Loss tangent of the reaction product	71
Figure 5.2:	Temperature dependence of the loss factor during the reaction ($dT/dt = 3 \text{ }^\circ\text{C}/\text{min}$).....	72
Figure 5.3:	Time dependence of the loss factor during the reaction ($dT/dt = 3 \text{ }^\circ\text{C}/\text{min}$).....	72
Figure 5.4:	Temperature dependence of the $\tan \delta$ of the unreacted mixture, reaction product and during the reaction.....	73
Figure 5.5:	Measured and simulated $\tan \delta$ during the reaction at room temperature	74
Figure 5.6:	Temperature dependent $\tan \delta$ of the reaction mixture over the reaction.....	75
Figure 5.7:	Microscope pictures of the PET particles.....	77
Figure 5.8:	Arrhenius plot for the alkaline hydrolysis of PET.....	78
Figure 5.9:	Measured and modelled dielectric properties for three different start reaction mixtures from Table 4.1.....	79

Figure 6.1:	Archimedean screw (left) and its simplified model for the simulations (right) [95].....	82
Figure 6.2:	Simulated relative power absorption as a function of $\tan \delta$ (at 2.46 GHz and $\epsilon'_r = 30$) [95].....	84
Figure 6.3:	Modular design of the microwave reactor (top), temperature profile along the MUT (bottom) [95]	86
Figure 6.4:	Simulated electric field in the cylindrical cavity [95].....	88
Figure 6.5:	Electric field density in a 'short' cylindrical microwave cavity with electric length in z-direction $< \lambda/2$ [95].....	89
Figure 6.6:	Simulated geometry of the power distribution network: center zone (left), side view (right) [95]	90
Figure 6.7:	Electric field distribution of the power distribution network design in azimuthal direction of zone c (upper right); of levels b and d (lower left); of levels a and e (lower right) and in axial direction (upper left) [95].....	91
Figure 6.8:	Simulated reflected power at the input of the power distribution network with and without matching element versus frequency	93
Figure 6.9:	Absorbed power for different ϵ'_r and $\tan \delta = 0.5$ versus frequency	94
Figure 6.10:	$\lambda/4$ filter structure to enable a contactless operation	94
Figure 6.11:	Absorbed power versus frequency for different gap thicknesses of the $\lambda/4$ filter structure.....	95
Figure 6.12:	Fabricated microwave cavity [95].....	96
Figure 6.13:	Simulated and measured S-parameters [95].....	97
Figure 6.14:	Simulated power distribution (left), measured temperature distribution (right) [95].....	98

Figure 6.15:	Temperature profile and reaction progress across the applicator at a reaction temperature of $\leq 180^{\circ}\text{C}$	99
Figure 6.16:	Temperature profile and reaction progress across the applicator at temperatures $\leq 220^{\circ}\text{C}$	100
Figure 8.1:	Measured dielectric properties of MEG using the coaxial probe HP 85070B at three different temperatures in a wide frequency range.....	105
Figure 8.2:	Measured dielectric properties of 5 wt.% NaOH with H_2O mixture using the coaxial probe HP 85070B at three different temperatures in a wide frequency range.....	107

List of tables

Table 2.1:	High frequency dielectric measurement methods and their pros and cons.....	14
Table 3.1:	Measured dielectric properties with the dual-mode approach, coaxial probe HP85070B and the corresponding literature values shown in [43] and [67]	37
Table 3.2:	Comparison between measured and literature values of the specific heat capacity	48
Table 4.1:	Mixture composition at the different reaction steps	57
Table 4.2:	Measured dielectric properties for the mixtures listed in Table 4.1	60
Table 6.1:	Simulated relative power absorption for various screw parameters, scaled to λ for a dielectric material with $\epsilon_r' = 30$ and $\tan \delta = 0.01$ and 1 respectively [95].....	83
Table 6.2:	Specific heat capacity of the various reactants and the corresponding mass in the used reaction mixture.	85
Table 6.3:	Power distribution in the MUT located in the power distribution network [% of the absorbed power] [95].....	92
Table 8.1:	Course of the coefficients and their approximation from the unreacted reaction mixture	108
Table 8.2:	Course of the coefficients and their approximation from the reaction product.	109
Table 8.3:	Course of the coefficients and their approximation from the loss factor during the reaction.....	109

List of abbreviations

MUT	material under test
RF	radio frequency
NaOH	sodium hydroxide
PTA	terephthalic acid
Na ₂ PTA	disodium terephthalate salt
PET	polyethylene terephthalate
MEG	monoethylene glycol
BHET	Bis(2-hydroxyethyl) terephthalate
DMT	dimethyl terephthalate
KOH	potassium hydroxide
TE	transverse electric
TM	transverse magnetic
LR	Lichtenecker Rother
MG	Maxwell Garnett
VNA	vector network analyzer
MWS	microwave studio

List of abbreviations

wt.% weight percent

ISM Industrial, Scientific and Medical

List of used symbols

ϵ	complex dielectric constant
ϵ_0	vacuum permittivity
ϵ_r	relative complex permittivity
ϵ'	dielectric constant
ϵ''	dielectric loss factor
ϵ'_r	relative dielectric constant
ϵ''_r	relative dielectric loss factor
$\tan \delta$	dielectric loss tangent
$\epsilon_{r,eff}$	complex permittivity of the mixture
ϵ_{r,i_n}	complex permittivity of the n-th inclusion
$\epsilon_{r,e}$	complex permittivity of the environment
μ	complex permeability
μ_0	vacuum permeability
μ'_r	real part of relative complex permeability
μ''_r	imagine part of relative complex permeability
P_{abs}	absorbed power
P_{refl}	reflected power

P_{inc}	incident power
P_{trans}	transmitted power
A_n	uncorrelated variables
δ_{A_n}	variances of the random variables A_n
D_p	penetration depth
E	electric field
f	frequency
T	temperature
t	time
V	volume
f	frequency
S_{ij}	ratio of the reflected or transmitted wave at port j to the incident wave at port i
$E_0; E_1$	electric field of the unloaded and the loaded cavity
$H_0; H_1$	magnetic field of the unloaded and the loaded cavity
P_c	power losses at the conducting walls
R_s	surface resistivity of the metal walls
H_t	tangential magnetic field
σ	electric conductivity
σ_{eff}	effective electric conductivity

W_e	stored electric energy
W_m	stored magnetic energy
Q	quality factor of the resonator
Q_c	quality factor of the resonator including power loss due to lossy walls and lossless dielectric
n, m, l	mode index of the resonator
a, b, d	corresponds either to the three dimensions of the rectangular cavity or a and d corresponds to the cavity radius and length
p'_{nm}	root of the derivative of the first kind Bessel function J_{nm}
p_{nm}	root of the first kind Bessel function J_{nm}
k	propagation constant
η	wave impedance in the medium
β	phase constant
Ω_m	complex resonance frequency
h	convection coefficient
q''	heat flux density
q	total heat transfer rate
r_i, r_e	inner and outer radius of the glass tube
R	universal gas constant
R_a	specific gas constant for air
E_a	activation energy

M_a	molar mass of dry air
ρ_a	volumetric mass density of air
c_p	specific heat capacity
e, e_1, e_2	actual, previous and two times before error value
K_P, K_I, K_D	proportional, integral and derivative gains
ζ	LR exponential factor
α	reaction degree
$\kappa(T)$	temperature dependent reaction rate
V_{PET}	fractional volume of PET
V_{L-PET}	fractional volume of MEG, NaOH and H ₂ O
A	Arrhenius constant
N_{As}	surface area of the PET flakes
N_{Ai}	moles of PET repeating units
M	ratio of moles of NaOH and of moles of PET
b_r	reaction rate order
λ	wavelength in medium
c_0	speed of light in vacuum
d_s	Archimedean screw pitch
h_s	Archimedean screw depth
m	mass

1 Introduction

1.1 Dielectric heating using microwave power

Today, the use of microwaves for dielectric heating finds increasing application in heating of materials such as food [2], in microwave assisted chemistry [3], [4], [5], [6] and in drying of materials [7]. The advantage of microwave heating originates from the fact that the heat is generated inside the material volume, so the heating is quick, direct and energy efficient. In particular, materials characterized by low thermal conductivity such as plastics, glass, ceramics and powders can be heated much faster than with conventional methods. Furthermore, microwaves enable the selective heating of mixtures of materials, having different dielectric loss factor. This allows process specific temperature profiles that are impossible to realize in conventional thermal furnaces. Another advantage of microwaves is that workflows at very high temperatures can be realized in cold ovens.

In order to develop energy efficient microwave systems and processes, the detailed knowledge of the dielectric properties of the processed materials at the center heating frequency is a prerequisite. The lack of data on temperature dependent dielectric properties possess barriers for further development as they can be rarely found in literature for the temperature and frequency of interest. Even if such data can be found, very often the reported material differs from the specific material of interest. Therefore, the accurate simulation of processes and microwave applicator demands the precise dielectric characterization of all involved materials. In case the materials exposed to microwave heating pass through irreversible changes, for example in chemical reactions with consecutive change in dielectric properties, the knowledge about the time and temperature history of material's permittivity is essential.

Microwave assisted chemistry is reported to provide numerous advantages, such as remarkable acceleration of the reaction, higher yields under milder reaction conditions and higher product purities [8]. These advantages may be

explained as a combination of thermal effects, such as higher heating rates, superheating (hot spots) and selective absorption of the microwave power from different substances.

1.2 Motivation

Polyethylene terephthalate, PET, is one of the engineering plastics which is widely used as it is showing excellent thermal and mechanical properties, chemical resistance, and transparency. By far the largest application is in the textile industry. Enormous quantities of this material are also consumed in the manufacture of PET films, used in 3D printing, injection molding, food packaging, and especially for the production of water and soft drink bottles. PET is the sixth-most used plastic with a total primary global production of 33 million tons in 2015 [9].

The usual durability of polymers such as PET is, on the one side, desirable for its application. On the other side, it is a threat to the environment when these are disposed after use. Different to the natural polymers, the synthetic polymers are not easily degraded under normal outdoor conditions. They are collected in landfills as waste products [10]. At the same time, discarded polymers represent a huge waste due to the amounts of energy and resources embodied in them [10]. Therefore, the recycling of PET becomes inevitable. The recycling of PET can be realized in many ways: (a) primary recycling refers to the mechanical reprocessing of uncontaminated polymer products into products with equivalent properties; (b) secondary mechanical recycling where the polymer is separated from the various contaminants and can be reprocessed into products with inferior properties; (c) chemical recycling refers to the full recovery of the monomers and (d) energy recovery [11], [12]. The chemical recycling of PET is the only ‘true’ recycling technique, which does not lead to a degradation and it is suitable for contaminated polymer products [12].

The chemical recycling is based on processes such as hydrolysis, methanolysis, glycolysis, ammonolysis and aminolysis [13]. Depending on the reaction chosen, different reaction products are obtained as shown in Fig. 1.1. Until

today, only the glycolysis and methanolysis can be commercially applied for the depolymerization of PET [10].

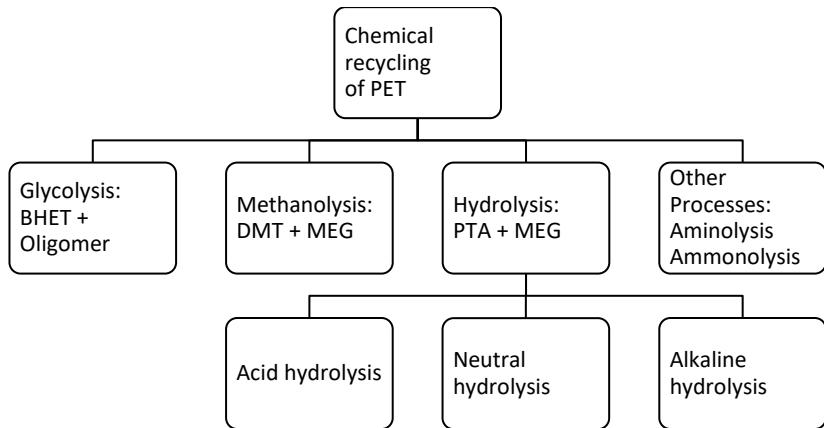


Figure 1.1: Possible chemical reactions for the depolymerization of PET and the corresponding reaction products

The hydrolysis is the only recycling method, which results in base products such as para-terephthalic acid (PTA) and mono-ethylene glycol (MEG), which can be used to produce virgin PET again.

Depending on the catalysts used, a distinction is made between acidic, alkaline and neutral hydrolysis. The acid hydrolysis is mostly realized in the presence of sulphuric acid, nitric or phosphoric acid. This process is very costly due to the demand of the further recycling of large H_2SO_4 amounts and the separation of MEG from sulphuric acid [10]. The neutral hydrolysis is realized with water or steam as catalyst. The main drawback from this reaction is that the products show a low purity [10]. The alkaline hydrolysis is performed with the use of alkaline solution of NaOH or KOH [10]. The alkaline hydrolysis may be carried out with highly contaminated PET and it is much cheaper and faster compared to methanolysis.

Based on above stated, the alkaline hydrolysis of PET is the only interesting recycling method of contaminated post-consumer PET. However, the long reaction time in combination with the high-energy consumption is the main concern of this recycling technique. Because of that, PET material used today is only reused to approximately 10 % but not really recycled or depolymerized. This motivates the investigation of alternative procedures to make the alkaline hydrolysis of PET more time- and energy-efficient. It leads to the microwave-assisted depolymerization of PET that provides a significant acceleration of the reaction process time from about 180 minutes by means of conventional heating, down to less than 10 minutes using microwave heating. Additionally, the microwave assisted depolymerization takes place at lower temperatures and therefore under lower pressure conditions because of the volumetric and selective heating characteristics of microwaves [12]. These facts enable an easier upscaling of a future reactor.

To enable a microwave-assisted reaction process, a suitable process chamber is required. In general, those microwave applicators are still based on the design of Raytheon developed in 1965 [14]. That microwave oven consists of a magnetron [15] as power source and a rectangular cavity of some 40 cm height, 50 cm width and 30 cm depth [14]. The main drawback for industrial application is the difficulty to enable a well-defined and uniform heating of materials, because of the existing cold and hot spots in any microwave oven. This problem of non-uniform heating until now is one of the main obstacles for the commercialization of microwave heating in industrial applications [16]. The main factors, which contribute to this lack of uniform heating, are the geometry of the microwave resonator, the finite penetration depth of the microwaves, the geometry of the material sample, the dielectric properties of the processed material and the feed point of the microwaves compared to the position of the processed material [17]. These factors make it also impossible to get a universal microwave oven for the processing of any dielectric material and geometry.

This motivated the development of various lab scale and industrial scale application specific microwave ovens with the main target to offer more homogeneous field patterns [16], [18], [19] and [20]. In [20] a novel industrial

microwave system is presented, which is based on a patented hexagonal cavity. This geometry provides a significantly increased homogeneity in a large applicator volume [21]. In [22], a ‘Coaxial Wrap-Around TE_{01} Mode Converter’ cavity is based on a TE_{01} waveguide in a circular orientation. The power is coupled into the actual heating cavity through nine radial slots (see Fig. 3 in [22]). Further industrial microwave applicators for both batch and continuous operation are shown in [23], [24] and [25]. In [18] various microwaves ovens are presented, which support the microwave-assisted organic synthesis. Those ovens are based on single and multimode cavities and are partially equipped with mode stirrers, special temperature sensors and pressure vessels to enable well-defined and reproducible heating conditions. These systems are mainly targeted to lab-scale operation.

In the area of microwave assisted PET recycling based on single mode cavities at lab-scale several investigations are on-going [26], [27] and [28]. Most of them are based on commercial single mode microwave reactors developed from CEM corporation [29]. Those investigations were carried out under atmospheric pressure and under higher pressure with samples between 10 ml and 100 ml. However, the main problem for the design of an industrial scale applicator is the restricted penetration depth (in the range of some millimeters) in the reaction mixture and the demand for a continuous operation to meet the economic needs.

1.3 Objectives and structure of this work

The focus of the current research is to develop an efficient industrial scale microwave reactor with a PET material throughput of more than 157 t/a and accordingly a total material throughput from about 1200 t/a to support the microwave assisted alkaline hydrolysis of PET. In the patents [30] and [31] a new method, the corresponding apparatus and scenario for a continuous heating of a high-loss reaction mixture with an electromagnetic field are presented. The design relies on a metallic Archimedean screw placed in a microwave transparent tube, which transports the full mixture through the microwave cavity. The present research is relying on the patents [30], [31] and

on a new microwave applicator design, which meets the needs of an industrial scale process of depolymerization of PET.

Detailed knowledge of the dielectric properties of the material parameters is essential for successful system and process design. Therefore, a system for in-situ monitoring of the chemical reaction under microwave heating conditions must be developed. This system shall allow the reconstruction of the temperature dependent dielectric properties of the reaction mixture consisting of mono-ethylene glycol, sodium hydroxide, water and PET in the ISM band at 2.45 GHz. In addition, this system must allow in-situ temperature and time dependent dielectric measurements under microwave heating conditions. It must be taken into account that the reaction takes place at temperatures above the boiling point and the system must accordingly be able to keep the reaction mixture under pressure. In addition to the dielectric measurements, a calorimetric measurement setup under microwave heating conditions must be developed. These measurements will be used to identify the exothermic or endothermic characteristics of the proposed reaction.

Secondly, based on the measured dielectric properties, a modular and scalable applicator on industrial scale has to be developed. This applicator must allow continuous operation using a metallic Archimedean screw within a glass tube, transparent to microwaves. In this context, the screw geometry has to be optimized with respect to the desired production rate and the overall efficiency of the microwave power. Furthermore, the proposed microwave cavity must ensure a homogeneous field distribution in the axial and azimuthal direction of the reactor.

In addition, a process optimization scenario must be introduced. Thereby the measured temperature and time-dependent dielectric properties have to be used for development of an appropriate reaction kinetics model. In this way, the different reaction scenarios can be evaluated to obtain an optimal reaction process.

Based on the listed objectives, chapter 2 describes the theory of dielectric properties, applied dielectric mixing rules and the alkaline hydrolysis of PET. The developed dielectric and calorimetric measurements setup and the

corresponding calibration procedure are presented in chapter 3. The measured dielectric properties of the individual reactants and of the full reaction mixture are described in chapter 4. Chapter 5 provides an overview of the developed model of the reaction kinetics based on the measured dielectric properties. The design of the developed industrial scale microwave cavity and experimental results with the developed reactor are shown in chapter 6. Finally, a conclusion and outlook are given in chapter 7.

2 Fundamentals

In this chapter, the microwave-assisted depolymerization of PET based on high temperature alkaline hydrolysis are introduced in detail. First, the principles of microwave heating are addressed. Then the different measurements methods for the dielectric characterization of materials and the alkaline hydrolysis of PET are explained.

2.1 Definition of dielectric properties

In general, electromagnetic heating refers to three different heating mechanisms, which are described by the material-specific parameters. The interaction of materials with electromagnetic waves is characterized by their dielectric (permittivity), magnetic (permeability) and conductive (electric conductivity) properties. Usually these material parameters depend on the frequency of the electromagnetic field, the temperature of the material and in case of anisotropic properties, as well on the orientation of the material versus the direction of the electric field [32]. Depending on the dominant material parameters, the electromagnetic heating may be realized through dielectric heating and/or magnetic heating and/or conductive heating.

Dielectric heating relies on the ability of the material to absorb energy when an external alternating electric field is applied. Such a material is called ‘dielectric material’ [32]. A dielectric material is characterized by its complex dielectric constant ϵ . The complex dielectric constant ϵ consists of a real part ϵ' , which represents the energy storage term, and an imaginary part ϵ'' which represents the dielectric loss term.

$$\epsilon = \epsilon' - j\epsilon'' = \epsilon_0 (\epsilon'_r - j\epsilon''_r) \quad (2.1)$$

where $\epsilon_0 \approx 8.8542 \cdot 10^{-12} \text{ C}^2/(\text{N} \cdot \text{m}^2)$ is the vacuum permittivity and ϵ_r' and ϵ_r'' are the relative dielectric constant and relative dielectric loss factor, respectively.

Magnetic heating relies on the ability of a magnetic material to absorb energy when an external alternating magnetic field is applied. A magnetic material is characterized by its permeability μ . The complex permeability μ as well consist of a real part μ' that represents the energy storage term and an imaginary part μ'' that represents the magnetic energy loss term [33].

$$\mu = \mu' - j\mu'' = \mu_0 (\mu_r' - j\mu_r'') \quad (2.2)$$

where $\mu_0 \approx 4\pi \cdot 10^{-7} \text{ H/m}$ is the vacuum permeability and μ_r' and μ_r'' are the relative magnetic constant and relative magnetic loss factor, respectively.

Conductive heating relies on the current flow, which takes place in a conductive material when an external electric field is applied. A conductive material is characterized by its electronic and/or ionic conductivity σ . Since many materials or mixtures of materials comprise dielectric as well as conductive losses, often the effective conductivity σ_{eff} is given as the sum of dielectric and conductive losses by the following formula [32]:

$$\sigma_{eff} = \sigma + \epsilon''\omega \quad (2.3)$$

where ω is the applied field angular frequency.

A dielectric material may experience a variety of polarization mechanisms and loss mechanisms. These parameters strongly depend on the material composition as well as the operating temperature and frequency range [33]. The loss and polarization mechanisms may be classified into ionic conduction, dipolar relaxation, atomic polarization and electronic polarization (see Fig. 2.1). The sum of all mechanisms results in the overall permittivity. In the microwave frequency range, the ionic conductivity and the dipolar relaxation mainly determine the loss behavior of a dielectric material. The effective material losses can be described as the sum of dielectric losses ϵ'' and

conductive losses σ . Depending on the materials composition the conductivity is based on electronic or ionic conductivity.

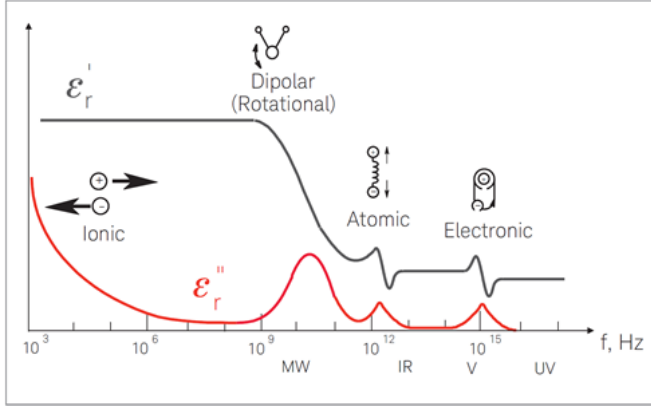


Figure 2.1: Dielectric permittivity over a wide frequency range [32]

The ratio of ϵ_r'' to ϵ_r' is called dielectric loss tangent $\tan \delta$ [32].

$$\tan \delta = \frac{\epsilon_r''}{\epsilon_r'} \quad (2.4)$$

The absorbed power as a function of the applied electric field is determined by the following formula [17].

$$P_{abs} = \int_{V_s} \omega \epsilon' \tan \delta E^2 dV \quad (2.5)$$

V_s is the volume of the dielectric material and E is the amplitude of the electrical field. If the electromagnetic wave propagates in a lossy dielectric material, its amplitude progressively attenuates in the propagation direction.

The distance at which the power of incident wave attenuates by $1/e$, approximately 37 %, is called penetration depth D_p . Assuming that $\mu_r'' = 0$, it can be approximated as follows [34]:

$$D_p = \frac{c_0}{4\pi f} \sqrt{\frac{2}{\epsilon_r'}} \left[\sqrt{1 + \tan^2 \delta} - 1 \right]^{\frac{1}{2}} \quad (2.6)$$

where $c_0 = 1/\sqrt{\epsilon_0 \cdot \mu_0} \approx 3 \cdot 10^8$ m/s is the speed of light in vacuum. The higher the losses of the material the lower is the penetration depth. Accordingly, the dielectric properties of the material (ϵ_r' and ϵ_r'') have significant influence on the field distribution in the material.

2.1.1 Dielectric mixing rules

In general, the effective dielectric properties of a material mixture can be estimated from the dielectric properties of each constituent. For this purpose, several dielectric mixing rules can be applied [35].

The most common dielectric mixing rules are the Maxwell-Garnett (MG) formula and the Lichteneker-Rothers (LR) formula [35], [36]. In the case of the MG rule, the mixture to be analyzed consists of the background material in which spherical inclusions are embedded. The MG formula is given as:

$$\frac{\epsilon_{r,eff} - \epsilon_{r,e}}{\epsilon_{r,eff} + 2\epsilon_{r,e}} = \phi_i \frac{\epsilon_{r,i} - \epsilon_{r,e}}{\epsilon_{r,i} + 2\epsilon_{r,e}} \quad (2.7)$$

where $\epsilon_{r,eff}$, $\epsilon_{r,e}$ and $\epsilon_{r,i}$ are the effective permittivity of the mixture, background material and inclusion, respectively. ϕ_i is the fractional volume of the inclusion. However, it must be mentioned, that the equations are based on the assumption that all inclusions are spherical [35]. The LR formula can be applied in a wider range than the MG formula to both isotropic and anisotropic mixtures and it is expressed as:

$$\epsilon'_{r,eff} = (\phi_i \epsilon_{r,i}^{\zeta} + (1 - \phi_i) \epsilon_{r,e}^{\zeta})^{1/\zeta} \quad (2.8)$$

where ζ is the LR exponential factor and is specified by the composites micro-geometry [36].

2.2 Dielectric measurement methods at microwave frequencies

During recent years, a variety of methods for measuring the dielectric parameters of materials have been developed [37], [38]. Usually, the choice of the most appropriate measurements technique depends on factors such as the range of the expected dielectric properties, the operating frequency, the required measurement accuracy, the sample geometry, and finally, the aggregate state of the material under test. The methods can be grouped in the reflection method, the transmission-reflection method and the resonance method as shown in Table 2.1 [33].

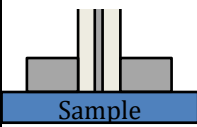
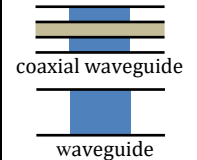
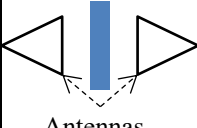
2.2.1 Reflection method


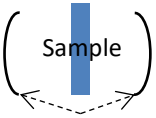
This method is based on the measurement of the reflection of an electromagnetic wave entering a dielectric material. A very common implementation of this method is the so-called coaxial probe measurement. The key component of this measurement method is an open-ended coaxial waveguide (Fig. 2.2) [32]. The material is measured either by inserting the probe into a liquid sample or by touching the flat surface of a liquid or by half-solid material. A perfect contact between the sample and the probe without any air gap is necessary and it is necessary, that the area and the thickness of the sample are sufficiently large, so that the complete fringe field of the probe is contained. This method enables the measurement of liquid and semi-liquid materials over a very broad frequency range with a single probe. It is applicable for medium- and high-loss dielectric materials ($\tan \delta > 0.05$).

2.2.2 Transmission-Reflection method

Another method is based on the measurement of the complex transmission coefficient (S_{21}) and the complex reflection coefficient (S_{11}) from which the complex material permittivity can be calculated. A sample partially fills a transmission line, which is usually a section of a rectangular or coaxial waveguide [39].

Table 2.1: High frequency dielectric measurement methods and their pros and cons

	Method	S-Parameter Measured par.	Advantages	Disadvantages
Reflection	Coaxial Probe 	S_{11} ϵ_r	Broadband, Flexible sample geometry	Sample surface quality, temperature restrictions through the coaxial probe
Transmission – Reflection	Waveguide 	S_{11}, S_{21} ϵ_r, μ_r	Broadband	Complex sample geometry preparation
	Free space 	S_{11}, S_{21} ϵ_r, μ_r	Suitable for high temperatures, easy sample preparation	$\lambda \ll \text{MUT}$, multiple reflections between the antennas

Resonance	Cavity		High precision, microwave heating in the cavity possible	Single frequency, high demands on sample geometry, small permittivity
		S_{11}, S_{21} ϵ_r, μ_r		
	 Open resonator	S_{11}, S_{21} ϵ_r, μ_r	High precision	Narrowband, complex sample preparation, $\lambda \ll \text{MUT}$

mitted signal, the complex permittivity of the sample can be estimated [32]. This method enables the dielectric characterization of medium and high loss dielectric materials over the full frequency band of the waveguide. Furthermore, it allows the measurement of magnetic material properties with the same measurement setup. Similarly, the measurement takes place in the free-space method. Here antennas are used to focus microwave energy onto or through a sheet of material. This method is contactless and can be used on materials that are exposed to high temperatures [32].

2.2.3 Resonance method

The resonance method is the most precise analysis for determining the complex permittivity and permeability of materials. However, there are strong limitations to the measurement technique given by the accuracy of the sample geometry and the maximum sample dielectric and magnetic losses. Different types of resonators such as cavity resonators [40], split-cylinder resonators [41] and Fabry-Perot resonators [42] can be used. This method allows the dielectric characterization of samples at the individual frequencies of the existing modes in the resonator. The most common resonance method is the cavity perturbation method, which is explained in more details as follows.

2.2.4 Microwave cavity

A microwave cavity can be described as a hollow structure enclosed by metallic walls. In simple terms, it can be expressed as a waveguide that is short-circuited at both ends. The cavity may be either hollow or filled with a dielectric material. Standing waves are formed within the cavity at specific resonance frequencies. Each resonance frequency corresponds to a certain field distribution. This field distribution is called resonance mode. Depending on whether the electric field or the magnetic field is perpendicular to the third dimension of the cavity, a distinction is made between TE_{nml} modes and TM_{nml} modes [43]. In the case of a coaxial cavity, a TEM_{nml} mode can also be formed in which both the electric and the magnetic field are perpendicular to the third dimension of the cavity. The indices n , m and l correspond to the number of field variations along the three dimensions of the cavity [43]. Sometimes not all boundary conditions can be fulfilled by pure TE- or TM-modes. In such cases, linear combinations of TE- and TM- modes can provide a complete and general solution, the so-called hybrid modes [43].

The most common microwave cavities are based on a rectangular or cylindrical waveguide short-circuited at both ends. The resonance frequency of a rectangular cavity is determined using the following equation [43]:

$$f_{nml} = \frac{c_0}{2\pi\sqrt{\mu_r\epsilon_r}} \sqrt{\left(\frac{n\pi}{a}\right)^2 + \left(\frac{m\pi}{b}\right)^2 + \left(\frac{l\pi}{d}\right)^2} \quad (2.9)$$

where c_0 is the speed of light in vacuum. a , b and d correspond to the three dimensions of the rectangular cavity.

Similarly, the resonance frequency of a cylindrical cavity is determined using the following equations [43]:

$$f_{nml} = \begin{cases} \frac{c_0}{2\pi\sqrt{\mu_r\epsilon_r}} \sqrt{\left(\frac{p'_{nm}}{a}\right)^2 + \left(\frac{l\pi}{d}\right)^2} & \text{for TE}_{nml} \text{ modes} \\ \frac{c_0}{2\pi\sqrt{\mu_r\epsilon_r}} \sqrt{\left(\frac{p_{nm}}{a}\right)^2 + \left(\frac{l\pi}{d}\right)^2} & \text{for TM}_{nml} \text{ modes} \end{cases} \quad (2.10)$$

Where p_{nm} is the root of the first kind Bessel function J_{nm} and p'_{nm} is the root of the derivative of the first kind Bessel function J_{nm} . a and d corresponds to the radius and length of the cylindrical cavity.

Fig. 2.2 shows the mode chart of cylindrical cavities [43]. As can be seen for specific ratios between radius and length of the cavity more than one mode can be excited simultaneously at exactly the same frequency. For example, at the red circle marks an area where the diameter is equal to the cavity length, the TM_{010} -mode and the TE_{111} -mode can be excited simultaneously.

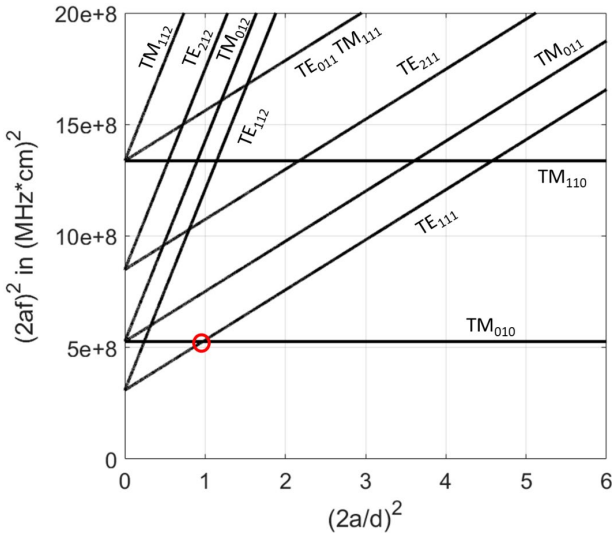


Figure 2.2: Mode chart of a cylindrical cavity [43]

The quality factor of a cavity with a resonance frequency ω_0 is defined as the ratio of the average energy stored in the cavity to the energy loss during one oscillation period [43]:

$$Q_0 = \omega_0 \frac{W_m + W_e}{P_{loss}} \quad (2.11)$$

where W_m and W_e corresponds to the magnetic and electric energy stored and P_{loss} corresponds to the resonator losses. The resonator losses are the sum of the conducting wall losses, dielectric losses, radiation losses and coupling losses. Within a cavity with a very large quality factor, a small power signal results in a very large electric and magnetic field strength near the resonant frequency [44]. Such cavities are used as microwave ovens, filters etc. The power losses at the conducting walls of a cavity are defined as follows:

$$P_c = \frac{R_s}{2} \int_s |H_t^2| ds \quad (2.12)$$

where $R_s = \sqrt{\omega\mu_0/2\sigma}$ is the surface resistivity of the metal walls and H_t is the tangential magnetic field on the resonator walls.

The Q-factor of a rectangular cavity with lossy walls, filled with a lossless dielectric material and without consideration of radiation losses and coupling is determined as follows [43]:

$$\begin{aligned} Q_c &= \frac{2\omega_0 W_e}{P_c} \\ &= \frac{k^3 abd\eta}{4\pi^2 R_s} \frac{1}{\left[\left(\frac{2l^2 ab}{d^2} \right) + \left(\frac{bd}{a^2} \right) + \left(\frac{l^2 a}{2d} \right) + \left(\frac{d}{2a} \right) \right]} \\ &= \frac{(kad)^3 b\eta}{2\pi^2 R_s} \frac{1}{2l^2 a^3 b + 2bd^3 + l^2 a^3 d + ad^3} \end{aligned} \quad (2.13)$$

a, b and d correspond to the physical dimensions of the rectangular cavity resonator, η is the wave impedance in the medium, l is the number of half waves in the third dimension of the rectangular cavity and k is the wave

number. The Q - factor of a cylindrical cavity with lossy walls, filled with a lossless dielectric material and without consideration of radiation losses and coupling walls for a TE_{nm1} -mode is determined as follows [43]:

$$Q_c = \frac{\omega_0 W_e}{P_c} \frac{1 - \left(\frac{n}{p'_{nm}}\right)^2}{4(p'_{nm})^2 R_s \frac{ad}{2} \left[1 + \left(\frac{\beta a n}{(p'_{nm})^2}\right)^2 \right] + \left(\frac{\beta a^2}{p'_{nm}}\right)^2 \left(1 - \frac{n^2}{(p'_{nm})^2}\right)} \quad (2.14)$$

a and d are the cavity radius and length, respectively. p'_{nm} is the zero position of the Bessel function of first kind, k is the propagation constant and β is the phase constant.

Similar, the Q-factor of the TM_{nm1} -modes is given by [45]:

$$Q_c = \frac{\eta \left[p_{nm}^2 + \left(\frac{l\pi a}{d}\right)^2 \right]^{1/2}}{2R_s \left(1 + \frac{2a}{d}\right)} \quad (2.15)$$

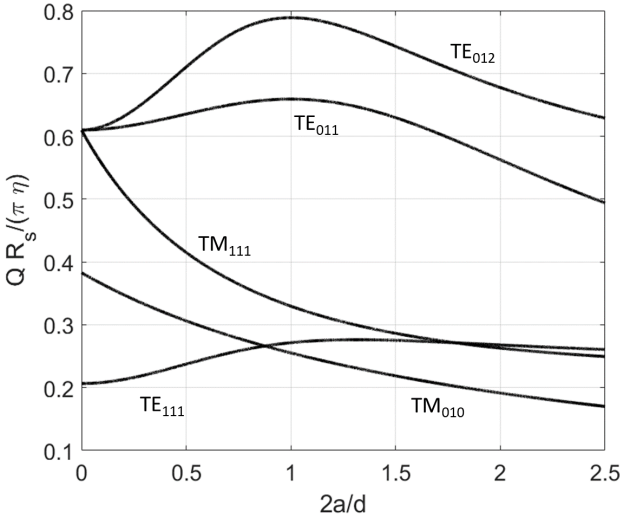


Figure 2.3: Normalized unloaded quality factor of a cylindrical resonator for various modes [43]

Fig. 2.3 shows the quality factor of an empty cylindrical cavity depending on the mode and the cavity geometry without consideration of coupling and radiation losses. As can be seen for specific ratios between radius and length of the cavity, the Q_c of existing modes in the resonator can be influenced.

Cavity perturbation method

The perturbation of the field in the microwave cavity can be realized by the modification of the cavity volume or the introduction of a small sample of a dielectric material. The latter is applied for the dielectric characterization of materials. The material perturbation method is based on the comparative analysis of electromagnetic properties and is based on the assumption that the electromagnetic field in the cavity with and without sample remains more or less constant. The determination of the sample parameters is realized by the measurement of the frequency shift and the quality factor change, which is generated through the perturbation of the electromagnetic field.

The change of the complex angular frequency Ω_m of an empty cavity by introduction of a material sample is given by the following equation [33].

$$\frac{\Omega_{m_1} - \Omega_{m_0}}{\Omega_{m_0}} = \frac{-\int_{V_s} (\epsilon_r - 1) E_0^* E_1 dV}{\int_{V_c} (E_0^* E_1 + H_0^* H_1) dV} \quad (2.16)$$

Ω_{m_0} and Ω_{m_1} are the complex resonance frequencies for the empty and perturbed cavity, respectively. ϵ_r is the complex relative permittivity H_0 , H_1 and E_0 , E_1 are the complex magnetic fields and complex electric fields, respectively before and after the introduction of the sample. The denominator represents the integral over all the cavity volume V_c , while the numerator is the integral over the sample volume V_s .

At the resonance frequency the stored magnetic energy W_m in the cavity is equal to the stored electric energy W_e . Under this assumption, the Eq. 2.16 can be simplified as follows.

$$\frac{\Omega_{m_1} - \Omega_{m_0}}{\Omega_{m_0}} = \frac{-\int_{V_s} (\epsilon_r - 1) E_0^* E_1 dV}{2 \int_{V_c} (E_0^* E_1) dV} \quad (2.17)$$

The complex resonance frequency Ω_m of a resonator is connected to the resonance frequency f and the Q-factor of the resonator as follows [33]:

$$\Omega_m = \Omega_{m_r} + j\Omega_{m_i} \quad (2.18)$$

$$\Omega_{m_r} = 2\pi f \quad (2.19)$$

$$Q = \frac{\Omega_{m_r}}{2\Omega_{m_i}} \quad (2.20)$$

If the perturbation of the field is small, $\Omega_{m_0} \approx \Omega_{m_1}$ and $\Omega_{m_i} \gg \Omega_{m_r}$, then according to the cavity perturbation theory, the Eq. 2.17 can be separated in the real and imaginary parts. The dielectric properties of the material under test (MUT) are calculated as follows [33].

$$\epsilon_r' = \frac{1}{A} \frac{(f_0 - f_1) V_c}{f_0 V_s} + 1 \quad (2.21)$$

$$\tan \delta = \frac{1}{\epsilon_r' B} \left(\frac{1}{Q_1} - \frac{1}{Q_0} \right) \frac{V_c}{V_s} \quad (2.22)$$

Q_0 and Q_1 represent the corresponding quality factors. V_c and V_s are the volumes of the cavity and the material sample, respectively. A and B are specific factors based on the geometry of the cavity and the cavity mode excited. For a small material perturbation ($E_0 = E_1$) A and B are constant.

Temperature dependent dielectric measurements

The reconstruction of the dielectric properties of several materials has been investigated with various methods in several publications [46], [47], [48], [49] and [50]. In parallel a variety of methods for measuring the dielectric parameters of materials over predefined heating scenarios have been developed during recent years [37], [38]. As it is well known, the resonant method, such as the cavity perturbation method is well suited for dielectric material with low and moderate dielectric properties [33], while the reflection method, such as the coaxial probe, and the transmission/ reflection method are suitable for the measurement of dielectric materials with medium and high losses [51]. In particular, the resonance method is well suited for microwave heating of lossy as well as low loss dielectric materials due to the high electric field amplitude in the cavity at resonance frequency. Of course, a sufficient source of microwave power must be available for that purpose.

Measurements on dielectric materials in a broad temperature range based on the cavity perturbation method are presented in [38]. This experimental setup is based on a rectangular TE_{104} cavity. Here the sample is heated stepwise in a conventional oven up to 1200 °C and afterwards is moved into the cavity for measurements. The dielectric properties were reconstructed using 3D full wave simulations by solving the inverse problem. This means that the material parameters of MUT are varied in expected permittivity range and the Q-factor and resonance frequency change is simulated.

Couderc et al. [52] developed a dual-mode cylindrical cavity based on a TM_{010} -mode and a TE_{111} -mode. Here the TM_{010} -mode is used as a heating mode at 2.45 GHz and the TE_{111} -mode is applied for dielectric measurements at about 3 GHz. Both modes are individually coupled into the cavity with minimum cross-coupling. Another study based on a dual-mode coaxial cavity for high-temperature measurements of small samples is presented in [53]. In both cases, microwave tuners are required during heating to adjust the resonance frequency of the loaded cavity to the fixed frequency of the magnetron power source in order to allow sample heating.

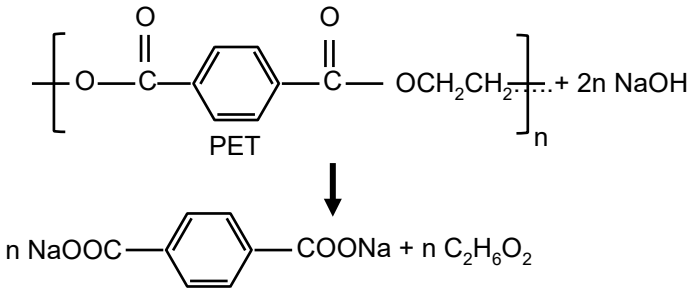
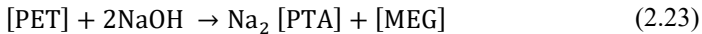
Nikawa et al. already developed a simplified in-situ technique for simultaneously heating and measuring of dielectric parameters using a 2.45 GHz TM_{010} -mode cavity [54]. For this purpose, the output power from the vector network analyzer (NWA) is amplified up to 100 Watt. Another in-situ test set is presented in [37]. This work demonstrates that it is possible to create a system, which enables simultaneous heating and measuring using the same microwave source. This system is based on a cylindrical TE_{111} -mode cavity and on a tunable high-power microwave amplifier. Nevertheless, a challenge of this measurement approach is the need of strong coupling for sufficient heating of the material in the cavity. But a strong coupling has a significant influence on the measurement accuracy and so far, inhibited accurate measurements of the dielectric loss factor, because the coupling is assumed as negligible in the equations for the perturbation theory. To increase the efficiency and control quality, Catala et al. extended the above-described approach in his work [55]. A dual-mode cylindrical cavity operating at both TE_{111} - and TM_{010} -modes was developed. In the design, the TM_{010} -mode was used for heating of the sample while dielectric measurements were performed using the TE_{111} -mode. However, this measurement setup is restricted to dielectric materials with low and medium losses since the reconstruction of the dielectric properties is based on an analytical model.

As already stated, the classical cavity perturbation method is valid for measurements of low-loss dielectrics where the perturbation of the resonance is sufficiently small. High-loss materials, when being placed in the cavity, result in a deterioration of the transmission resonance peak in such a way that

the classical cavity perturbation method is no longer valid. The deterioration of the resonance peak, however, also depends on the particular field mode excited. A dual-mode cavity approach going along with a calibration procedure based on full-wave simulation may help to extend the measurement range towards high loss materials and increase the accuracy of the measurements.

2.3 Alkaline hydrolysis of PET

In the depolymerization reaction, the PET is hydrolyzed in sodium hydroxide (NaOH) that yields to the disodium salt, Na₂[PTA] and mono-ethylene glycol (MEG) [56]:



The reaction mixture consists of a sodium hydroxide solution and PET particles. The reaction takes place at the surface of the PET flakes and therefore the reaction is directly influenced by the particle size.

According to various studies, the alkaline hydrolysis of polyethylene terephthalate is described as both slightly endothermic [57] and slightly exothermic reaction [58]. According to [57], during the hydrolysis of PET an additional thermal energy input (endotherm) of about 5 kJ/mol is required. In

contrast, according to [58], an energy of about 70 kJ/mol is released (exotherm) during the hydrolysis of PET. This makes the further investigation of the reaction enthalpy particularly interesting.

Calorimetric measurements

In general, calorimetry is a tool to measure the heat transfer in a material associated with changes in the material due to a chemical reaction, physical change, or phase transition. In particular, by chemical reaction, calorimetry enables the investigation of the power required to follow the reaction (endothermic reaction) or the released power during the reaction (exothermic reaction). The most common methods of calorimetry are differential scanning calorimetry [59], isothermal titration calorimetry [60] and isothermal micro calorimetry [61]. For all of these conventional calorimeters a thermally isolated system is required in order to get an accurate information.

In addition to the above mentioned calorimetry methods, there exists also various investigations about thermal analysis setups under microwave heating conditions. In this case, quantitative results are difficult to obtain because the thermal analysis always assumes that the sample is in thermal equilibrium with its environment. But this is never the case with microwave heating. Parkes et al. [62] have developed a thermal analysis system based on a single-mode rectangular cavity and a narrow band high frequency power source (see Fig. 2.5). Since the applied power source is not frequency-tunable, the proposed system enables the microwave heating of the sample based on complex tuning elements (e.g. variable coupling iris, short plate tuner and a stab tuner). In this work a qualitative thermal analysis has been carried out through the sample temperature monitoring and the proposed applied power. Nesbitt et al [37] has developed a more accurate microwave calorimeter based on TE_{111} -mode cylindrical cavity and a tunable solid-state amplifier. This system enables accurate power measurements with the help of a power meter. Here the incident and the reflected microwave power had been continuously monitored.

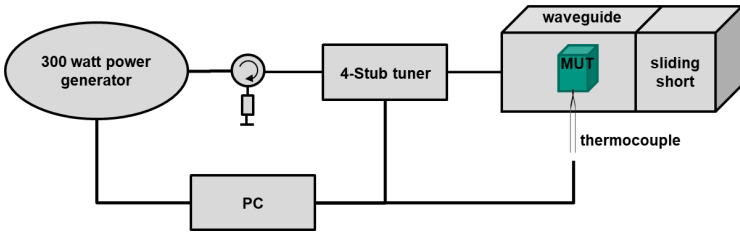


Figure 2.4: Calorimetric measurements under microwave heating conditions, proposed by Parker et al. [62]

3 Dielectric and calorimetric measurement systems

Microwave chemistry shows increasing applications in the last years. It enables a faster and more energy efficient reaction [63]. For the successful design of microwave applicators, the a-priori knowledge of the temperature dependent dielectric properties of the involved materials is required. Furthermore, the detailed knowledge of the reaction kinetic and power requirements is important. In this chapter, a novel dielectric and calorimetric measurement system is presented.

3.1 In-situ, high pressure and high precision measurement setup

3.1.1 Design methodology

The equations 2.15 and 2.16 are derived without taking into account the coupling ports, sample holder and perturbation of the electromagnetic field in the cavity when introducing the material under test. However, for strong material perturbation ($E_0 \neq E_1$) the changes of the electric field and coupling losses have to be taken into account. Those effects may be accounted in the factors A and B in equations 2.15 and 2.16, which become dependent in that case on the dielectric properties of the sample. Moreover, for strong perturbations the separation of the complex frequency into real and imaginary parts is no longer valid. A calibration procedure is necessary based on full wave numerical simulations [38]. The frequency shift Δf of the resonance and/or the change in quality factor saturate with increasing dielectric constant and/or loss factor. However, this is dependent on the wave mode excited in the cavity. In Fig. 3.1 the electric fields for the first two modes (TE_{111} and TM_{010}) in a cylindrical cavity can be seen. Both modes are often used for the dielectric characterization of materials, because they have an electric field maximum in

the center of the cavity. Fig. 3.1 also shows the electric field distribution in a lossless MUT with very high dielectric constant ($\epsilon'_r = 20$) located on the axis of the cylindrical cavity. In Fig. 3.2 the dependencies of the frequency shift Δf and Q- factor versus ϵ' and $\tan \delta$ are plotted for TM_{010} and TE_{111} mode in the cylindrical resonator. It is obvious that for the TM_{010} -mode the frequency shift with increasing permittivity shows a nearly linear behavior for $1 < \epsilon'_r < 50$ without saturation, while for the TE_{111} -mode it saturates already at $\epsilon'_r > 10$. Vice versa the quality factor for the TM_{010} -mode gets saturated significant earlier with increasing $\tan \delta$ ($\tan \delta > 0.2$) as compared to the TE_{111} -mode.

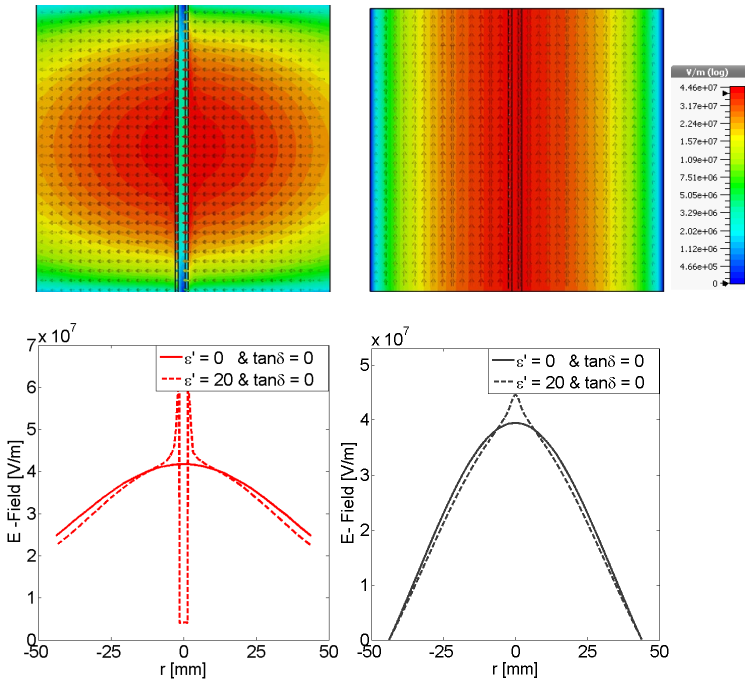


Figure 3.1: Sideview of cavity E-Field for $\epsilon'_r = 20$ and $\tan \delta = 0$: TE_{111} (top left) and TM_{010} (top right), E-Field stretch in the center of the cavity: TE_{111} (bottom left) and TM_{010} (bottom right) [64]

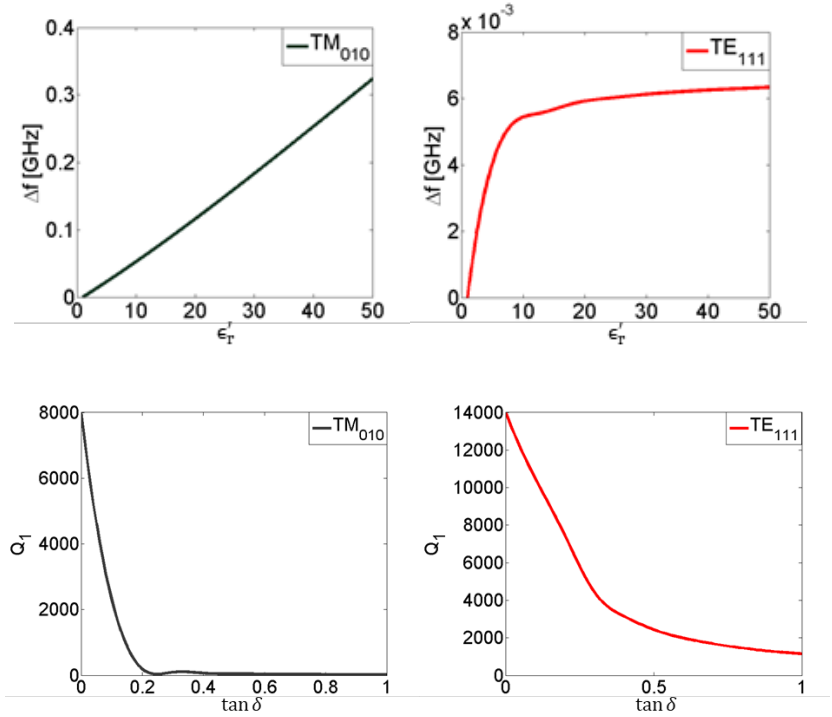


Figure 3.2: Simulated $\Delta f(\epsilon_r')$ for $\tan \delta = 0.01$ (top) and $Q(\tan \delta)$ for $\epsilon_r' = 40$ (bottom) for a cylindrical sample with 3 mm in diameter in a cavity with 88.5 mm in diameter and a length of 90 mm [64]

The dual-mode resonator approach solves this problem. The loss factor is measured with the TE_{111} -mode and the dielectric constant in the TM_{010} -mode. The modes are well separated from each other because of their orthogonality (see Fig. 3.1). That allows a separate measurement at both modes without interference. Additionally, for samples with a high permittivity the TM_{010} -mode resonance shows a much larger frequency shift as compared to the TE_{111} mode resonance. However, because of very low quality factors for $\tan \delta > 0.2$ the TM_{010} -mode resonance becomes unmeasurable. This is why the focus is on measurement of dielectric losses in the TE_{111} -mode resonance.

Those effects can be explained with the help of Eq. 2.17 and considering an ideal sample without dielectric losses. Fig. 3.1 reveals that for the TE_{111} -mode the electric field within the sample is decreasing significantly for large ϵ_r' values. This phenomenon can be explained by the oblique incident electric field on the cylindrical MUT surface, which leads to a scattering of the field. Therefore, the numerator in the Eq. 2.17 decreases. At the same time, the stored energy in the cavity, becomes higher due to the higher effective ϵ_r' in the cavity. Therefore, the denominator becomes higher. This results in a continuous decreasing frequency shift and therefore a saturation of the frequency.

For the TM_{010} -mode (Fig. 3.1) numerical simulations show that the E-field is slightly peaking around the sample position. This can be explained by the electric fields oriented along the MUT. Accordingly, the numerator in Eq. 2.17 is slightly increasing with ϵ_r' . At the same time, the total stored energy has to increase with ϵ_r' . Then the total stored energy in the cavity outside from the sample becomes slightly lower (because of field peaking), that results in constant or weak increasing frequency shift function with ϵ_r' .

To account the above-mentioned deviations in the dual mode cavity system from the classical perturbation theory the calibration of the measurement system is realized with the help of interpolated full wave 3D simulation. Further information will be given in chapter 3.2.2. These results were published in [64].

3.1.2 Cavity design

The designed empty cavity operates at the TE_{111} -mode and at the TM_{010} -mode at around 2.6 GHz [64]. This frequency is chosen in consideration of the expected frequency shift (see Fig 3.2) and the operating frequency range of the power amplifier. The model of the cavity used for CST simulations is shown in Fig. 3.3. The cavity diameter is 88.49 mm and the cavity height is 88.50 mm. This dimension corresponds to the intersection between the both modes, which exist for a diameter equal to the radius (see Fig 2.2). The considered dimensions enables the excitation of only the two modes in the resonator in the frequency range under consideration. The cavity material is

aluminum 6020, which has a specific electrical resistivity of about $3.7 \cdot 10^{-6}$ ohm-cm [65]. With the help of Fig. 2.3, the theoretical Q-factor (without coupling and under consideration of the cavity material) can be determined to be approx. 17500 and 18900 for the TM_{010} -mode and the TE_{111} -mode, respectively. The unloaded Q-factor included coupling for the TE_{111} -mode is calculated to be about 8000 and about 6000 for the TM_{010} -mode, respectively [64].

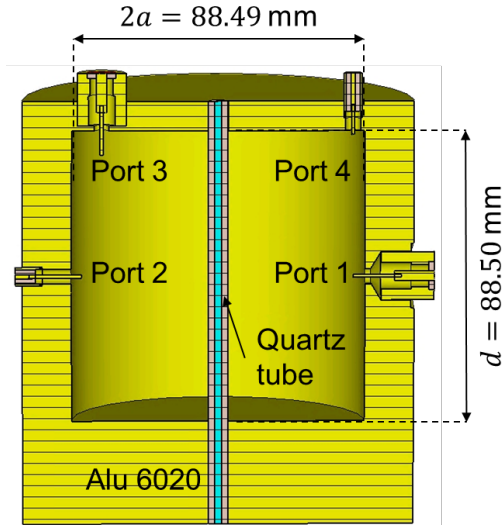


Figure 3.3: Dual-mode cavity simulated with CST Microwave Studio [64]

The TE_{111} -mode is coupled through a coupling element at port 1, which is a modified N-type coaxial adaptor with a 5.30 mm long copper pin acting as an inductive coupling (see Fig. 3.3). The microwave power of the TE_{111} -mode is decoupled from the cavity at port 2 where a modified SMA coaxial adaptor with a 3.05 mm copper pin is used. Through the port 3 the microwave is coupled to the TM_{010} -mode. The port 3 is a modified N-type coaxial adaptor with a copper pin of 11.70 mm in length. The decoupling of the TM_{010} -mode is realized through port 4, using a modified SMA coaxial adaptor with a

3.55 mm long copper pin. The pin length of the coupling ports is selected to allow a sufficient strong power coupling for subsequent microwave- assisted heating of the MUT, and the decoupling ports are selected to allow a measurable transmission (> -60 dB) in the loaded cavity. This coupling design enables an isolation of about 60 dB between both modes (see Fig. 3.4). In Fig. 3.4, the cross-talk between port 1 and port 3 (from Fig. 3.3) is shown, as these are the two with the strongest coupling factor. At both resonance positions two characteristic ‘fano-like’ resonances are visible [66]. Such resonance results from the interference between a broadband, e.g. through the direct transmission between the two coupling ports, and a narrow band resonance, e.g. TM_{010} -mode or TE_{111} -mode of the resonator. As sample holder a fused quartz-tube, with an inner diameter of 2 mm and an outer diameter of 6 mm, is used (see Fig. 3.3). The diameter is chosen according to the expected maximum frequency shift for a sample permittivity of up to $\epsilon'_r = 80$ with regards to the frequency bandwidth of the amplifier (2.0 – 2.7 GHz). The liquid sample fills the fused quartz tube.

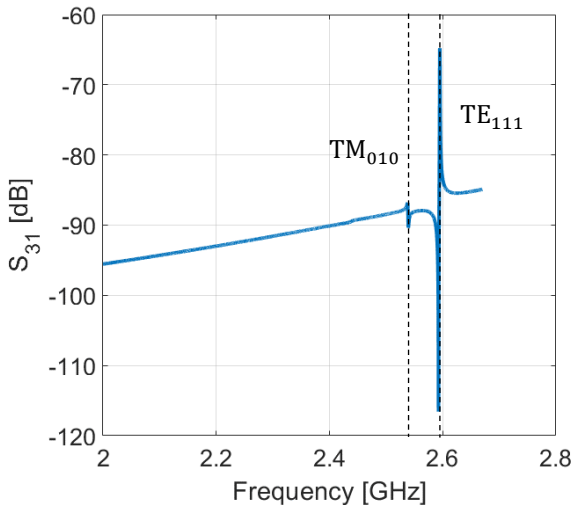


Figure 3.4: Simulated transmission between port 1 and port 3 of the dual-mode cavity

As already mentioned, here the TM_{010} -mode is also used to heat the sample by microwaves. This mode is particularly suitable for heating, as it has a homogeneous field along the sample. The resulting inhomogeneity in temperature along the sample was investigated both in experiment with the help of two fiber-optic sensors of the type Optocon TS2 and in simulation as well. The result of the simulation with COMSOL multiphysics showed that the expected temperature inhomogeneity along the sample inside the cavity due to convection and heat conduction losses is ± 1 °C at around 180 °C (see Fig. 3.5). This behavior is also verified experimentally. The gradient at both MUT ends is due to the transition from the cold MUT part outside the microwave field to the heated MUT part inside the microwave field.

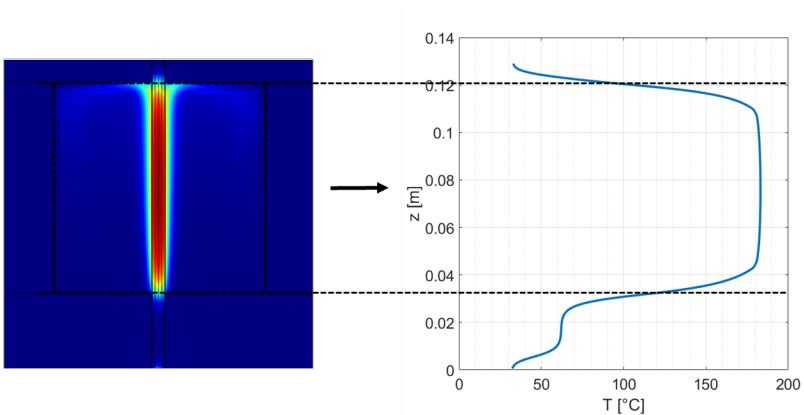


Figure 3.5: Temperature distribution along the MUT by heating with the TM_{010} mode and taking into account the convection and conduction heat losses calculated with COMSOL multiphysics simulations

3.1.3 Measurement setup

The block diagram of the measurement system is shown in Fig. 3.6 [64]. A key element of the measurement system is the frequency-tunable power amplifier. The WMP2350/700/50MK-A from G-Way Microwave, which provides up to 50 dBm (100 W) output power. It has a gain of up to 50 dB. A vector network

analyzer (VNA) Agilent N5224A is utilized both for the measurement of the transmission coefficient of the TM_{010} -mode and for providing the input power for the amplifier. To reduce the nonlinear effects of elements between VNA output and input of the cavity, the so-called “high power” configuration of the VNA is used including the external reference signal. A second VNA HP8720d is used for measurement of the transmission coefficient of the TE_{111} -mode. The sample temperature is measured in the center of the sample with the help of a fiber-optic temperature sensor of type Optocon TS-NANO. The temperature sensor signal is used for the temperature control along the predefined temperature scenario with the help of a proportional-integral-derivative (PID) control algorithm. The fiber-optic sensor was calibrated before each measurement by a one-point calibration at 180 °C with the help of a calibration oven from Eurolec of type MK173 and a calibrated thermometer, from Mawi-Therm of type P755.

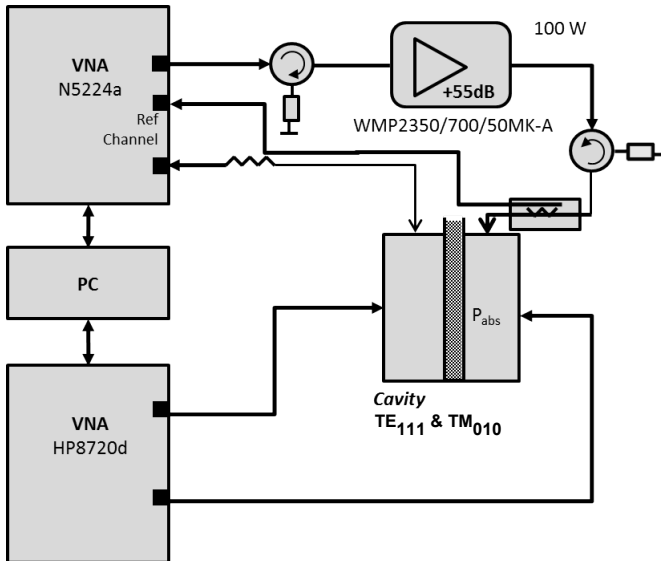


Figure 3.6: Block diagram of the dielectric measurements system [64]

Fig. 3.7 shows the measurement cell of the developed measurement setup. Since the reaction mixture consists of sodium hydroxide solution and PET particles, the sample should be oriented horizontally (to avoid sedimentation of the solid parts of the sample). The sample holder was fixed and closed at both ends with Swagelok connectors, which can withstand a pressure up to 18 bars. For active control of the cavity temperature two QuickCool Peltier elements of type QC-241-1.0-3.9M were installed. This enables the temperature stabilization of the cavity to avoid any dilatation, that may influence the reference resonance frequency of the unperturbed cavity.

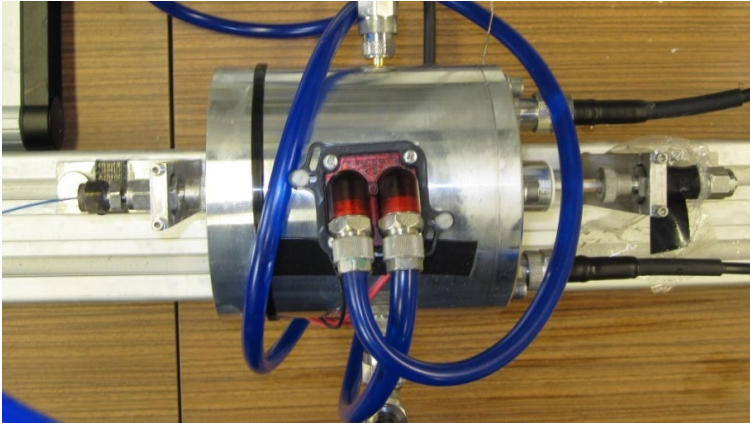


Figure 3.7: Test setup for the dielectric measurements

3.1.4 Calibration method

Following the classical cavity perturbation method, for finding of the dielectric constant and loss factor from the experimentally measured frequency shift ($f_0 - f_1$) and $(1/Q_1 - 1/Q_0)$ the Eq. 2.21 and Eq. 2.22 have to be solved. However, for high permittivity values this method is no longer valid while the calibration factors A and B are not constant but material-dependent. To resolve this problem a novel calibration procedure is used [64]. For that purpose, the cavity geometry (see Fig. 3.3) is accurately simulated with the help of 3D full

wave simulator CST Microwave Studio (Fig. 3.8). The frequency domain solver is used for the range of the expected dielectric properties. The frequency domain solver is especially suitable for geometries with a very high Q-factor.

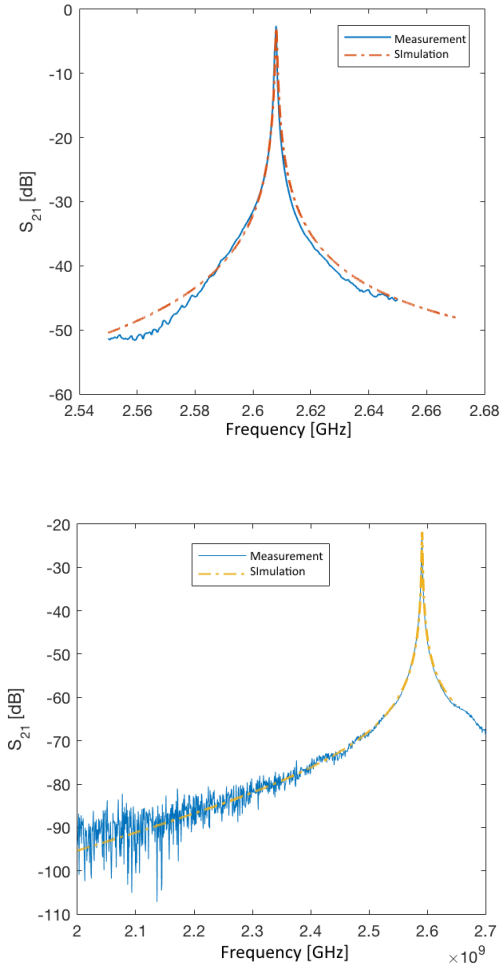


Figure 3.8: Simulated and measured S_{21} - parameters for the TE₁₁₁-mode (top) and for the TM₀₁₀-mode (bottom) [64]

Fig. 3.8 shows the measured and simulated transmission for the two modes in the empty cavity. In order to exclude errors due to manufacturing tolerances, the exact diameter of the cavity is determined based on the TM_{010} -mode resonance frequency and then the exact length of the manufactured cavity is determined based on the TE_{111} -mode resonance frequency.

Then, based on the precisely determined dimensions of the manufactured cavity, the perturbed resonator is simulated for different combinations of dielectric properties of the MUT. Thus, the Q-factor and f_r for the different MUT parameters can be determined for both modes. To estimate ϵ' , the calculated data of the frequency shift for the TM_{010} -mode are interpolated. Here a linear interpolation is used, because the frequency shift shows an almost linear behavior versus ϵ' . To estimate the loss factor of the TE_{111} -mode, the change in the Q-factor data is interpolated with a cubic spline. For the estimation of $\tan \delta$ the a-priori knowledge of ϵ' is required, since the quality factor of the TE_{111} -mode depends on ϵ' strongly.

3.1.5 Error estimation

To validate the designed dual-mode experimental setup, two known high lossy liquids, alcohol and distilled water, are measured at room temperature. The same materials are also measured with the commercial coaxial probe HP85070B (Fig. 3.18). The properties measured with both dielectric measurements systems and the corresponding literature values are compared in Table 3.1

Table 3.1: Measured dielectric properties with the dual-mode approach, coaxial probe HP85070B and the corresponding literature values shown in [43] and [67]

Material	Dual mode cavity		Coaxial probe		Literature [67]; [43]	
	ϵ'_r	ϵ''_r	ϵ'_r	ϵ''_r	ϵ'_r	ϵ''_r
Alcohol	10.55	9.75	10.67	9.90	11.23	11.02
Dist. water	78.67	9.28	77.30	9.32	76.7	12.04

For both highly lossy liquids, the dual mode cavity approach shows a good agreement with the results from the coaxial probe. The literature values are for water at 3 GHz [43] and for spirit at 5.65 GHz [67] that may explain the deviation from the measured data.

The most important sources of error are the inaccuracy of the sample volume, the error in the numerical calibration of the coefficients A and B , the variation of the resonator volume and the frequency resolution of the VNA. In the following section, the errors are determined individually and the impact on the measurement accuracy is estimated.

Sample volume

The accuracy of the cavity perturbation method is strongly affected by the accuracy of the sample geometry. Since the sample length is equal to the resonator length, only the sample diameter can affect the measurement accuracy. To minimize this source of error all applied sample holders had been cut from the same quartz tube. The inner diameter of the used quartz tube is 2.05 mm and the maximum measured deviation is ± 0.01 mm. This results in a measurement error of $\leq 1\%$ for the dielectric constant and $\leq 2\%$ for the loss factor.

Numerical calibration

Another uncertainty originates from the numerical calibration of the coefficients A and B (Eq. 2.21 and 2.22). The error is caused by the error in tolerances of the simulation and the error in the linear interpolation of the simulation results. The error due to the interpolation is estimated directly by MatLab and the error due to numerical simulations was determined by varying the discretization parameters and the pre-set simulation accuracy. The maximum error for the coefficients A and B within the calibration ranges $5 < \epsilon'_r < 35$ and $0.1 < \tan \delta < 1.2$, amount to 1 % and 2 %, respectively.

Resonator volume

Another uncertainty may result from the thermal expansion of the cavity. This effect, however, is negligible as the cavity temperature is stabilized to

15 ± 0.3 °C cavity. The cavity was stabilized at 15 °C instead of room temperature to ensure a more accurate temperature stabilization, since the Peltier elements used can provide an active cooling only.

VNA resolution

The limited frequency resolution of the VNA may cause an error. For the present measurement system, a relatively low frequency resolution of the VNA is used to enable a fast system control. The frequency resolution of the ‘Agilent N5224a’, which is used for the measurement of the TM_{010} -mode, is set to 601 frequency points. During measurements, the frequency span is typically 50 MHz. This results in a maximum error in the measured resonance frequency of $50 \text{ MHz} / 601 \approx 83 \text{ kHz}$. It results in an error of ± 0.01 for the dielectric constant. In addition, the frequency resolution of the ‘HP8720d’, which is utilized for the measurement of the TE_{111} -mode, is set to 601 measurements for a frequency bandwidth of 3 MHz. Since the unloaded cavity has a quality factor of approx. 8000, it corresponds to a maximum deviation in the Q-factor of approx. ± 60 . This corresponds to a maximum error of $\pm 4\%$ for the loss factor in the range $0.1 < \tan \delta < 1.2$.

Estimation of the total error

In order to define the accuracy of the proposed measurement setup various error sources have been investigated independently, as discussed above. Assuming that the individual errors are not correlated, the total error can be calculated with following equation [68]:

$$\frac{\delta_y^2}{y^2} = \frac{\left(\frac{\partial y}{\partial A_1}\right)^2 \delta_{A_1}^2 + \dots + \left(\frac{\partial y}{\partial A_n}\right)^2 \delta_{A_n}^2}{y^2} \quad (3.1)$$

where y is a function of A_1, \dots, A_n . A_1, \dots, A_n are n uncorrelated variables. $\delta_{A_1}, \dots, \delta_{A_n}$ are the variances of the corresponding random variables.

From the Eq. 3.1 and the Eq. 2.21 the error of ϵ_r' can be estimated to be:

$$\frac{\delta_{\epsilon_r' - 1}^2}{(\epsilon_r' - 1)^2} = \frac{\delta_A^2}{A^2} + 2 \left(\frac{f_1}{f_0 - f_1} \right)^2 \frac{\delta_f^2}{f^2} + \frac{\delta_{V_s}^2}{V_s^2} + \frac{\delta_{V_c}^2}{V_c^2} \quad (3.2)$$

The overall accuracy of ϵ_r' is estimated to be $\pm 1.5\%$. Similarly, it results from equations 2.22 and 3.1:

$$\frac{\delta_{\tan \delta}^2}{\tan \delta} = \frac{\delta_{\epsilon_r'}^2}{\epsilon_r'^2} + \frac{\delta_B^2}{B^2} + \frac{Q_0^2}{(Q_0 - Q_1)^2} \frac{\delta_{Q_1}^2}{Q_1^2} + \frac{Q_1^2}{(Q_0 - Q_1)^2} \frac{\delta_{Q_0}^2}{Q_0^2} + \frac{\delta_{V_s}^2}{V_s^2} + \frac{\delta_{V_c}^2}{V_c^2} \quad (3.3)$$

The overall error in the measured $\tan \delta$ is additionally dependent on the inaccuracy in the measured ϵ_r' , which is prerequired for the estimation of losses. From Eq. 3.3 it results in an accuracy of $\pm 8\%$.

3.2 Microwave calorimetry

In the present work, the approach from Nesbitt et al. [37] has been extended with advanced numerical simulations to enable a more qualitative thermal analysis of the MUT. Through the addition of the thermal analysis, for the first time the proposed method enabled the estimation of the specific heat capacity of MUT under microwave heating conditions. This system is proposed in [69].

The calorimetric analysis bases on the evaluation of the heat flow into or out from the MUT during a constant heating rate. In case of microwave calorimetry the microwave energy, which remains in the cavity (P_{abs}) is calculated from the microwave power balance in the cavity:

$$P_{abs} = P_{inc} - P_{refl} - P_{trans} \quad (3.4)$$

where P_{inc} and P_{refl} are the measured incident and reflected power. The transmitted power (P_{trans}) is assumed to be negligible. Furthermore, in order to specify the part of P_{abs} , responsible for the measured sample temperature

increase, the power measurements is extended by the simulative estimation of the wall losses, convection and conduction thermal losses.

3.2.1 Measurement setup

Two Anritsu power meters ML2487B and ML2495A are used for the measurement of the incident and the reflected power. The isolation between the incident and the reflected power is realized by using a bidirectional coupler of type Narda-ATM PNR CHP274-30F-30R. For accurate power measurements, the VNA and both power meters need a perfect synchronization, which is implemented by using a trigger signal generated by the VNA.

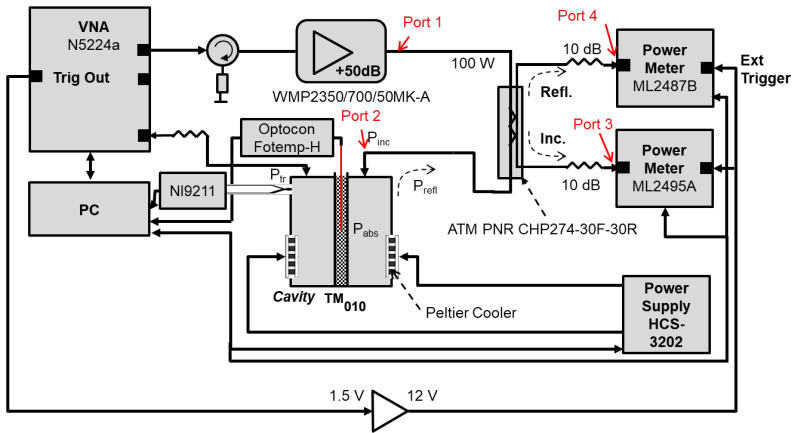


Figure 3.9: Block diagram of the power measurements system [69]

3.2.2 Calibration method

Calibration of the power measurements

A power calibration is required in order to obtain accurate values of the absorbed power based on Eq. Fehler! Textmarke nicht definiert.3.4. The VNA is used to measure the four-port scattering matrix (S-parameters). Those

four ports are the ports for the power meters (port 3 & 4), the power amplifier output (port 1) and the cavity input (port 2) (Fig. 3.9). The absolute values for the incident and the reflected power are calculated using the following equations [69]:

$$P_{refl} = \frac{P_4 \cdot S_{31}^2 - P_3 \cdot S_{41}^2}{S_{42}^2 \cdot S_{31}^2 - S_{32}^2 \cdot S_{41}^2} \quad (3.5)$$

$$P_{inc} = \frac{P_3 - P_{refl} \cdot S_{32}^2}{S_{31}^2} S_{12}^2 \quad (3.6)$$

P_3 and P_4 are the power levels at port 3 and port 4 respectively measured by the power meter (see Fig. 3.9) to monitor the incident and reflected power, respectively. The power meter is operated in the pulse-modulated mode with a gate time equal to the sweeping time of the VNA. This enables the input and reflected power to be determined very accurately by integration over a sweeping period of the VNA.

The measured frequency dependent S-parameters are shown in Fig. 3.10 and Fig. 3.11. It should be noted that the isolation between the incident and the reflected power is higher than 20 dB.

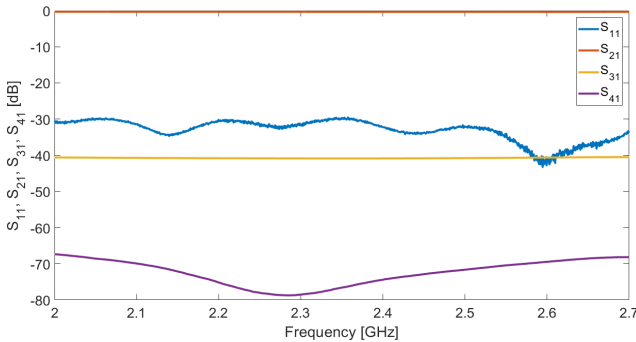


Figure 3.10: S-Parameters with excitation at port 1 of the power measurement system from Fig. 3.9

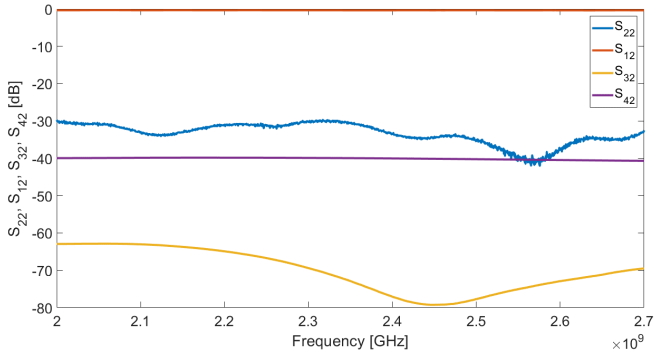


Figure 3.11: S-parameters with excitation at port 2 of the power measurement system from Fig. 3.9

In order to specify the part of P_{abs} , responsible for the measured increase in sample temperature, full-wave 3D simulations with CST Microwave are done. Based on these simulations the cavity wall losses can be estimated accurately. Additionally, the exact power distribution in the sample can be approximated. For a further improvement of the accuracy of the calorimetric measurements, the heat transfer losses from the sample are simulated with COMSOL Multiphysics. For the COMSOL modelling, the simulated power distribution from the model used in CST MWS is applied as heat source.

Estimation of the convection and conduction thermal losses

In this section, an analytical estimation of the convection and conduction of the thermal losses of the sample is done for a given sample temperature T_S . That estimation is valid for a system which consists of a glass tube with the inner radius r_i and the outer radius r_e . The length of the tube is l (Fig 3.12). It is assumed that the tube is completely filled with a liquid and placed in a microwave cavity, where a uniform electric field exists. Because of the homogeneity of the MUT and of the electric field, the power density is uniform inside the tube.

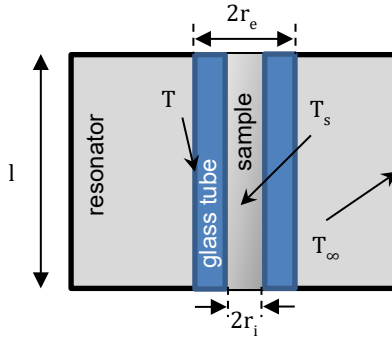


Figure 3.12: Resonator model with the correspondings temperature variables

The heat transfer by heat conduction from the MUT to the outer surface of the glass. The total conductive heat flow is given by the following equation [70]:

$$q_{conductive} = 2\pi k \frac{T - T_s}{\ln\left(\frac{r_e}{r_i}\right)} l \quad (3.7)$$

k is the thermal conductivity of the glass tube. T is the temperature of the outer surface of the glass tube.

Heat transfer by convection occurs from the wall of the glass tube to the cold air inside the cavity. The heat flux density q'' can be calculated if the convection coefficient h is known [71]:

$$q'' = h(T - T_\infty) \quad (3.8)$$

At this stage, the value of this coefficient is unknown, but from the literature [71], it is known that for natural convection cooling it is in the range of $5 - 20 \text{ W}/(\text{K m}^2)$.

The total heat transfer rate is obtained by integrating the heat flux at the surface of the glass tube with an outer radius r_e :

$$q = \int_0^{2\pi} \int_0^l q'' r_e d\phi dz = 2\pi r_e h l (T - T_\infty) \quad (3.9)$$

The Eq. 3.9 gives the total heat transfer rate in watt transferred from the hot tube to the air by natural convection, knowing the temperature at the surface of the glass tube T (Eq. 3.10), and the convection transfer coefficient h .

Assuming that no energy remains stored in the glass tube, the conductive heat flow from Eq. 3.7 should be equal to the convective heat flow from Eq. 3.9. This allows the temperature of the outer surface of the glass tube T to be determined as follows:

$$T = \frac{kT_s + hr_e \ln\left(\frac{r_i}{r_e}\right) T_\infty}{hr_e \ln\left(\frac{r_i}{r_e}\right) + k} \quad (3.10)$$

T_∞ corresponds to the temperature of the surrounding air in the cavity and is assumed to be equal to the cavity wall temperature.

The uniform absorbed power P_{MUT} by the MUT is given as follow:

$$P_{MUT} = mc_p \Delta T / \Delta t + 2\pi r_e h l (T - T_\infty) \quad (3.11)$$

m corresponds to the mass of the MUT. c_p is the specific heat capacity of the MUT. The first term from Eq. 3.11 represents the absorbed power needed to elevate the material temperature by ΔT in time Δt , the last term is the power transmitted to the surrounding air inside of the cavity by convection. From Eq. 3.11, the temperature rise ΔT can be calculated:

$$\Delta T = \frac{P_{MUT} - 2\pi r_e h l (T - T_\infty)}{mc_p} \Delta t \quad (3.12)$$

COMSOL model

Using a 2D axisymmetric model, a coupled fluid and thermal model is solved to obtain the convection flux and the transfer coefficient h . The model solves the laminar Navier-Stokes equation [71] together with the heat equation. The convection takes place due to the differences in the air density ρ_a caused by the temperature gradient. The volume force $f(r, z, t)$ in COMSOL is implemented as follows:

$$f(r, z, t) = g \cdot (\rho_a(r, z, t) - \rho_{ref}) \quad (3.13)$$

r and z represent the cylindrical coordinates and t is the time. $\rho_{ref} = 1.19 \text{ kg/m}^3$, is the density of air at an ambient temperature of 293 K and at a pressure of one bar. The volume force f at the location (r, z) and at the time t is proportional to the current local density. The earth gravity is given as g . The air is modelled as an ideal gas, and the density is expressed as a function of the temperature and pressure via the ideal gas law [72]:

$$p_a V_a = n_a R T = \frac{m_a}{M_a} R T = m_a \frac{R}{M_a} T = m_a R_a T. \quad (3.14)$$

$$p_a = \frac{m_a}{V_a} R_a T = \rho_a R_a T \quad (3.15)$$

$$\Rightarrow \rho_a = \frac{p_a}{R_a T} \quad (3.16)$$

$R = 8.3 \text{ J/(mol}\cdot\text{K)}$ is the universal gas constant and $M_a = 29 \text{ g/mol}$ is the molar mass of dry air. The specific gas constant for air is assumed to be $R_a = 286 \text{ J/(kg}\cdot\text{K)}$.

Geometry

The inner and outer radius of the glass tube are $r_i \approx 1.5 \text{ mm}$ and $r_e = 3 \text{ mm}$ respectively. The diameter and height of the cavity are 88 mm each.

Material properties

For the glass tube is assumed a density of $\rho = 2210 \text{ kg/m}^3$ [73]. The specific heat capacity c_p of the quartz tube is assumed to be 770 J/(kg K) and the thermal conductivity is assumed to be 1.4 W/(m K) [73]. The thermal properties of air are a function of temperature and follows the ideal gas law.

Power Calibration

The power calibration is performed in the following manner: firstly, the dielectric properties of the MUT and the incident and the reflected power are measured. Secondly, based on the measured dielectric properties, the electric field density and the wall losses in the cavity with CST microwave studio are estimated. Thirdly, the simulated data are used as input for the multi-physic modelling using COMSOL (see Fig. 3.13). Based on the material and geometry parameters mentioned above, the simulative estimated transfer coefficient h is $13 \text{ W/(m}^2 \text{ K)}$.

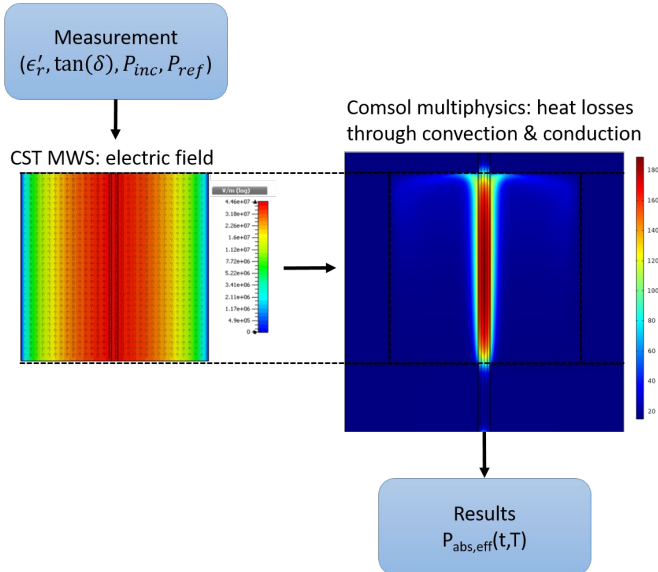


Figure 3.13: Power calibration methodology

3.2.3 Validation of the system performance

To validate the measurement system three known liquids have been measured. A sample with a radius of 1.5 mm is used to keep the power requirement as high as possible. In this way the absolute error on the heat capacity determination can be kept low since the energy required to heat the sample is much greater than the thermal or wall losses. All measurements of the specific heat capacities are made at a constant power level of 25 Watt for the incident power and a fixed frequency span of 0.1 MHz around the resonance frequency. In this way the influence of temperature control is minimized while maximizing the absorbed power, thus minimizing the relative error of the power measurements. Only in this way a determination of the heat capacity was possible.

Using water as a first sample, this results in an average absorbed power of 5.71 Watt. According to the simulations the wall losses amount to approximately 31 % of the absorbed power. From Eq. 3.9 the average thermal losses are calculated to be approx. 0.5 Watt. This results in an absorbed power of about 3.44 Watt, which is responsible for the heating of the water sample. From Eq. 3.11 the measured specific heat capacity is approx. 5.5 J/(g K).

The measured properties from the three measured liquids with the developed calorimeter and the literature values [74] are presented in Table 3.2.

Table 3.2: Comparison between measured and literature values of the specific heat capacity

Material	c_p [74] [J/(g·K)]	c_p (measured) [J/(g·K)]	c_p (corrected) [J/(g·K)]
Ethanol	2.4	3.2 ± 0.5	2.44
Ethylene glycol	2.2	2.8 ± 0.4	2.14
Water	4.2	5.5 ± 0.7	4.2

For all three liquids, the proposed microwave calorimetry shows the right order of the specific heat capacity. The most important sources of error are the

inaccuracy of the measured dielectric properties, the inaccuracy of the sample and cavity temperature measurements, the measured incident and reflected power and finally the error in the numerical calibration.

Table 3.2 shows a systematic overestimation of the measured heat capacities. A further improvement of the heat capacity determination can be achieved by an extended calibration of the measurements system by a known sample (e.g. water). This correction can be made by multiplying the measured specific heat capacity by the ratio between the actual and the measured value of the well-known material (reference material). In case of Table 3.2 and assuming that the heat capacity of water is well known and equal to $4.2 \text{ J}/(\text{g}\cdot\text{K})$, resulting in a correction factor of ~ 0.76 , the measured heat capacity of ethanol and ethylene glycol can be corrected to $2.44 \text{ J}/(\text{g}\cdot\text{K})$ and $2.14 \text{ J}/(\text{g}\cdot\text{K})$, respectively.

An important goal of calorimetric measurements is to find out the exothermic or endothermic behavior of the depolymerization reaction. Hence, it has to be investigated for known reactions, e.g. for the curing of epoxy resins. For this, a quartz tube with an inner diameter of 3 mm is completely filled with the epoxy resin 'Pattex Stabilit Express' [75]. On the basis of a material density of $1.172 \text{ g}/\text{cm}^3$ this amounts to a material quantity of 0.7357 g assuming a volume of 0.627 cm^3 . Fig. 3.14 shows the curing process of the epoxy resin with two different constant heating rates. More exactly, it shows the absorbed power measured during the curing process of an epoxy resin. An approximate linear increase of the absorbed power demand with increasing temperature can be recognized, which is due to an increased heat loss from the sample surface to the cold environment by conduction and convection. As soon as the exothermic polymerization reaction starts at about $80 \text{ }^\circ\text{C}$, the power requirement to maintain a constant heating rate decreases until the polymerization is completed. Furthermore, as the heating rate increases, the observed decrease in power demand during polymerization increases. In ideal case, the Fig. 3.14 provides a proper estimation of the energy released during the reaction. That energy can be calculated by integrating the surfaces 'area 1' and 'area 2'. The calculated energy is 416 J and 392 J from the 'area 1' and 'area 2', correspondingly. This corresponds to a released energy during the exothermic curing reaction between $532 \text{ J}/\text{g}$ and $565 \text{ J}/\text{g}$, which is comparable

to literature values of about 400 J/g for similar epoxy resins [76]. Taking water as reference material, the measured released energy during the reaction can be corrected to 406 J/g and 432 J/g.

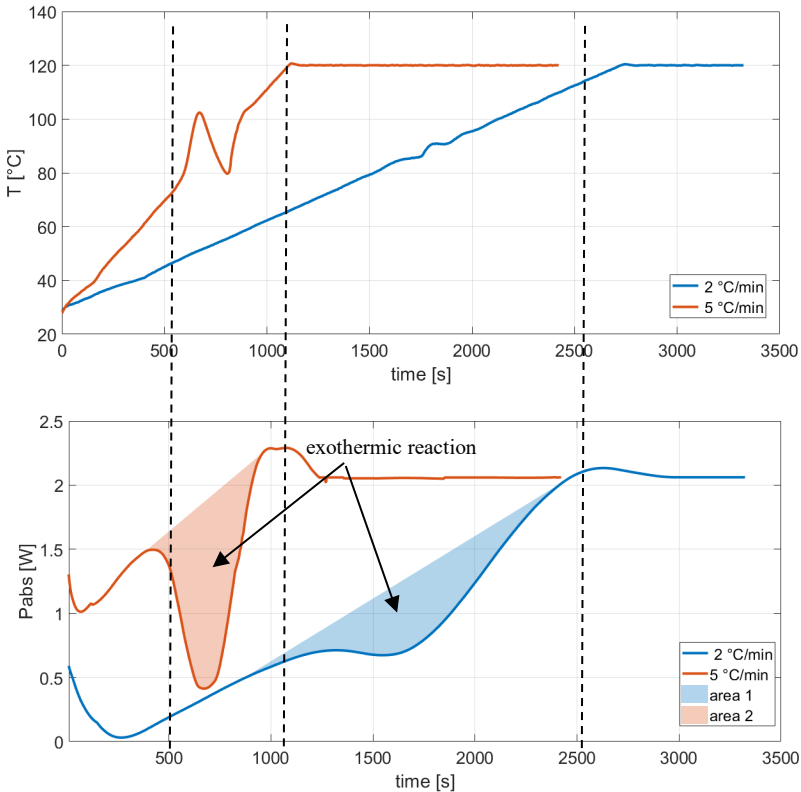


Figure 3.14: Calorimetric monitoring of curing of epoxy resins

The power measurements should fulfill two main goals. First, it should make an exothermic or endothermic behavior visible and second, the heat capacity of the investigated material should be determined. The inaccuracy of the power measurements should be investigated for systematic and random errors. Hereby, the systematic errors only affect the determination of the heat

capacity, since relative measurements are sufficient for the determination of the behavior of the reaction. The main error sources in the estimation of the incident and the reflected power can be calculated with the help of the equations 3.5 and 3.6. It follows that the errors are caused by the inaccuracy of the measured power signals P_3 and P_4 with the power meter and the inaccuracy of the measured S- parameters. According to [77] the systematic errors of the power sensors are about ± 4 % and the random errors are ± 0.11 %. The error of the measured S-parameters is about ± 0.01 dB [78]. It can be considered as a purely systematic error. These errors can be calibrated using a well-known sample (e.g. water). From Fig. 3.10 and 3.11 it can be seen that the transmission coefficients S_{32} and S_{41} are significantly smaller than the transmission coefficients S_{31} and S_{42} . This simplifies the equations 3.5 and 3.6 as follows:

$$P_{refl} \approx \frac{P_4}{S_{42}^2} \quad (3.17)$$

$$P_{inc} \approx \left(\frac{S_{12}}{S_{31}}\right)^2 P_3 \quad (3.18)$$

The equations 3.1, 3.17 and 3.18 result in

$$\delta_{P_{refl}} \approx \sqrt{\frac{\delta_{P_4}^2}{P_4^2} + 4 \frac{\delta_{S_{42}}^2}{S_{42}^2}} \quad (3.19)$$

$$\delta_{P_{inc}} \approx \sqrt{\frac{\delta_{P_3}^2}{P_3^2} + 4 \frac{\delta_{S_{12}}^2}{S_{12}^2} + 4 \frac{\delta_{S_{31}}^2}{S_{31}^2}} \quad (3.20)$$

For the calculated P_{inc} and P_{refl} this results in a systematic error of about ± 4.1 % and ± 4 %, respectively. Since the power levels of P_{inc} and P_{refl} are about 10 Watt, an error for P_{abs} of up to 0.8 Watt is feasible and accordingly the determination of the heat capacity is very imprecise. The random error in the calculation of P_{inc} and P_{refl} is about ± 0.11 % and a random error for P_{abs} of up to 0.022 Watt is feasible. It follows that the power measurements can be

considered as meaningful in the determination of the endothermic/exothermic behavior of the reaction.

3.3 Combined dielectric and calorimetric measurements

3.3.1 Measurements setup

Finally, both subsystems for the dielectric and calorimetric measurements were merged. This enables the simultaneous temperature dependent dielectric and calorimetric characterization of materials under microwave heating conditions. The block diagram of the measurement system is shown in Fig. 3.15.

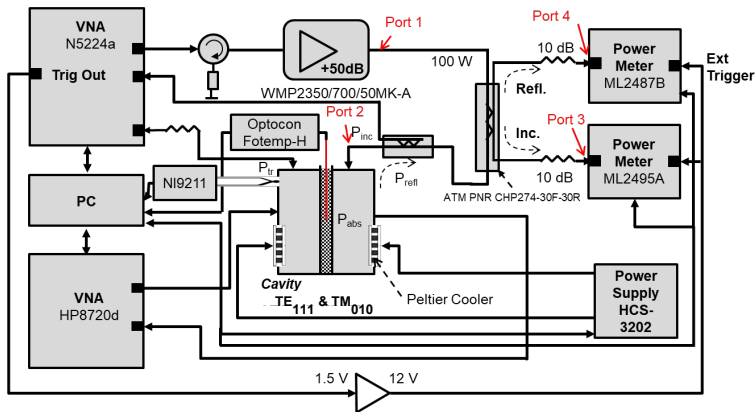


Figure 3.15: Block diagram of the measurements system

3.3.2 Automatic calibration and control system

Operation control and data acquisition are performed on a personal computer (PC) with the help of a MATLAB code. In the code, the standard commands for programmable instruments (SCPI) are used to control the I/O interfaces.

The network analyzer HP9720d is controlled via a remote general-purpose interface bus (remote GPIB). The second network analyzer N5224a is controlled via a local area network (LAN), as well as the two power meters. The power supply HCS-3202 control and the acquisition of the thermocouple data (NI9211) are controlled via USB ports. The Optocon fiber optic temperature sensor is controlled via RS-232 port. The software allows a loop-controlled operation including heating and data acquisition (see Fig. 3.16).

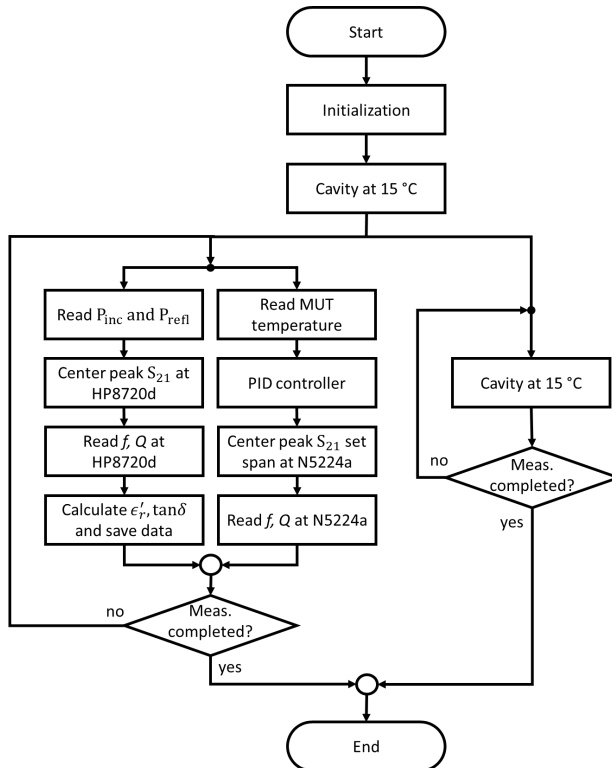


Figure 3.16: Scheme of the control of the dielectric and calorimetric measurements setup

The achievable control time is 0.5 s. In this setup the main restricting factor for the control time is the communication with the VNA, which is about 0.45 s. For this reason, the main code is parallelized. It consists of two well synchronized loops. The temperature stabilization of the resonator works independently during the measurements process. The structure of the developed control algorithm is shown in Fig. 3.16. Furthermore, a graphical user interface (GUI) for the implementation of fully-automated measurements has been developed.

The temperature control is carried out with the help of a proportional-integral-derivative (PID) controller. The PID controller uses as input the measured and the set temperature values and provides a frequency step as the output, which is added to the actual frequency. This span value is given as input to the VNA N5224a. The smaller the frequency step the larger the heating rate of the sample and vice versa.

The equation for the PID controller can be formulated as follows [79]:

$$d_{span} := K_p \cdot ((e - e_1) + K_I \cdot e + K_D \cdot (e - 2e_1 + e_2)) \quad (3.21)$$

where K_p, K_I, K_D are the proportional, integral and derivative gains, respectively. e, e_1, e_2 are the actual, previous and two times before error value, respectively. The error value is defined as the difference between a nominal temperature $T_{nominal}$ and an actual temperature T_{actual} . For the developed measurement setup the following control constants were determined experimentally with the help of a multi-step temperature scenario (see Fig. 3.17): $K_p = 0.65, K_I = 0.28, K_D = 0$.

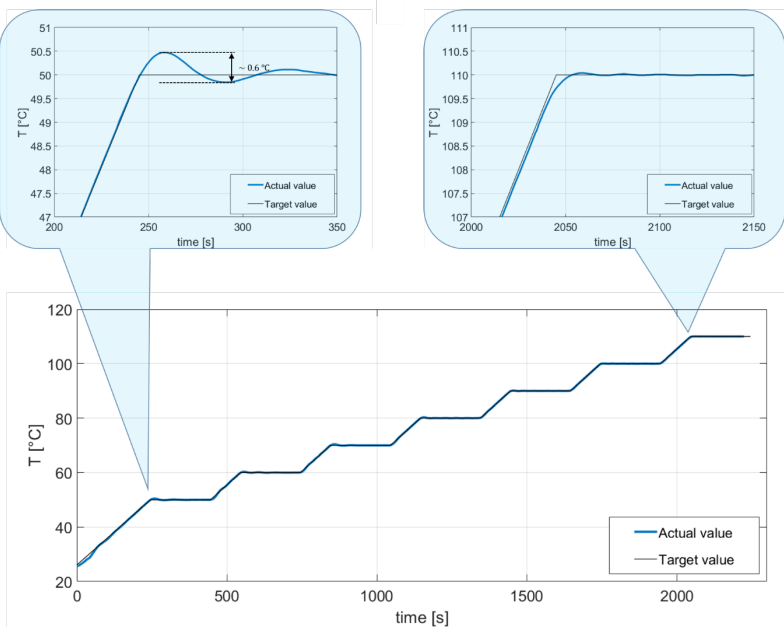


Figure 3.17: Example of temperature control with optimized PID controller parameters

The starting parameters of the PID controller are selected in a way that an overshooting at the beginning of the process (close to room temperature) is avoided. Otherwise, the settling time of the PID controller would be very long due to the lack of an active cooling. Fig. 3.17 shows that the higher the actual temperature is the shorter the settling time and the lower the overshoot becomes. This can be explained by the increasing conduction and convection heat losses due to the cold environment. That enables a faster and more accurate reaction to the temperature by variation of the microwave power.

In ideal case, the short control time in combination with the PID controller allows accurate temperature control with a maximum deviation from the preset temperature profile of about ± 0.3 °C. But as the dielectric loss tangent becomes larger ($\tan \delta > 0.5$), the temperature control becomes more and more complex. Because of the very high dielectric losses the microwave cavity

develops a very low-quality factor and therefore becomes very broadband. Accordingly, the variation of the microwave power and the corresponding temperature control can be realized in a very restricted way, since all the temperature control is done by the frequency span variation. In that case, greater temperature fluctuation of up to ± 3 °C are common.

3.4 Measurements using the coaxial probe

In the present work, the various reactants are partially measured depending on temperature and frequency by using a commercial coaxial probe of type HP85070B [80]. The coaxial probe enables the dielectric characterization of materials from DC up to 20 GHz in the temperature range from -40 °C to +200 °C. The typical accuracy is ± 5 % for the dielectric constant and ± 0.05 for the dielectric loss tangent [81]. A magnetic hotplate stirrer VWR VMS-C7 is used for the controlled heating of the liquid probe up to 100 °C. A picture of the measurement setup is shown in the Fig. 3.18.

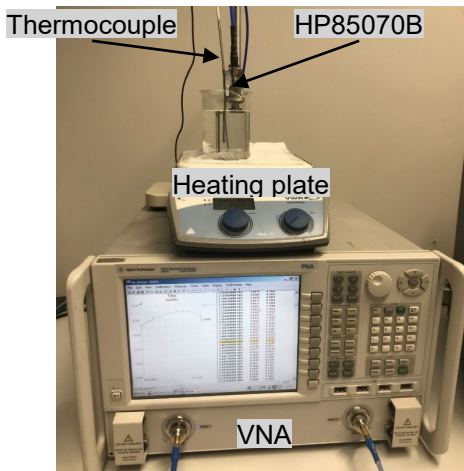


Figure 3.18: Measurement setup based on commercial coaxial probe HP85070B

4 Dielectric and calorimetric measurement results

4.1 Sample preparation

For the following measurements, MEG and PTA with a purity grade of $\geq 99\%$ and $\geq 98\%$, are obtained from company Alfa Aesar. NaOH with a purity of $\geq 99\%$. is obtained from company Merck Millipore. The PET particle size is about $500\ \mu\text{m}$ (see Fig. 5.13).

Table 4.1: Mixture composition at the different reaction steps

Reaction progress	PET		PTA		MEG		Water		NaOH	
	g	mol	g	mol	g	mol	g	mol	g	mol
0	180	0.94	0	0.00	955	15.39	140	7.78	82.4	2.06
10	162	0.84	15.6	0.09	960	15.48	140	7.78	82.4	2.06
20	144	0.75	31.1	0.19	966	15.57	140	7.78	82.4	2.06
30	126	0.66	46.7	0.28	972	15.67	140	7.78	82.4	2.06
40	108	0.56	62.2	0.38	978	15.76	140	7.78	82.4	2.06
50	90	0.47	77.8	0.47	984	15.85	140	7.78	82.4	2.06
60	72	0.38	93.3	0.56	989	15.95	140	7.78	82.4	2.06
70	54	0.28	108.9	0.66	995	16.04	140	7.78	82.4	2.06
80	36	0.19	124.5	0.75	1000	16.14	140	7.78	82.4	2.06
90	18	0.09	140.0	0.84	1007	16.23	140	7.78	82.4	2.06
100	0	0.00	155.6	0.94	1013	16.32	140	7.78	82.4	2.06

In Table 4.1 different chemical mixtures are given. Each mixture represents a different level of the reaction progress, e.g. 0 % is equal to a status of no depolymerization, whereas 100 % is equal to full depolymerization. As expected by eq. 2.23, one mol PET reacts with two mol NaOH. It yields one mol PTA and one mol Na_2PTA . Since Na_2PTA is not directly available as a substance, here NaOH and PTA are mixed. It yields to Na_2PTA .

4.2 Dielectric measurement results

4.2.1 Dielectric properties of the reaction mixture

The samples have been prepared just prior to the individual measurements, to avoid any reaction before the actual measurement. The measurement procedure including constant heating up to 180 °C and subsequent controlled cooling did last approximately one hour. Eleven samples are tested with a depolymerization level of 0 % up to 100 % as shown in Table 4.1.

In Fig. 4.1, the time- and temperature-dependent dielectric properties of the reaction mixture with PET/PTA are presented. During the experiment, the heating rate was chosen to be 3 °C/min and the cooling rate -5 °C/min. Larger heating rates were not feasible because of the long reaction time of the thermo-sensor, the risk for boiling within the sample volume and leaking problems of the sample from the sample holder. During the initial experiments such problems were noticed as well as the local heating of the inner glass tube surface which was affecting the glass itself in a way that it could not be cleaned any more.

Fig. 4.1 shows the temperature-dependent properties during heating and cooling of the samples. The direct comparison of the heating and cooling scenarios for 0 % depolymerization (red curve) reveals information about the influence of the chemical process onto the dielectric constant and dielectric loss. Both show higher values during heating as compared to the cooling scheme. The sample '100 % depolymerized' (green line), which represents the dielectric properties of finished chemical depolymerization, follows quite well the cooling curve of sample '0 % depolymerized', indicating that the chemical process is finished as soon as the target temperature of 180 °C is reached. This is probably due to the slow heating rate of 3 °C/min as well as by the fact that the PET used was a fine powder. In case of faster heating or larger PET particles still some isothermal dwell at the targeted reaction temperature might be needed. Due to the low heating rate, the direct characterization of the mixtures at a process temperature of 180 °C was not possible since the

chemical reaction already started during the heating and obviously finished before the target temperature was reached.

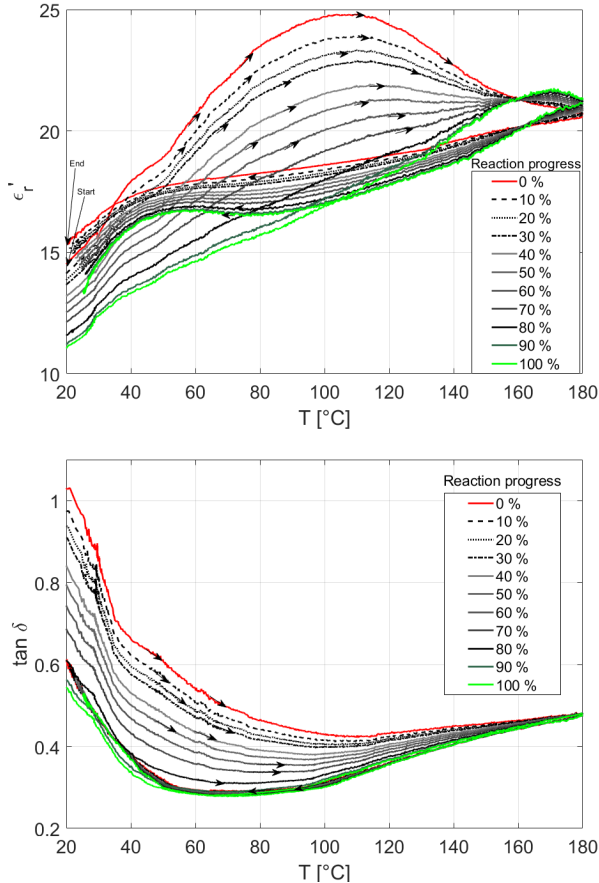


Figure 4.1: Temperature dependent permittivity for all samples according to Table 4.1

Three different effects that take place during heating can explain the main course of the dielectric parameters from Fig 4.1. First, the dielectric properties of MEG (see Fig 8.1) dominates, which also forms a large volume fraction

(~74 %) of the total mixture. This factor is mainly responsible for the strong reduction of $\tan \delta$ at the beginning of the heating phase and the simultaneous increase of ϵ'_r . At the same time, the conductivity losses caused by NaOH increases with the temperature (see Fig 8.2). Due to these losses, the slide increase of $\tan \delta$ can be explained by temperatures $T > 80$ °C). And finally the depolymerization reaction, which leads to an effective reduction of the NaOH concentration. The effective reduction of the concentration of unbound NaOH may be responsible for the reduction of $\tan \delta$.

For the latter system design the permittivity measured for the sample '0 % depolymerized' is most relevant since it represents the dielectric properties along the full process. The corresponding properties for all samples according to Table 4.1 at room temperature and at 180 °C after heating with a heating rate of 3 °C/min are listed in Table 4.2.

Table 4.2: Measured dielectric properties for the mixtures listed in Table 4.1

Reaction progress [%]	ϵ'_r @ 25 °C	ϵ'_r @ 180 °C	$\tan \delta$ @ 25 °C	$\tan \delta$ @ 180 °C
0	14.9	21.2	0.95	0.47
10	14.7	20.8	0.91	0.48
20	14.4	20.9	0.85	0.48
30	14.2	20.9	0.82	0.48
40	13.8	21.0	0.76	0.48
50	13.5	21.0	0.71	0.48
60	13.1	21.1	0.67	0.48
70	12.6	21.1	0.61	0.48
80	12.0	21.1	0.55	0.48
90	11.7	21.2	0.51	0.48
100	11.6	21.1	0.49	0.48

It must be mentioned, that all samples are 100 % depolymerized as soon as the target temperature of 180 °C is reached. This explains why all samples show the same permittivity at 180 °C. A future applicator must be able to work efficiently over the full range of permittivities, which means for a permittivity $15 < \epsilon'_r < 25$. The difference between the heating and cooling scenario for 100 % depolymerization (green curve) may be explained at least

partially by a temperature demand to enable the binding of NaOH and PTA to Na_2^+PTA . This can be investigated by the permittivity curve of the re-heated sample. A re-heating of the sample is only possible up to approx. 100 °C, because the chemicals damage the glass fiber sensor after a certain time and a repair/replacement becomes necessary. From Fig. 4.2 is evident that the direction of the permittivity during the cooling down process is very similar to that of the re-heated reaction mixture.

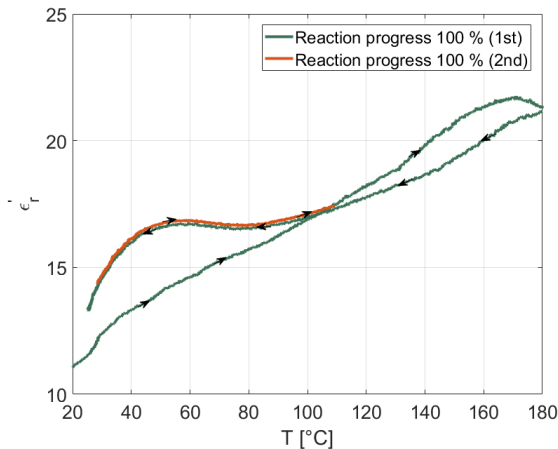


Figure 4.2: Temperature dependence of ϵ'_r for sample 'Reaction progress 100 %' according to Table 4.1 incl. re-heating

An important parameter that can act as an indicator for a maximum material thickness is the penetration depth D_p . [82]. Based on the measured dielectric properties (Fig. 4.1) and the Eq. 2.6 the penetration depth during the reaction can be calculated. Fig. 4.3 shows the behavior of the penetration depth with temperature and reaction progress. As can be seen in the graph the lowest penetration depth is estimated to be about 5.5 mm at 25 °C.

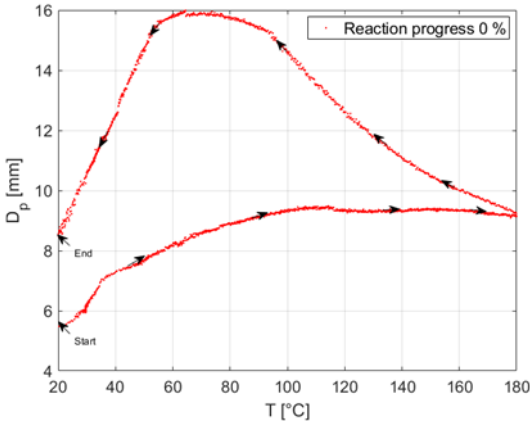


Figure 4.3: D_p of the sample ‘Reaction progress 0 %’

4.2.2 Dielectric properties of the initial mixture

For the modelling of the reaction, the temperature-dependent loss factor of the reactant (initial mixture), the reaction mixture (initial mixture during the reaction), and the reaction product (final mixture) as well as the time-dependent dielectric losses of the reaction mixture have to be known.

As mentioned in section 4.2.1, it is not possible to characterize directly the temperature-dependent properties of the reactants, because the reactants start reacting already at low temperatures. At the same time a very fast heating of the mixture is not possible due to the slow temperature sensor. Therefore, the temperature-dependent ‘initial mixture’ is measured in two steps, separating the reactant from the PET. In this way, a reaction during the heating process can be avoided. Firstly, the mixture consisting of mono ethylene glycol, water and NaOH is measured up to 180 °C. Secondly, the loss factor from virgin PET is measured separately up to 180 °C.

For the dielectric characterization of PET a measuring system based on the TE₁₁₁-Mode was used. The detailed description of this measurement setup can be found in [83]. A cylindrical sample with a diameter of 7.8 mm and a length

of 10 mm was used for this measurement. The measured dielectric properties are shown in figures 4.4.

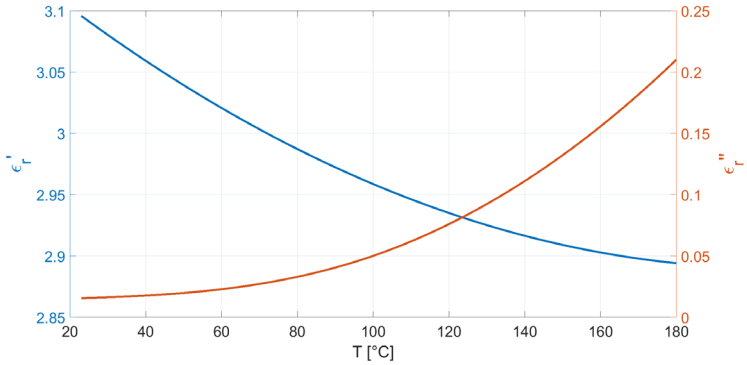
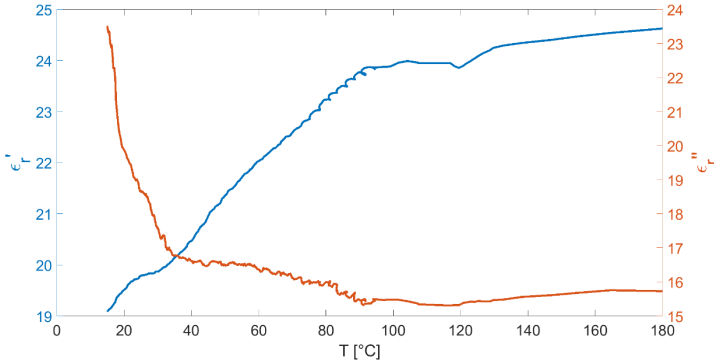


Figure 4.4: Dielectric properties of PET

For the characterization of the reaction mixture without PET the dual mode system is used. The measured dielectric properties are shown in figures 4.5. The highly noisy dielectric parameter of MEG, H₂O and NaOH without PET in Fig. 4.5 is explained due to the very high dielectric losses ($\tan \delta \sim 1$). In this range, both the temperature control and the measurement accuracy of the system reaches its limits. In any case, these results are sufficient for further consideration.

Figure 4.5: Dielectric properties of MEG, H₂O and NaOH

From the figures 4.4 and 4.5 is evident that the permittivity of PET is much smaller than that of the rest of the reaction mixture. Accordingly, PET does not significantly influence the course of the permittivity of the unreacted mixture.

The temperature dependent dielectric properties of the mixture are calculated using Eq. 2.8 with the LR exponential factor $\zeta = 1$. The mixing formulas for the dielectric properties of the full reaction mixture are as follows:

$$\epsilon'_{rL} = V_{L-PET}\epsilon'_{rL-PET} + (1 - V_{L-PET})\epsilon'_{rPET} \quad (4.1)$$

$$\epsilon''_{rL} = V_{L-PET}\epsilon''_{rL-PET} + (1 - V_{L-PET})\epsilon''_{rPET} \quad (4.2)$$

$$\tan \delta_L = \epsilon''_{rL} / \epsilon'_{rL} \quad (4.3)$$

V_{L-PET} is the volume percentage of H₂O, NaOH and MEG in the mixture at the beginning of the reaction. The dielectric constant of the full-unreacted reaction mixture, reaction mixture except of PET (consisting of H₂O, NaOH and MEG) and PET are ϵ'_{rL} , ϵ'_{rL-PET} and ϵ'_{rPET} , respectively, and ϵ''_{rL} , ϵ''_{rL-PET} and ϵ''_{rPET} are the corresponding loss factors. The volume percentage of PET in the reaction mixture is 11 %, from a PET density of 1.38 g/cm³ [84], MEG density of 1.11 g/cm³ [85] and NaOH density of 2.13 g/cm³ [86]. The calculated $\tan \delta$ for the full reaction mixture, based on measurement results

given in Fig 4.4 and 4.5 following eqs. (4.1) to (4.3) is shown in Fig. 4.6. This process can be described similar to the process shown in Fig. 4.1, based on the dielectric losses of MEG (Fig 8.1) and NaOH (Fig 8.2).

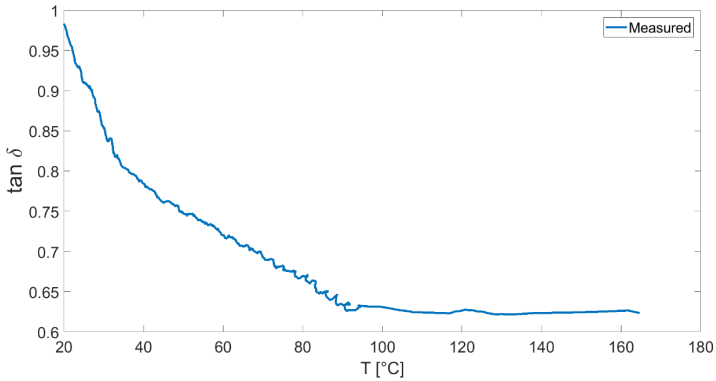


Figure 4.6: $\tan \delta$ of the unreacted mixture consisting of MEG, H_2O , NaOH and PET

4.2.3 Dielectric properties of reactants measured with coaxial probe

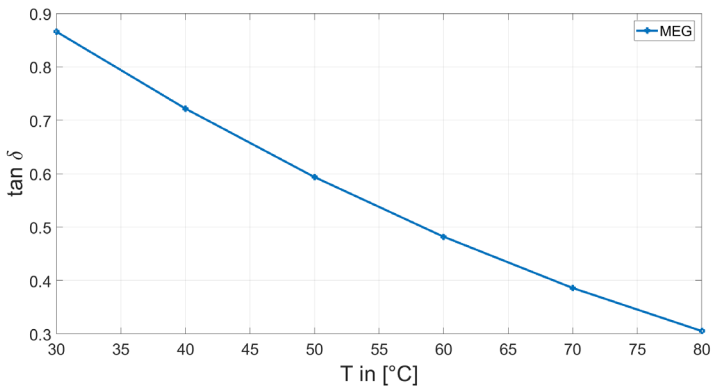


Figure 4.7: Measured dielectric loss tangent of MEG for six different temperatures.

Due to the very high dielectric losses of NaOH and MEG, the dielectric properties of the liquid components of the reaction product have been measured at different temperatures with the coaxial probe HP 85070B (see section 3.4).

Since the reaction mixture consists mainly of MEG, the loss tangent of MEG is firstly considered separately for six different temperatures (30 °C, 40 °C, 50 °C, 60 °C, 70 °C and 80 °C). The measured data is shown in Fig. 4.7.

Furthermore, due to the expected high conductivity of the NaOH solution [87], the NaOH concentration influences the total permittivity strongly. For a more detailed analysis, a separate consideration of the NaOH solution has been realized with the coaxial probe method. In each measurement series a different concentration of NaOH (5 wt.%, 7.5 wt.%, 10 wt.% and 15 wt.%) is used and the complex permittivity is measured for the six different temperatures (30 °C, 40 °C, 50 °C, 60 °C, 70 °C and 80 °C).

The weight fraction of NaOH in water is defined as the NaOH mass divided by the total mass.

In Fig. 4.8 the dielectric losses versus temperature for the different NaOH concentrations at 2.45 GHz are shown. According to Fig. 4.8, the losses are related to the temperature. An increase in the concentration of NaOH, leads to a significantly greater temperature dependence of the losses and higher losses. This phenomenon has already been described in [88].

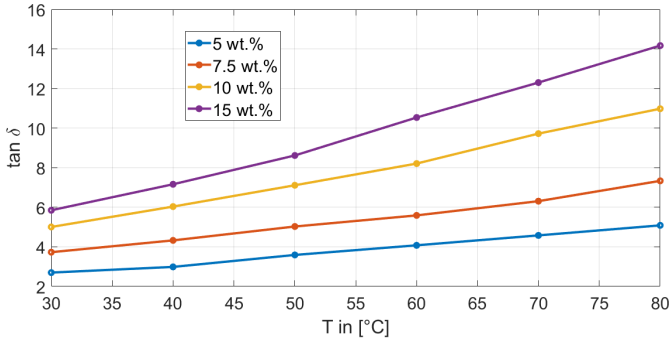


Figure 4.8: NaOH solution: loss tangent versus temperature for four NaOH concentrations

In addition, the dielectric loss tangents of the entire mixture consisting of NaOH, H₂O and MEG is characterized. Thereby a fixed weight ratio between NaOH and water (37 wt.% according to Table 4.1) was used. The concentrations mentioned are to be understood as weight of NaOH in relation to the weight of NaOH, H₂O and MEG. In Fig. 4.9 the dielectric loss tangents versus temperature for the different NaOH concentrations at 2.45 GHz are shown.

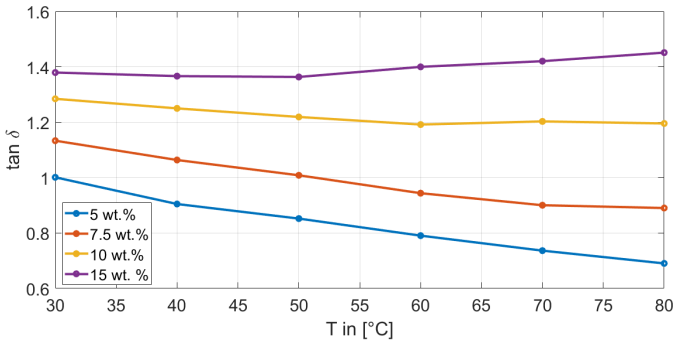


Figure 4.9: NaOH, H₂O and MEG solution: loss tangent versus temperature for four NaOH concentrations

In order to derive a mathematical expression for describing the concentration dependency, a fitting routine is used. This provides an approximation for the losses over the NaOH concentration for a selected frequency at room temperature (see Eq. 4.4). Here too, the weight proportion between NaOH and water was fixed at 37 wt.%. The resulting progression at room temperature for different concentrations is shown in Fig. 4.10. From Fig.4.10 it is visible that the dielectric losses follow a path that reaches its maximum for a concentration of approximately 15 wt.%. Similar behavior of the NaOH conductivity is reported in [89]. The dielectric losses across the NaOH concentration can be fitted with a polynomial of third order (see [89]). A comparison of the approximated and measured parameters in Fig. 5.11 shows a very good match. The expected error through these fitting is less than 2 %.

$$\tan \delta_{L-PET,RT} = a_3 c_{\text{NaOH}}^3 + a_2 c_{\text{NaOH}}^2 + a_1 c_{\text{NaOH}} + a_0 \quad (4.4)$$

where the coefficients $a_3 = 5.425 \cdot 10^{-5}$, $a_2 = -4.392 \cdot 10^{-3}$, $a_1 = 0.1012$ and $a_0 = 0.5912$

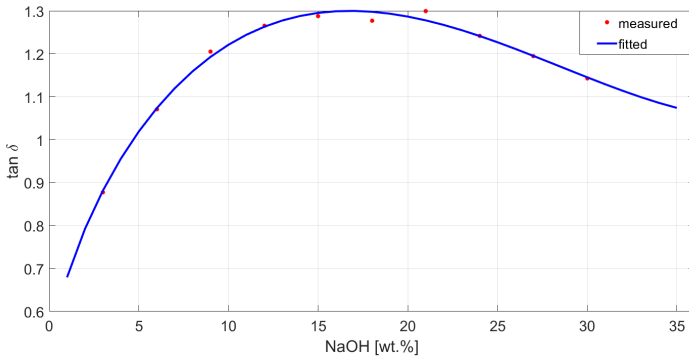


Figure 4.10: Measured and fitted $\tan \delta$ from NaOH with water and MEG at room temperature

From Eq. 2.23 it becomes evident that during the alkaline hydrolysis of PET one mole of PET reacts with two mole of NaOH. During the reaction NaOH binds to $\text{Na}_2[\text{PTA}]$. This effect leads to an effective reduction of the NaOH

concentration. The dielectric losses of NaOH are disproportionately higher than those from the total mixture. This is why a prevalence of the dielectric losses throughout the reaction from NaOH is expected.

In the literature, the molar weight of PET and NaOH are given as 192.2 g/mol and 39.997 g/mol, respectively. Under the assumption that the effective dielectric loss during the reaction changes due to the precipitation of disodium terephthalate and resulting reduction of ionic conductivity, the loss tangent development can be modelled based on the data in section 4.2. From Eq. 2.23 it is obvious that the degree of conversion is linearly proportional to the change of NaOH concentration. Depending on the reaction stage the NaOH concentration c_{NaOH} changes between 6.07 and 0.55 wt.% of the total reaction mixture. Therefore, the relationship between the degree of reaction and the NaOH concentration can be described as follows

$$c_{\text{NaOH}} = 5.52 \cdot (1 - \alpha) + 0.55 \quad (4.5)$$

4.3 Calorimetric measurement results

In Fig. 4.11, the time-dependent absorbed power of the reaction mixture with PET/PTA is plotted. The heating rate is 3 °C/min. Those measurements are realized in parallel to the measurements from section 4.2. Due to the slow heating rates and the permittivities measured in section 4.2, it can be assumed that the reaction mixture is completely reacted during the heating phase. Hence, only the heating phase is considered for the further analysis.

The absorbed power shows an irregular progression for temperatures < 30 °C. This can be explained by the time the controller needs to adjust the heating parameters. The direct comparison of the heating scenarios for ‘0 % depolymerization’ (blue curve) and ‘100 % depolymerization’ (orange line) is expected to reveal information about the exothermic and endothermic behavior of the chemical processes, respectively. The MUT weighted approximately 0.335 g. The integration of the gray area ‘Area 1’ in Fig. 4.11 results in released energy from ~526 J, which under correction with the

reference material water to a released energy of about ~ 368 J follows, that corresponds to released energy of ~ 1591 kJ/mol. This value is comparable with the values referred in [58]. Due to the uncertainty of the power measurements, further modeling of the reaction kinetics is realized based on the permittivity measurements.

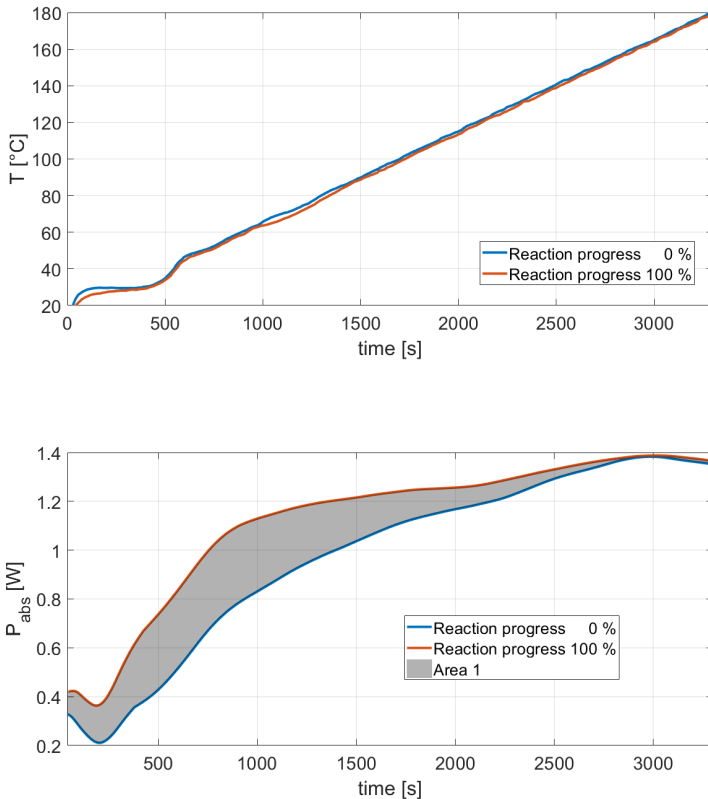


Figure 4.11: Time dependence of absorbed power during the depolymerization of PET and of the reaction product according to Table 4.1

5 Modelling of the reaction kinetics based on $\tan \delta$

This chapter describes a novel modelling approach to describe the loss factor of the reaction mixture during the alkaline hydrolysis of PET, which takes into account a progressive decrease in the surface area of the PET particles, in contrast to comparable studies [90].

5.1 Data preparation for modelling

For the modelling of the reaction kinetics, the data of the reaction product and of the reaction mixture during the reaction are needed. The measured $\tan \delta$ data of the reaction product (Sample ‘Reaction progress 100 %’) versus temperature can be seen in Fig. 5.1. The corresponding fitted data used for the further modelling can be found in the Appendix.

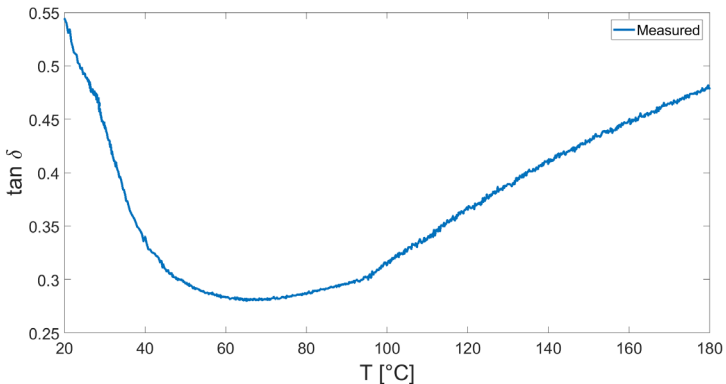


Figure 5.1: Loss tangent of the reaction product

Fig. 5.2 and Fig. 5.3 show measured data in dependence of the temperature and time during the reaction under a heating rate of $3\text{ }^{\circ}\text{C}/\text{min}$, respectively. These data correspond to the sample ‘Reaction progress 0 %’ from Table 4.1. Fig. 5.3 shows a plateau in the time range $< 400\text{ s}$ (red circle). This is caused by the settling time of the PID controller and has nothing to do with the reaction itself.

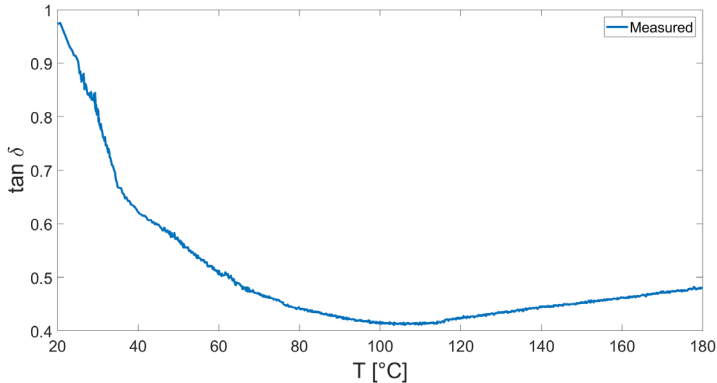


Figure 5.2: Temperature dependence of the loss factor during the reaction ($dT/dt = 3\text{ }^{\circ}\text{C}/\text{min}$)

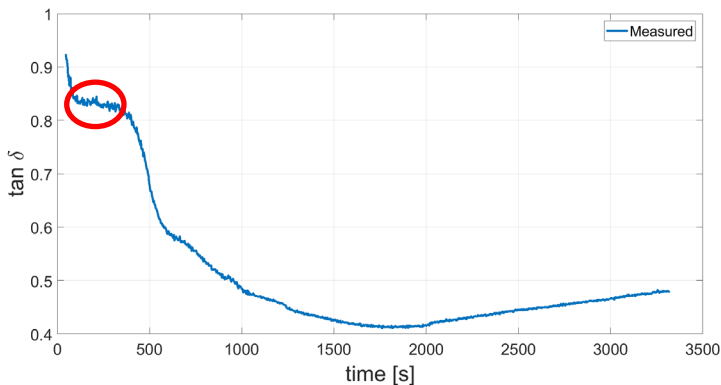


Figure 5.3: Time dependence of the loss factor during the reaction ($dT/dt = 3\text{ }^{\circ}\text{C}/\text{min}$)

In order to enable a calculation with Matlab, the measured data were described for later modelling by analytical functions. Fig. 5.4 shows the fitted curves of the mixtures at their different stages: unreacted (solid black line), reacted (dashed black line) and during the reaction (dotted black line) (see Appendix A). The red area corresponds to the portion of the mixture that has reacted and the green area to the portion of the unreacted mixture.

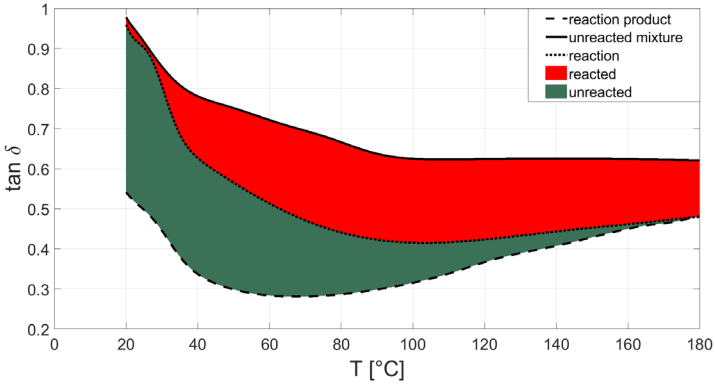


Figure 5.4: Temperature dependence of the $\tan \delta$ of the unreacted mixture, reaction product and during the reaction

5.2 Reaction model

By substituting Eq. 4.6 in Eq. 4.5, the $\tan \delta_{L-PET,RT}$ at room temperature can be calculated as follows

$$\begin{aligned} \tan \delta_{L-PET,RT} &= a_3 (5.52(1 - \alpha) + 0.55)^3 + a_2(5.52(1 - \alpha) + 0.55)^2 \\ &+ a_1(5.52(1 - \alpha) + 0.55) + a_0 \end{aligned} \quad (5.1)$$

For the modelling, Eq. 2.9 is used to mix $\tan \delta_{L-PET,RT}$ calculated using Eq. 5.1 with $\tan \delta_{PET}$ (see Fig. 4.4). The fractional volume of PET V_{PET} is assumed to be $\sim 11\%$ (see Table 4.1). It is also assumed that the density and dielectric losses of PET and PTA are the same. From Eq. 2.9 the total loss tangent at room temperature can be calculated as follows

$$\tan \delta_{L,RT} = V_{L-PET} \cdot \tan \delta_{L-PET,RT} + (1 - V_{L-PET}) \cdot \tan \delta_{PET,RT} \quad (5.2)$$

In Fig. 5.5, the modelled development of $\tan \delta$ versus the degree of the reaction (with the help of Eq. 5.3) is presented. A good agreement between the modelled and measured parameter (see Table 4.2) is evident. The maximum deviation between the measured and modelled $\tan \delta$ is $\leq 3\%$, which leads according to Table 4.2 to an incorrect estimation of the actual reaction stage of up to 6%.

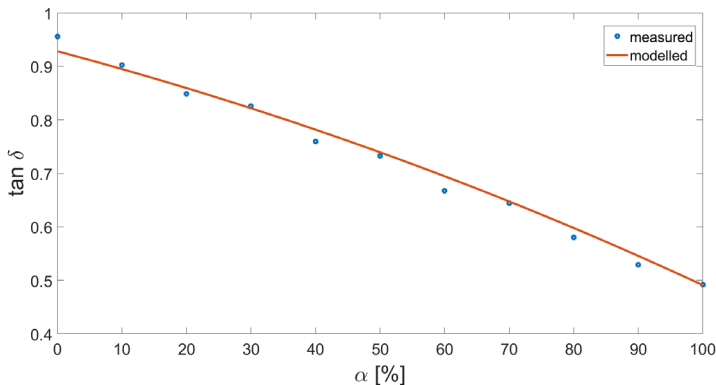


Figure 5.5: Measured and simulated $\tan \delta_{L,RT}$ during the reaction at room temperature

Under the assumption that $\tan \delta$ behaves similar at room temperature (see Fig. 4.8), $\tan \delta$ of the reaction mixture can be easily estimated over T with the help of Eqs. 5.2, 8.3 and 8.4.

$$\begin{aligned} \tan \delta_L &= \tan \delta_{End} + (\tan \delta_{L,RT} - \tan \delta_{End,RT}) \\ &\cdot \frac{\tan \delta_{Start} - \tan \delta_{End}}{\tan \delta_{Start,RT} - \tan \delta_{End,RT}} \end{aligned} \quad (5.3)$$

$\tan \delta_{Start,RT}$ and $\tan \delta_{End,RT}$ are the dielectric losses of the unreacted reaction mixture and the reaction product, respectively. These can be easily calculated from Eqs. 8.3 and 8.4 for $T = 20$ °C. In this way, the measured $\tan \delta$ can be converted to the corresponding reaction degree.

The corresponding temperature dependent $\tan \delta_L$ of the reaction mixture over the reaction progress is shown in Fig. 5.6.

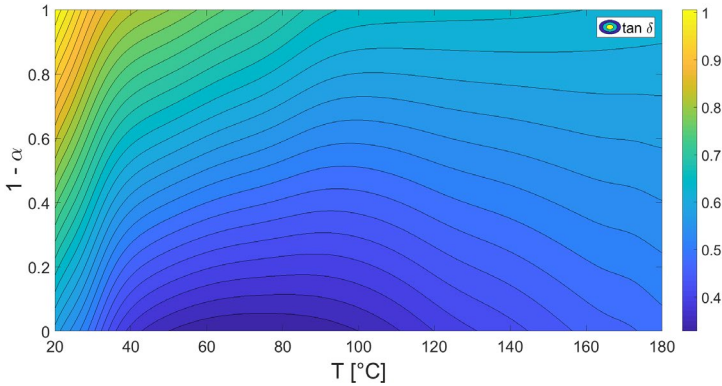


Figure 5.6: Temperature dependent $\tan \delta_L$ of the reaction mixture over the reaction

The reaction degree α results from a continuous integration over time. In general, the reaction degree can be derived from the following differential equation [91]:

$$\frac{\Delta\alpha}{\Delta t} = \kappa \cdot f \quad (5.4)$$

f as function of α comprises the reaction model and κ is the temperature dependent reaction rate that is given by the Arrhenius formula [92].

$$\kappa = Ae^{\left(-\frac{E_a}{RT}\right)} \quad (5.5)$$

$R = 8.3144598$ J/(mol K) is the universal gas constant. A is the Arrhenius constant and E_a is the activation energy. The latter is the energy required to start a chemical reaction.

Depending on the type of reaction or the function of the reaction mechanism, $f(\alpha)$ can be expressed by different formulas [91]. In case of the alkaline hydrolysis of PET, $f(\alpha)$ has been reported as follows [90]:

$$f = N_{As} \cdot V^{-b_r} \cdot N_{Ai}^{b_r-1} \cdot (M - 2\alpha)^{b_r} \quad (5.6)$$

where

- α represents the degree of the PET conversion,
- N_{As} is the surface area of the PET flakes,
- V is the total reaction volume,
- N_{Ai} is the moles of PET repeating units,
- M is the molar ratio of NaOH and PET,
- and, finally b_r is the reaction rate order.

The order of the reaction rate refers to the power dependence of the rate on the concentration of the individual reactants [93]. In a first-order reaction, the rate is therefore dependent on the concentration of the single species. A second-order reaction refers to a reaction whose rate depends on the square of the concentration of a single reactant or the combined first-order dependence of the rate on the concentrations of two different reactants [93]. According to [90], in case of alkaline hydrolysis of PET the reaction rate b_r is a first order

reaction. Here, for the further calculations b_r is set equal one. Accordingly, from equations 5.4, 5.5 and 5.6 follows.

$$\frac{\Delta\alpha}{\Delta t} = \kappa \cdot N_{As} \cdot (M - 2\alpha)/V \quad (5.7)$$

In Eq. 5.7 all parameters are known or measured except κ .

The PET mass during the reaction changes proportionally to $1 - \alpha$. The volume of PET V_{PET} is calculated from the mass divided by the density of 1.38 g/cm^3 [84]. For further calculation, it is assumed that the PET particles are spherical. Accordingly, the surface area of PET N_{As} changes proportionally to $V_{PET}^{2/3}$. The initial PET particle diameter was measured with the help of an optical microscope (see Fig. 5.7). In [90], it is assumed that the PET particle surface remains constant. Different to [90], a progressive decrease of the particles surface is considered in the following model approach. This should allow a more precise determination of the reaction kinetics.



Figure 5.7: Microscope pictures of the PET particles

The degree of PET conversion α can be calculated from the measured $\tan \delta$ and temperature T (Fig 5.2) with the help of Fig. 5.6. The calculated α can be

assigned to the corresponding t with the help of Fig 5.3. The time interval between two measurements is approximately $\Delta t \sim 0.5$ s. It is assumed that there is no temperature change between two measurements points. Subsequently, on the basis of the discretely estimated time- and temperature-dependent α , $\Delta\alpha/\Delta t$ can gradually be estimated by the different temperatures.

A table can be created in which $\Delta\alpha/\Delta t$, T and N_{As} data are assigned to each other. By solving Eq. 5.7 to κ and substituting the variables from the above table, the Arrhenius plot can be calculated. The Arrhenius plot shows the logarithm of the reaction rate constant $\ln\kappa$ over the reciprocal of the temperature $1/T$ [94]. Fig. 5.8 shows the corresponding Arrhenius plot. In this figure, the measured data is fitted with a straight line, because, according to Eq. 5.5, for the numerical value $\{\kappa\}$ of κ , $\ln\{\kappa\}$ is linearly dependent on $1/T$. The maximum deviation of κ as a function of the temperature from the fitted results is $\leq 4\%$.

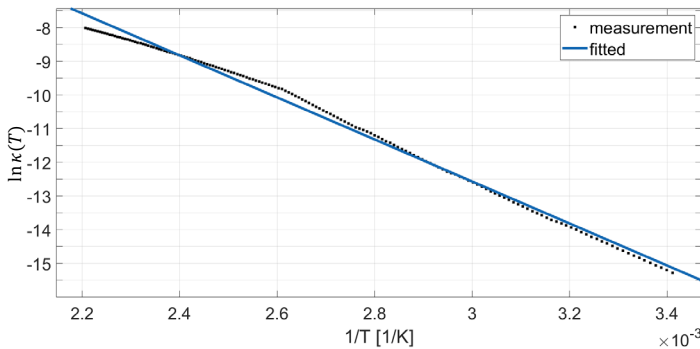


Figure 5.8: Arrhenius plot for the alkaline hydrolysis of PET

$$\ln\{\kappa\} = -6014 \cdot \frac{1}{T} + 5 \quad (5.8)$$

The slope of the Arrhenius plot corresponds to $-E_a/R$. From Eq. 5.8 results the activation energy E_a from PET to 50 ± 5 kJ/mol and the Arrhenius constant calculated from the intercept to be

$\exp(5) = 148 \pm 40 \text{ L}/(\text{min} \cdot \text{cm}^2)$. These numbers fit well with the one referred in [90].

5.3 Verification and errors

In order to validate the model parameters in section 5.2, three different start reaction mixture from Table 4.1 are experimentally examined.

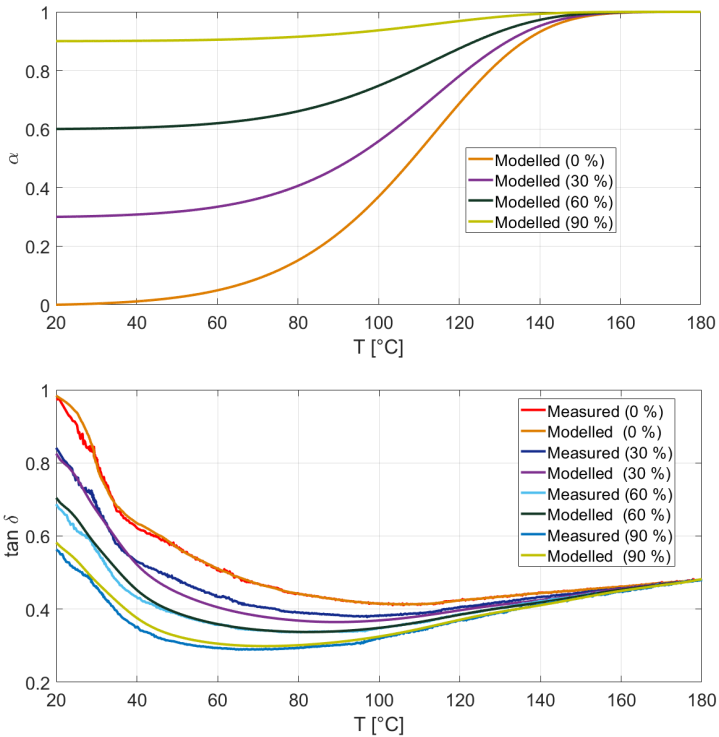


Figure 5.9: Measured and modelled dielectric properties for three different start reaction mixtures from Table 4.1

During the experiment, the heating rate was chosen to be 3 °C/min. At first, the numerical solution of Eq. 5.7 is used to model the course of the reaction. Subsequently, the $\tan \delta$ course is modelled with the help of Fig. 5.6. The corresponding $\tan \delta$ for these three samples are shown in Fig. 5.9. The modeled $\tan \delta$ progress for the different start reaction mixtures are shown in Fig. 5.9.

From Fig. 5.9 a good agreement between the modelled and measured dielectric properties is evident. The most important sources of error are the inaccuracy of the measured dielectric properties, the inaccuracy of the modeled temperature depended dielectric properties of the unreacted mixture, the assumed PET particle thickness and finally the assumption that the losses change only due to the variation of the dissolved NaOH concentration in the liquid solution. The total error on the predicted $\tan \delta$ is estimated to be less than 10 %.

6 Physical and technical design of an industrial μ Wave applicator

6.1 Concept

The applicator has to meet the following specifications:

- It must enable a continuous operation with the use of a metallic Archimedean screw within a tube, which must be transparent to microwaves, e.g. glass.
- It has to provide a homogeneous electric field distribution in axial and azimuth direction of the processed material.
- It has to provide a production rate for the depolymerization of PET of at least 12.5 kg/h and accordingly an overall flow rate of at least 100 kg/h in total for PET, MEG, NaOH and H₂O.

6.2 Archimedean screw geometry

For the microwave assisted depolymerization process, PET and appropriate catalysts have to be transported through the microwave field. This is achieved by the use of a metallic Archimedean screw placed in a microwave transparent glass tube. To make sure that the metallic structure of the Archimedean screw allows an efficient penetration of the electromagnetic field into the liquid, the influence of the Archimedean screw design on the microwave power absorption has been investigated. For optimization the following geometric parameters of the screw were varied: the pitch distance d_s and the thread depth h_s . To simplify the discretization with an orthogonal grid and to reduce the simulation efforts the screw has been modelled by a metallic core and parallel discs with a distance d_s . The simplified screw model is shown in Fig. 6.1.

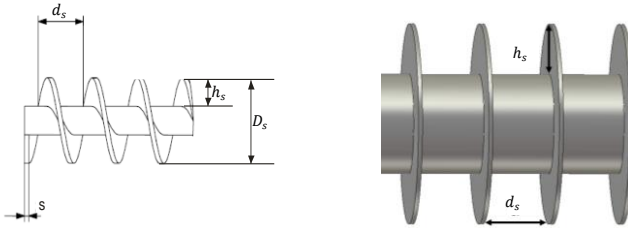


Figure 6.1: Archimedean screw (left) and its simplified model for the simulations (right) [95]

It is assumed that the screw parameters have a comparable influence on the total power efficiency, independent of the exact cavity geometry. For this investigation a rectangular cavity, similar to that of a household microwave oven (310 mm x 375 mm x 200 mm) is used. It is expected that a variation of the screw core diameter should have insignificant impact and, therefore, it is set equal to 100 mm for the further investigations. In the electromagnetic simulation, the screw material is consisted as a perfect electric conductor (PEC) and the dielectric constant ϵ'_r of the surrounding liquid has been chosen equal to 30, because this value corresponds to the order of magnitude of permittivity of the later processed reaction mixture in cold state. The corresponding wavelength λ at the magnetron frequency of 2.46 GHz inside the material is equal to 22.3 mm. The depth of the thread h_s as well as the pitch d_s were varied between $\lambda/4$ and λ in order to study both the resonant and non-resonant behavior. Note that for a fixed external screw diameter, the material volume depends on the final geometry of the screw.

The estimated absorbed power in the liquid material (given in percentage of the input microwave power) for $\epsilon'_r = 30$ and $\tan \delta = 0.01$ or $\tan \delta = 1$ are shown in Table 6.1 for different d_s and h_s . Both parameters are scaled with the wavelength $\lambda = 22.3$ mm. The absorbed power is integrated over the volume of the material.

Table 6.1 reveals a significant influence of the screw geometry on the efficiency of the applicator. In particular for a material with a small dielectric loss constant ($\tan \delta = 0.01$) the screw depth h_s of $\lambda/4$ and $3\lambda/4$, as well as

an increasing pitch d_s , enables a higher absorbed power. Furthermore, Table 6.1 shows that the geometry parameters of the screw are much more important at lower loss tangents, due to the higher penetration depth of the microwaves. The dielectric loss tangent of the liquid used in the process is in the range of $0.3 < \tan \delta < 1$, and correspondingly the differences in the absorbed power between resonant (grey lines in Table 6.1) and non-resonant screw parameters are no longer obvious and may almost disappear for $\tan \delta = 1$, if the penetration depth D_p is in the range of about 3 mm.

Table 6.1: Simulated relative power absorption for various screw parameters, scaled to λ for a dielectric material with $\epsilon'_r = 30$ and $\tan \delta = 0.01$ and 1 respectively [95]

Dimensions		$P_{\text{abs}} [\%]$	
d_s	h_s	$\tan \delta = 0.01$	$\tan \delta = 1$
$\lambda/4$	$\lambda/4$	11	84
$\lambda/4$	$\lambda/2$	6	84
$\lambda/4$	$3\lambda/4$	24	84
$\lambda/4$	λ	15	84
$\lambda/2$	$\lambda/4$	40	75
$\lambda/2$	$\lambda/2$	20	76
$\lambda/2$	$3\lambda/4$	41	77
$\lambda/2$	λ	40	77
$3\lambda/4$	$\lambda/4$	41	84
$3\lambda/4$	$\lambda/2$	34	82
$3\lambda/4$	$3\lambda/4$	66	82
$3\lambda/4$	λ	72	82
λ	$\lambda/4$	92	86
λ	$\lambda/2$	24	82
λ	$3\lambda/4$	86	83
λ	λ	45	83

It is found that a screw pitch of $d_s = n \cdot \lambda/2$; $n = 1,2,3$ in combination with a depth of the thread of

$$h_s = (2n + 1) \cdot \frac{\lambda}{4}; n = 0,1,2, \dots \quad (6.1)$$

enable the best efficiency. This can be understood from the fact that the tangential component of electric field at a perfect conductive surface is equal to zero and has a maximum at a distance of h_s . The screw acts like a quarter-wave wavelength transmission line, equivalent to a short to open transformation and enables a maximum coupling of the microwave power into the material in-between two neighboring threads.

Figure 6.2 shows the relative absorbed power for different $\tan \delta$ for an optimized and a completely unfavorable screw geometry. It is obvious that the improper selection of the geometrical parameters of the Archimedes screw can lead to a significant reduction of the overall system efficiency. This factor is especially important for $\tan \delta < 0.5$. This optimization is proposed in [95]

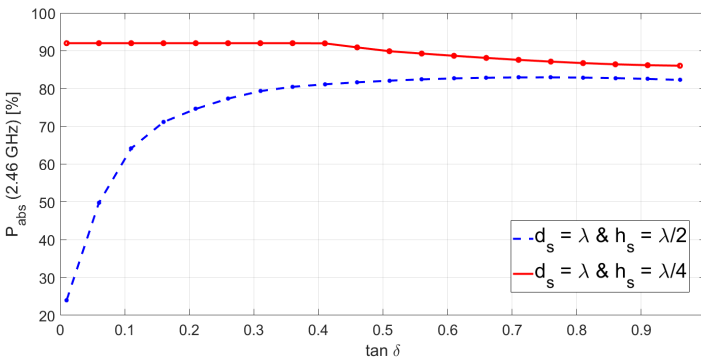


Figure 6.2: Simulated relative power absorption as a function of $\tan \delta$ at 2.46 GHz and $\epsilon_r' = 30$ [95]

6.3 Energy required for a specific volume

The reaction temperature of the depolymerization of PET lies in the range from 150 °C to 220 °C [28]. The specific heat capacity of the reaction mixture $c_{p_{ges}}$ can be estimated as weighted average over the individual reactants as follows

$$c_{p_{ges}} = \frac{m_{PET}c_{p_{PET}} + m_{MEG}c_{p_{MEG}} + m_{NaOH}c_{p_{NaOH}} + m_{H_2O}c_{p_{H_2O}}}{m_{PET} + m_{MEG} + m_{NaOH} + m_{H_2O}} \quad (6.2)$$

The specific heat capacities and the quantities of the individual reactants are shown in Table 6.2.

Table 6.2: Specific heat capacity of the various reactants and the corresponding mass in the used reaction mixture.

Material	c_p [kJ/(kg K)]	mass [g]
PET	1.1 [96]	180
MEG	2.2 [74]	955
H ₂ O	4.2 [74]	140
NaOH	1.49 [97]	82.4

Accordingly, the mentioned reaction mixture provides a specific heat capacity of approximately 2.2 kJ/(kg K). The power P_{heat} required to raise the temperature by ΔT of material with a total mass m within the time Δt can be calculated as follow [98]:

$$P_{heat} = c_{p_{ges}} m \Delta T / \Delta t \quad (6.3)$$

In the application considered here, with a reaction mixture mass of 100 kg and a start temperature of 20 °C, the required power is between 8.0 kW and 12.3 kW depending on the final reaction temperature, without consideration of thermal heat losses.

6.4 Estimation of the applicator segments

The outer diameter of the glass tube is chosen to be 250 mm with a wall thickness of 10 mm. The mentioned glass diameter has been selected according to the maximum dimensions of commercial quartz glass tubes approved for pressure application. The modular concept of the reactor implies a subdivision of the applicator's geometry into N equivalent segments. With the use of this kind of modular concept and the limitations of the glass tube, any specific temperature profile along the reactor may be realized. It requires the control of microwave power level in each segment individually, thus resulting in the corresponding temperature scenario along the material axis (see Fig. 6.3).

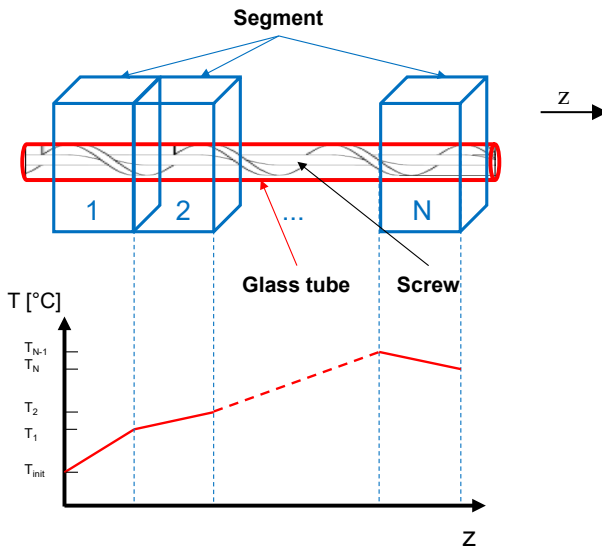


Figure 6.3: Modular design of the microwave reactor (top), temperature profile along the MUT (bottom) [95]

In Fig. 6.3 the temperatures T_1, T_2, \dots, T_N are the target temperatures at the end of each segment. In the particular reaction the reaction mixture should be heated up to the reaction temperature as fast as possible and then the temperature should be kept constant until the reaction is complete. Accordingly, two segments would be sufficient.

Another crucial criterion for the number of segments required, is the size of the available microwave generators (magnetrons) and their prices. As the commercial available magnetrons with more than 3 kW nominal microwave power are equipped with an additional circulator, which is very expensive, only magnetrons with a nominal power from 1 kW, 2 kW and 3 kW are considered. In section 6.3 the power required to bring the reaction mixture to the reaction temperature is estimated between 8 kW and 12 kW. As the magnetrons with a nominal power between 2 kW and 3 kW are the most economical in terms of price per watt. Four segments would be preferred.

Since the process temperature exceeds the boiling point of the aqueous phase of the reactive mixture, a pressurized microwave reactor is required. This reduces the failure probability of the glass tube. Thus, the preferable geometry of the microwave cavity is cylindrical. At the same time, considering the investment and installation efforts, the number of coupling ports with pressure sealed microwave windows and accordingly the number of microwave generators must be reduced to the minimum. Therefore, in the present design only one magnetron and hence one quartz windows per segment is considered.

6.5 Applicator design

In this section, the design of the industrial scale microwave cavity based on the measured material properties is presented. Fig. 6.4 shows the simulated electric field density in a cylindrical cavity with 336 mm in diameter and a length of 250 mm with a single microwave port on the left side. The core of the Archimedean screw occupies the hollow space in the cavity center. The cylindrical sample is enclosed by the glass tube with a diameter of 250 mm. From Fig. 6.4 it can be seen, that the most of the microwave field is absorbed

through the material near the port position and that the electric field shows a strong inhomogeneity in the z-direction as well as in the azimuthal direction.

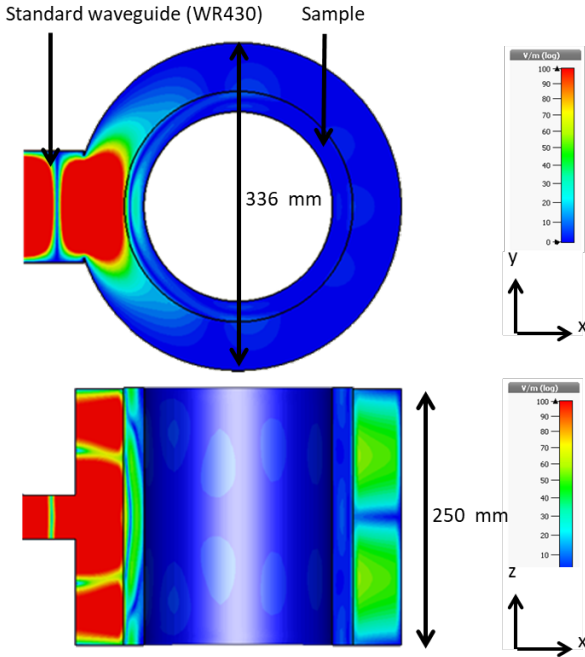


Figure 6.4: Simulated electric field in the cylindrical cavity [95]

The inhomogeneity in the z-direction can be avoided by limiting the cavity length in z-direction to $50 \text{ mm} < \lambda/2$. In this way a constant E-field is forced in z- direction. The dominant mode in that case is a TE_{108} -mode. The corresponding simulation results are shown in Fig. 6.5.

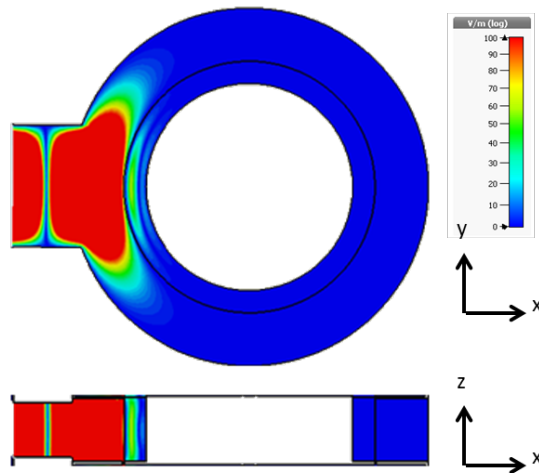


Figure 6.5: Electric field density in a ‘short’ cylindrical microwave cavity with electric length in z-direction $< \lambda/2$ [95]

It should be noted, that in the ‘short’ cavity the azimuthal inhomogeneity of the electric field remains. A further improvement of the field distribution is realized through an optimized power distribution network design. Such an approach enables a well-defined power distribution over the azimuthal direction of the resonator. The optimized distribution network is shown in the Fig.6.6.

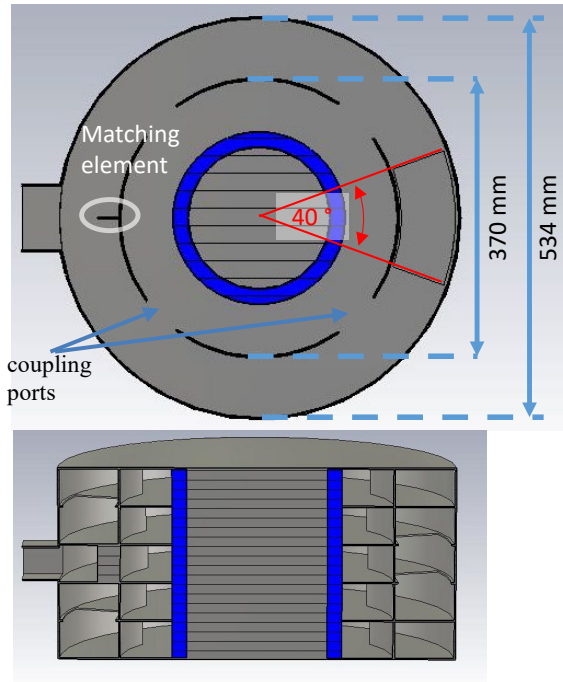


Figure 6.6: Simulated geometry of the power distribution network: center zone (left), side view (right) [95]

This design consists of a single microwave port, which is coupled to the external resonator circuit. The outer diameter of the resonator is 534 mm. The resonator structure has a total effective length of 250 mm and subdivided into 5 zones of equal length (Fig 6.6). Furthermore, looking in the azimuthal direction of each zone four equidistant coupling ports are designed to couple the microwave power to the corresponding heating cavity. It is particularly important that the phase velocity between the actual heating cavity and the external resonator is the same. The number of zones of equal size in a single segment can be varied depending on the required sample length and/or required power density. In that case the coupling apertures between the inner and the outer resonator have to be modified in an appropriate way. The coupling apertures between the different zones should have a width of about λ and are

only depending on the width of the outer resonator. The width and length of this coupling aperture for an outer diameter of the resonator of 534 mm are 72 mm and 157 mm, respectively. In the middle zone this coupling is positioned opposite of the waveguide port (see Fig. 6.6 left). And for the other zones, it is positioned axially symmetrical.

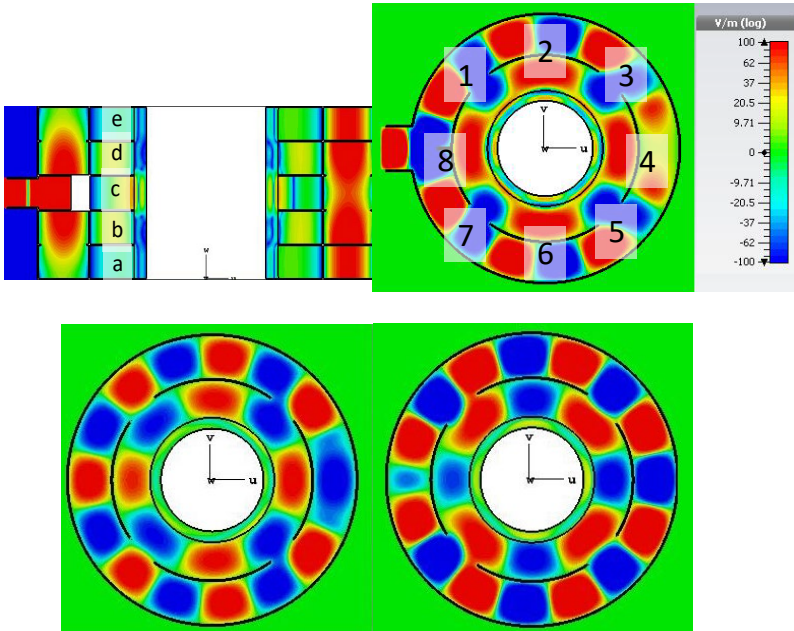


Figure 6.7: Electric field distribution of the power distribution network design in azimuthal direction of zone c (upper right); of levels b and d (lower left); of levels a and e (lower right) and in axial direction (upper left) [95]

Table 6.3 shows the power distribution at the microwave cavity for the five individual segments (a, b, c, d, e). The coordinates of the different radial MUT sections is shown in Fig. 6.7. The listed power is given in percent of the total power absorbed in the applicator.

Table 6.3: Power distribution in the MUT located in the power distribution network [% of the absorbed power] [95]

MUT section (coordinates)	a	b	c	d	e
1	2.5	2.4	2.5	2.4	2.5
2	2.4	2.6	2.5	2.6	2.4
3	2.2	2.8	2.4	2.8	2.2
4	2.3	2.9	2.5	2.9	2.3
5	2.2	2.8	2.4	2.8	2.2
6	2.4	2.6	2.5	2.6	2.4
7	2.5	2.4	2.5	2.4	2.5
8	2.8	2.2	2.7	2.2	2.8

The proposed design shows some similarities with the one presented from [22]. In [22] a so-called ‘Coaxial Wrap-Around TE_{01} Mode Converter’ is introduced. This is based on two coaxially arranged WR90 waveguides that shares a common broad-wall. The design is very similar to the middle segment (segment c) of Fig. 6.7. However, there are a number of key differences with the concept presented here. One of them is the organizing of the coupling between the inner and outer waveguide. In the here proposed design, it is realized via a sidewall of the waveguide contrary to [22] where the coupling is organized through a broadwall. This enables a fully constant electric field in the axial direction. Moreover, the coupling slots between the different cavity segments are tapered to enable a well-defined power distribution. Last but not least the proposed design consists of many ‘stacked’ zones. This enables a constant and defined field distribution over any material length. It is not limited to samples with a length $\leq \lambda/2$.

The proposed design enables a good and well-defined field distribution (see Table 6.3). Since the transition from the waveguide port to the ring-shaped external resonator acts like a waveguide power divider, an additional matching element is needed to achieve a maximum system efficiency. The implemented optimized matching element in the front of the waveguide port (only in the middle zone) is shown in Fig. 6.6. It must be oriented vertically to the port. Already a small misalignment ($<3^\circ$) of this element leads to a significant

change of the power distribution in the middle zone c. The power distribution in adjacent zones is not affected. For example, a rotation clockwise of the matching element from 1° to 3° leads to a difference in the absorbed power between sample section 1 & 7 by factor of 1.5 to 3 respectively. The total absorbed power in the applicator is reduced by 2 %. This matching element leads to significant reduction of the reflected power. The reflected power with and without ‘matching element’ is presented in Fig. 6.8.

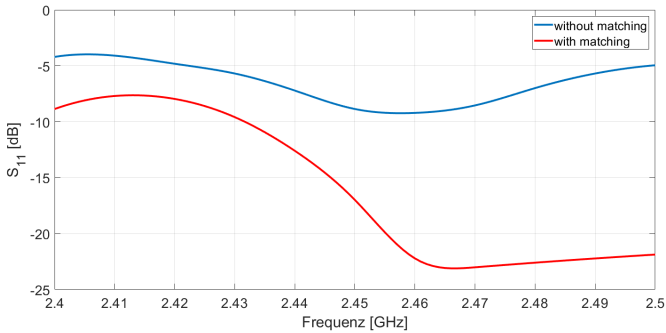


Figure 6.8: Simulated reflected power at the input of the power distribution network with and without matching element versus frequency

Fig. 6.9 shows the total absorbed power versus frequency for different dielectric constants of the material. The design is characterized by a high robustness against material permittivity changes (verified for high loss materials with $\tan \delta > 0.3$). This can be explained by the fact that the resonance frequency of the complete resonator is given by the external power distribution network. In the actual heating cavity is existed a running wave.

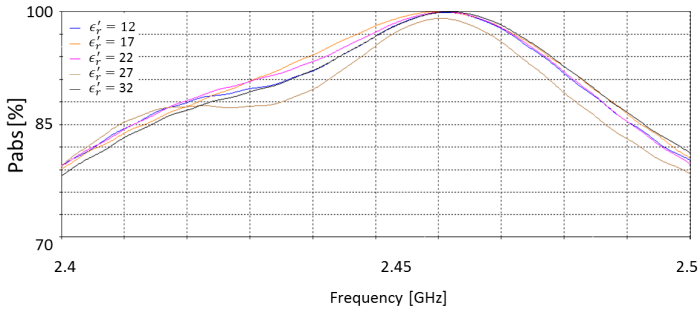


Figure 6.9: Absorbed power for different ϵ_r and $\tan \delta = 0.5$ versus frequency

To avoid a physical electric contact between the cylindrical metal plates (levels separators) and the outer metal tube, a $\lambda/4 = 47$ mm stub filter may be used. This filter makes a virtual open -to -short transformation. Here the gap between filter and metal tube is < 2 mm.

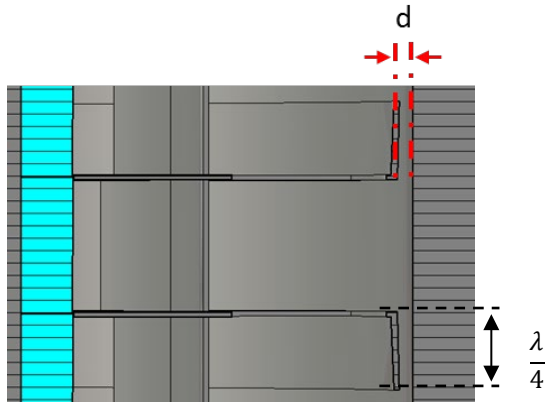


Figure 6.10: $\lambda/4$ filter structure to enable a contactless operati...

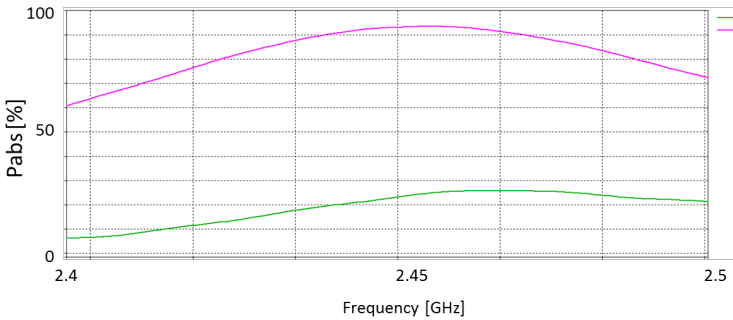


Figure 6.11: Absorbed power versus frequency for different gap thicknesses of the $\lambda/4$ filter structure

At larger distance between inner structure and outer metal tube, the operating mode is strongly suppressed and the matching between the source and the load is lost. This results in a significant loss of system efficiency as shown in the following figure for a 2 and 4 mm gap, respectively. As an alternative contact springs may be used although those are not specified for such high-power applications [99]. Depending on the spring geometry contact gaps in the range from 0.14 mm to 0.7 mm could be bridged.

6.6 Performance of the fabricated applicator

6.6.1 Test set

The design presented in section 6.5 is based on a complex geometry, which consist of several thin sheets of metal that need good electrical contact with each other. Because of the complexity of the geometry, a prototype is very costly to manufacture. A prototype production based on 3d metal printing is out of the question due to the excessive size of the cavity. To enable a cost-efficient manufacturing the design of the prototype has been slightly modified. Modifications at the following elements are done: the wall thicknesses and radius of the edges. For testing purposes, a carbon blended

silicone rubber from Gummiwerk Kraiburg GmbH & Co. KG [100] is chosen. The thermal conductivity of the chosen MUT is low to prove the field homogeneity. A hollow cylindrical sample with 183 mm outer diameter and 171 mm inner diameter and dielectric parameters of $\epsilon' = 15$, $\tan \delta = 0.3$ is chosen. The MUT consists of several stacked cylinders (layers) with tiny vertical cuts. Hence, it forms a sandwich structure. With the vacuum bag the MUT is fixed on the metal core (sample holder, see photo on the Fig. 6.12). To check the homogeneity of the absorbed microwave power in the load, the surface temperature of the sample is recorded with an infrared camera. Firstly, the sample is exposed to the microwave inside the designed applicator. In the following step, it is removed from the applicator and a thermal imaging is recorded. For the experimental verification a magnetron with an output power of 800 Watt and the infrared camera FLIR type AX5 are used. Sample pictures of the manufactured microwave cavity are shown in Fig. 6.12.

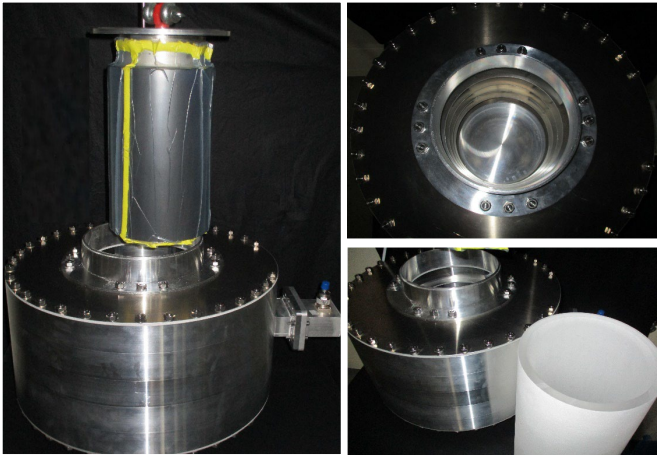


Figure 6.12: Fabricated microwave cavity [95].

6.6.2 Results

For the verification of the developed applicator, the final CAD file from the manufactured applicator is simulated with CST MWS. The comparison with the measurement is shown in Fig. 6.13. From Fig. 6.13 is obvious that the resonance of the developed applicator match very good to the simulation

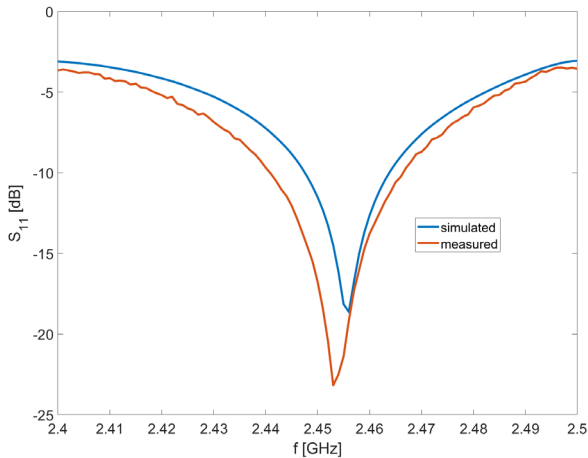


Figure 6.13: Simulated and measured S-parameters

Fig. 6.14 compares the measured temperature distribution, against the simulated absorbed microwave power distribution within the sample. The measured temperature inhomogeneity is found to be $\pm 8^\circ\text{C}$ at a mean temperature level of 90°C (see Fig. 6.14). A proper agreement between simulation and experiment exists. It must be noted, that in the experiment the sample does not completely fill the glass tube inside the applicator. It enables a fast temperature measurement but results in some differences with the simulated absorbed power profile.

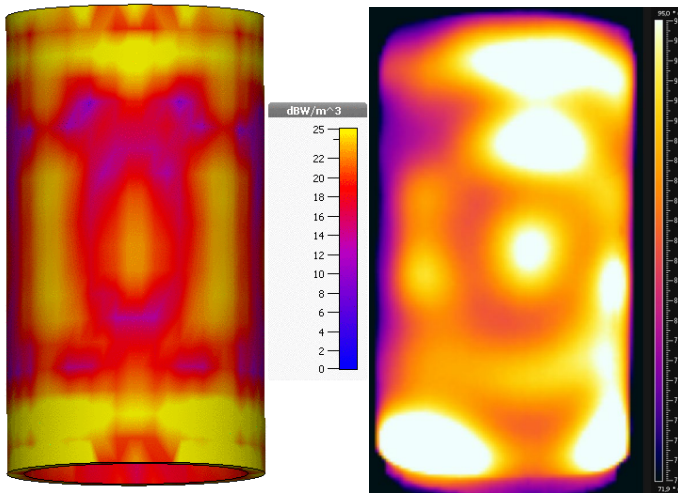


Figure 6.14: Simulated power distribution (left), measured temperature distribution (right) [95]

6.7 Process optimization

The goal is to find the optimum power level of the power sources individually for each segment to get a full-reacted mixture at the end of the applicator. Based on the simulated power distribution in a single segment (see Table 6.3), the demanding temperature profile of the sample passing the microwave cavity is estimated for a four-segment configuration with a total length of one meter. The capacity of the proposed reactor is fixed to about 100 kg/h. Accordingly, the Archimedean screw angular and axial speed is 0.067 rotations per second and 2 mm per second. For the optimization, it is assumed that the thermal convective losses of the mixture remain homogeneous in each zone. This assumption is feasible because the applicator consist of a total of 20 zones (four segments with five zones each). The MUT is heated over its entire length by a $\Delta T < 180$ °C. Hence, it is expected a temperature deviation of about ± 4.5 °C within a zone.

As magnetrons are considered as power sources. The following levels of nominal power are industrially available: 1, 2, 3, 6 and 10 kW. Ideally, the

maximum power of the respective power source is used. The optimization bases on the reactions kinetics developed in section 5 and results in a demanded power of 6 kW in the first segment, 2 kW in the second segment and 1 kW in the third and fourth segment. The convection losses through the glass tube over the entire applicator can be determined using Eq. 3.9. And for this temperature scenario, they amount to approx. 660 W in total.

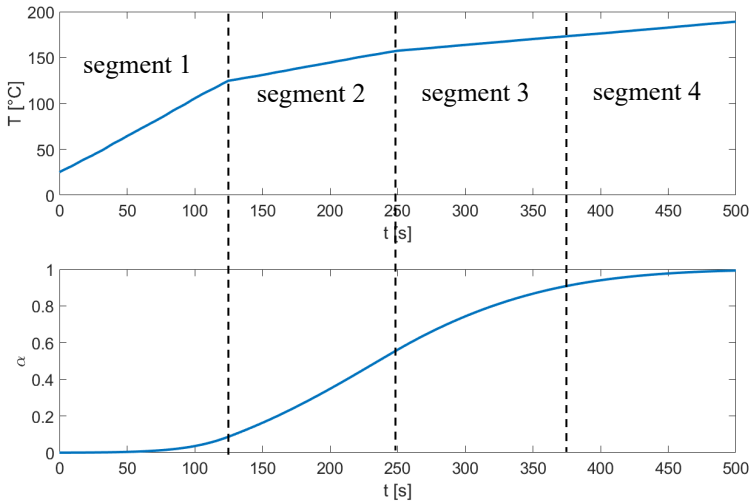


Figure 6.15: Temperature profile and reaction progress across the applicator at a reaction temperature of ≤ 180 °C

In the above scenario, the reaction temperature is limited to 180 °C. Under this assumption, the minimum reaction time is around 5 minutes and 30 seconds, excluded any heating up time. Therefore, a further increase of the installed power does not follow to significantly higher yields. Since the reaction may take place at temperatures up to 220 °C, it is theoretical feasible to double the screw speed and accordingly the reactor capacity by increasing the installed power levels of 10 kW in the first and second segment, 3 kW in the third segment and 0.3 kW in the fourth segment. This scenario follows to very

critical reaction pressure conditions. The corresponding reaction profile is shown in the following figure.

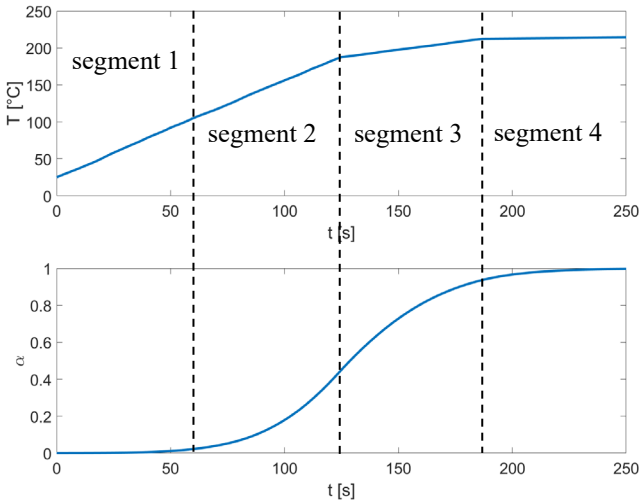


Figure 6.16: Temperature profile and reaction progress across the applicator at temperatures ≤ 220 °C

7 Conclusion and outlook

Polyethylene terephthalate, PET, is a widely used plastic. It shows excellent thermal and mechanical properties and chemical resistance. On the one hand, this robustness of PET is desirable, but on the other hand it is also detrimental for the environment if it is disposed of after use. This makes PET recycling indispensable. PET recycling can be achieved by mechanical processing, chemical recycling and energy recovery. Through chemical recycling, the molecules that originally make up the polymer (PET) can be completely recovered without degradation. This technique is not widely used due to the long reaction time and the high-energy demand. The microwave-assisted depolymerization of PET is expected to take place in significantly shorter reaction times and under milder reaction conditions (e.g. pressure and temperature) [12]. This is probably because in case of microwave-assisted depolymerization, apart from a temperature effect, the microwaves also initiate currents in the material, which leads to a higher mobility of the Na^+ ions.

In this thesis, an innovative microwave applicator for PET recycling is developed with the aim to build an efficient, large-scale process that allows continuous operation. The development is carried out for the Industrial, Scientific and Medical (ISM) frequency band at 2.45 GHz.

The starting point for the successful development of the microwave applicator is the knowledge of the dielectric properties of the materials involved at the process frequency and temperatures. Therefore, an advanced, fully automated system for accurate in-situ monitoring of dielectric properties during microwave heating has been developed. A dual-mode approach is combined with a 3D full-wave simulation. The system allows measurements in wide ranges of the dielectric constant $1.5 < \epsilon_r' < 80$ and loss tangent $0.01 < \tan \delta < 1$. The coupling design allows an isolation of about 60 dB between both operating modes, thus the interference can be neglected. Furthermore, the sample holder is sealed at both ends with connectors that withstand a pressure of 18 bar. This allows the dielectric characterization of liquids above the boiling point.

The measurement of the time- and temperature-dependent dielectric loss tangent enables the determination of the actual reaction course. Based on these data a model for the reaction kinetics is developed. The model allows an optimization of the process parameters, such as heating time and temperature holding time. This model also allows the definition of the power requirement per reaction segment to enable a targeted material throughout under consideration of the convection losses across the glass tube.

Accurate power measurements enable a qualitative calorimetric estimation of the PET depolymerization process. Based on RF and multi-physics modeling of the experimental setup, the specific heat capacity of well-known liquids is determined based on a microwave calorimeter for the first time.

An advanced microwave cavity on an industrial scale, which enables power efficient microwave heating of liquids with high permittivity at 2.45 GHz, has been developed. The developed applicator is modular and allows homogeneous heating of a large cylindrical sample with an outer diameter of 250 mm. The sample volume used in the simulation is 11 liter. The use of a coupled resonator structure allows a specific power distribution in the cavity. In addition, a matching element at the port position leads to a significantly increased power efficiency.

The reached power efficiency is $> 95 \%$ for high permittivity materials in the range from $15 < \epsilon'_r < 25$ and $\tan \delta > 0.3$. The maximum temperature deviation is estimated to be below $4 \text{ }^\circ\text{C}$ for a sample volume of 11 liter.

Due to its modular design the applicator can easily be adapted to the requirements of different reaction conditions and different reactants. The first experiment shows a very promising homogeneity of the absorbed RF power ($\pm 8 \text{ }^\circ\text{C}$). The temperature distribution corresponds well to the expectations from the simulation for the MUT geometry used. The continuous operation of the applicator is realized with an Archimedean screw, which transports the displacement through the microwave pattern. The screw geometry was investigated and optimized independently of the final design of the applicator. It is shown that the screw geometry becomes especially important for materials with $\tan \delta < 0.3$.

Based on the work done in this thesis, the calorimetric measurements setup could be further optimized in order to improve the power measurements accuracy. For example, a more stable bidirectional coupler and or improved manufactured cavity, which allows a more precise definition of the wall losses, would significantly improve the accuracy of the calculated absorbed power. Furthermore, a faster temperature sensor would allow faster heating ramps and more accurate temperature control.

Regarding the industrial scale applicator, even lower frequencies, such as 915 MHz, would be interesting. This enables higher penetration depth of the microwaves into the reaction mixture and subsequently allows the core of the Archimedean screw to be reduced. In this way, a significant increase of the applicator capacity tube may be reached by use of the same glass tube diameter.

In the frame of the European Union's Horizon 2020-SPIRE-2015 research and innovation program SYMBIOPTIMA in cooperation with the industry, a microwave applicator similar to the one presented in this thesis was also developed and is successfully installed at one of the industry partners. They have shown its efficiency and the simulations match very well. Based on the results of this applicator, one of the project partners won the 2018 Innovation Radar Prize [101]

8 Appendix

Frequency and temperature dependent dielectric properties of MEG and NaOH

Fig 8.1 shows the measured dielectric parameters of MEG for three different temperatures. It can be seen that the dielectric constant ϵ_r' of MEG increases with the temperature and the dielectric losses decreases (see Fig 8.1).

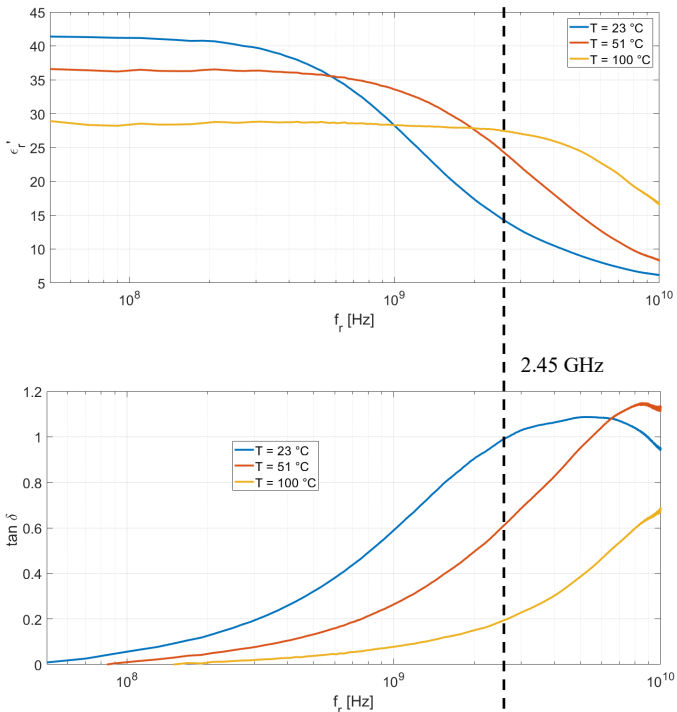


Figure 8.1: Measured dielectric properties of MEG using the coaxial probe HP 85070B at three different temperatures in a wide frequency range

The Debye model can describe the behavior of the measured permittivity from Fig 8.1. Using the Debye model, the frequency dependent permittivity can be determined as follows [102]

$$\epsilon' = \epsilon_{\infty} + \frac{\epsilon_s - \epsilon_{\infty}}{(1 + j\omega\tau)^2} \quad (8.1)$$

$$\epsilon'' = \frac{\omega\tau(\epsilon_s - \epsilon_{\infty})}{(1 + j\omega\tau)^2} \quad (8.2)$$

where ϵ_{∞} corresponds to the permittivity of the medium at very high frequencies, ϵ_s the low-frequency permittivity of the medium and τ the characteristic relaxation time of the medium. τ is connected with the temperature as follows:

$$\tau = \tau_{\infty} \exp\left(\frac{E_{\alpha}}{k_B T}\right) \quad (8.3)$$

where τ_{∞} is the relaxation constant, E_{α} is the activation energy and k_B is the Boltzmann constant. For $\tau = \omega^{-1}$ the course of ϵ' follows a step from ϵ_s to ϵ_{∞} and ϵ'' runs through a maximum at the same frequency. From eq. 8.3, it is clear that an increase in T results in a shift of the frequency dependent permittivity to higher frequencies (to the right). This behavior follows the curves measured here (see Fig 8.1).

Fig 8.2 shows the measured dielectric properties of a 5 wt.% NaOH solution in water. It can be seen that the dielectric losses increases with the temperature. It should be noted that the losses in the mixture are mainly dominated by the conductivity losses, which normally increases exponentially with temperature.

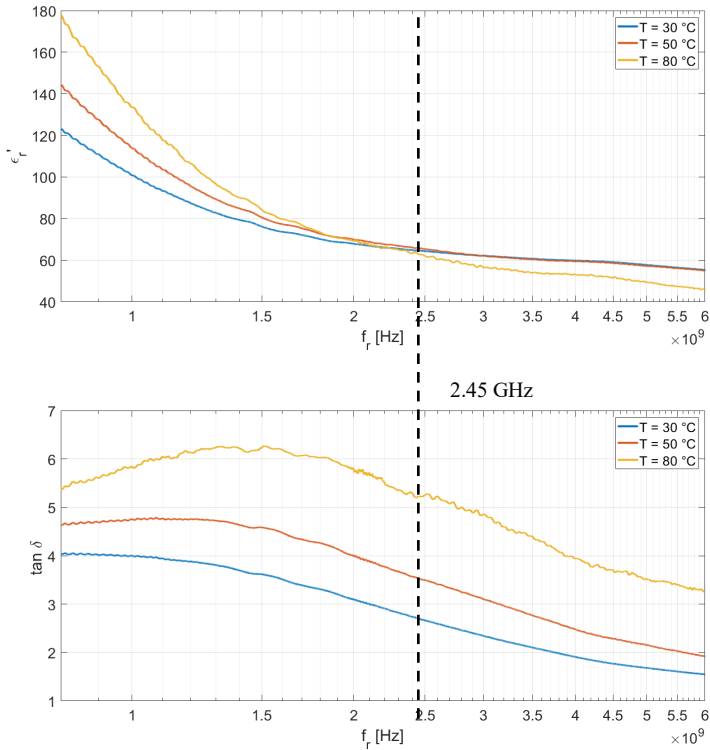


Figure 8.2: Measured dielectric properties of 5 wt.% NaOH with H₂O mixture using the coaxial probe HP 85070B at three different temperatures in a wide frequency range

Modelling of the reaction kinetic

A usage of the curve-fitting tool from MatLab ‘cftool’ shows that the behavior of the unreacted reaction mixture over the temperature can be approximated by a Gaussian function with five terms. The expected error on the loss factor due the fitting is estimated to about 0.11 %.

$$\tan \delta_{Start}(T) = \sum_{x=1}^5 a_x e^{-\left(\frac{T-b_x}{c_x}\right)^2} \quad (8.4)$$

Table 8.1: Course of the coefficients and their approximation from the unreacted reaction mixture

x	a_x	b_x	c_x
1	0.1980	15.1481	2.7032
2	0.3301	14.1132	16.1049
3	0.1642	40.8480	30.7718
4	0.0227	75.7096	13.8588
5	0.6254	141.1441	430.6950

$$\tan \delta_{End}(T) = \sum_{x=1}^5 a_x e^{-\left(\frac{T-b_x}{c_x}\right)^2} \quad (8.5)$$

The course of the coefficients and their approximation for the reaction product are given in Table 8.2 and from the reaction mixture during the reaction in Table 8.3. The expected errors through this fitting for the reaction product and the reaction mixture are estimated to be about 0.18 % and 0.1 % correspondingly.

Table 8.2: Course of the coefficients and their approximation from the reaction product.

x	a_x	b_x	c_x
1	0.0475	27.6109	7.4211
2	0.3781	207.5609	106.1568
3	0.0109	123.8985	13.4328
4	6129.5	-325.851	109.2479
5	0.6894	-637.99	633.3769

Table 8.3: Course of the coefficients and their approximation from the loss factor during the reaction.

x	a_x	b_x	c_x
1	41.4544	-30.5646	21.5679
2	0.1496	26.3432	6.8576
3	0.6486	-4.5765	67.3126
4	0.0153	183.9751	14.9851
5	0.4651	178.0238	152.0581

The fitting of the time depending loss factor during the reaction is realized also with the help of a Gaussian function with 8 terms. The expected error through the fitting is 0.15 %

$$\tan\delta_{\text{Reaction}}(t) = \sum_{x=1}^8 a_x e^{-\left(\frac{t-b_x}{c_x}\right)^2} \quad (8.6)$$

Table 8.4: Course of the coefficients and their approximation from the time depending loss factor of the reaction mixture.

x	ax	bx	cx
1	3.798e11	-4289.3	825.3049
2	0.3269	196.8953	159.6712
3	0.2332	400.6403	129.1403
4	0.0906	621.5689	256.4009
5	0.4440	3492.2	1046.7
6	0.4824	752.6186	1623.7
7	0.0236	2710.1	419.3913
8	0.1099	2258.3	606.1110

Bibliography

- [1] B. Geyer, G. Lorenz and A. Kandelbauer, "Recycling of poly(ethylene terephthalate) – A review focusing on chemical methods," *eXPRESS Polymer Letters*, vol. 10, no. 7, pp. 559-586, 2016, doi: 10.3144/expresspolymlett.2016.53.
- [2] R. Schiffman, "State of the art of microwave applications in the food industry in the USA," in *Advances in Microwave and Radio Frequency Processing*, Berlin, Springer-Verlag, 2006, ISBN-10: 3-540-43252-3, pp. 415-425.
- [3] T. Kayser, G. Link, T. Seitz, V. Nuß, J. Dittrich, J. Jelonnek and R. Ghomeshi, "An applicator for microwave assisted pultrusion of carbon fiber reinforced plastic," 2014 IEEE MTT-S International Microwave Symposium (IMS2014), pp. 1-4, 10 July 2014, doi: 10.1109/MWSYM.2014.6848325.
- [4] M. Mehdizadeh, "Engineering and scale-up considerations for microwave induced reactions," *Research on Chemical Intermediates*, vol. 20, no. 1, pp. 79-84, 25 August 1993, doi: 10.1163/156856794X00081.
- [5] J. Qinhan, L. Feng, Z. Hanqi, Z. Liwei, H. Yanfu and S. Daqian, "Applications of microwave techniques in analytical chemistry," *TrAC Trends in Analytical Chemistry*, vol. 18, no. 7, pp. 479-484, July 1999, doi: 10.1016/S0165-9936(99)00110-7.
- [6] M. Gupta, S. Paul and R. Gupta, "General characteristics and applications of microwaves in organic synthesis," *Acta Chim Slov*, vol. 56, pp. 749-764, 2009.
- [7] P. L. Jones and A. T. Rowley, "Dielectric Drying," vol. 14, no. 5, pp. 1063-1098, 07 May 2007, doi: <https://doi.org/10.1080/07373939608917140>.
- [8] A. de la Hoz, Á. Díaz-Ortiz and A. Moreno, "Microwaves in organic synthesis. Thermal and non-thermal microwave effects," *The Royal Society of Chemistry*, vol. 34, pp. 164-178, 2005, doi: 10.1039/B411438H.

- [9] R. Geyer, J. R. Jambeck und K. L. Law, „Production, use, and fate of all plastics ever made,“ *Science Advances*, Bd. 3, Nr. 7, pp. 1-5, 2017, doi: 10.1126/sciadv.1700782.
- [10] V. Sinha, M. R. Patel and J. V. Patel, “PET Waste Management by Chemical Recycling: A Review,” *J Polym Environ*, vol. 18, pp. 8-25, 3 September 2008, doi: 10.1007/s10924-008-0106-7.
- [11] J. Hopewell, R. Dvorak and E. Kosior, “Plastics recycling: challenges and opportunities,” *Philos Trans R Soc Lond B Biol Sci.*, vol. 364, no. 1526, pp. 2115-2126, 27 July 2009, doi: 10.1098/rstb.2008.0311.
- [12] D. S. Achilias, H. H. Redhwi, M. N. Siddiqui, A. K. Nikolaidis, D. N. Bikiaris and G. P. Karayannidis, “Glycolytic Depolymerization of PET Waste in a Microwave Reactor,” *JOURNAL OF Applied Polymer SCIENCE*, vol. 118, no. 5, pp. 3066-3073, 03 September 2010, doi: 10.1002/app.32737.
- [13] M. Khoonkari, A. H. Haghighi, Y. Sefidbakht, K. Shekoohi and A. Ghaderian, “Chemical Recycling of PET Wastes with Different Catalysts,” *International Journal of Polymer Science*, vol. 2015, 16 September 2015, doi: 10.1155/2015/124524.
- [14] A. Davis, “theinstitute.ieee.org,” 2 Mai 2016. [Online]. Available: <http://theinstitute.ieee.org/tech-history/technology-history/a-history-of-the-microwave-oven>. [Accessed 10 August 2020].
- [15] A. W. Hull, “The magnetron,” *Journal of the American Institute of Electrical Engineers*, vol. 40, no. 9, pp. 715-723, 9 Sept. 1921, doi: 10.1109/JoAIEE.1921.6594005.
- [16] IMS, “Industrial Microwave Systems, L.L.C.,” 2003. [Online]. Available: <http://www.industrialmicrowave.com/> [Accessed 05 April 2019].
- [17] M. Mehdizadeh, *Microwave/RF Applicators and Probes*, Great Britain: William Andrew, 2015, ISBN: 9780323322560.
- [18] C. O. Kappe, “My Twenty Years in Microwave Chemistry: From Kitchen Ovens to Microwaves that aren’t Microwaves,” *The chemical record*, vol. 19, no. 1, pp. 15-39, 15 June 2018, doi: 10.1002/tcr.201800045.

- [19] Ferrite Microwave Technologies, 2019. [Online]. Available: <https://ferriteinc.com/industrial-microwave-systems/>. [Accessed 14 Dez. 2019].
- [20] L. Feher and M. Thumm, "Microwave innovation for industrial composite fabrication-the HEPHAISTOS technology," *IEEE Transactions on Plasma Science*, vol. 1, pp. 73-79, 04 May 2004, doi: 10.1109/TPS.2004.823983.
- [21] L. Feher, "Simulationsrechnungen zur verfahrenstechnischen Anwendung von Millimeterwellen für die industrielle Materialprozeßtechnik," *FZKA 5885*, Karlsruhe, 1997, doi: 10.5445/IR/270041647.
- [22] C. D. Nantista, "Overmoded Waveguide Components for High-Power RF," *SLAC-PUB-10218*, vol. 691, no. 1, pp. 263-271, 01 December 2003, doi: 10.1063/1.1635127.
- [23] I. Imenokhoyev and P. Wübber, "Microwave Heating - practical examples," *Microwave Heating Reports*, pp. 69-72, March 2013.
- [24] Fricke und Mallah Microwave Technology GmbH, [Online]. Available: <https://www.microwaveheating.net/de/anlagentechnik/durchlaufanlagen>. [Accessed 26 August 2020].
- [25] J. Varith, C. Noochuay, P. Netsawang, B. Hirunstitporn, S. Janin and M. Krairiksh, "Design of Multimode-Circular Microwave Cavity for Agri-Food Processing," *2007 Asia-Pacific Microwave Conference*, pp. 1-4, 27 June 2008, doi: 10.1109/APMC.2007.4554804.
- [26] M. Nikje and F. Nazari, "Microwave-assisted depolymerization of poly(ethylene terephthalate) [PET] at atmospheric pressure.," *Advances in Polymer Technology* 25, vol. 25, no. 4, pp. 242-246, 5 July 2006, doi: 10.1002/adv.20080.
- [27] M. A. Anaqbi, M. A. Mohsin, R. M. Busheer and Y. Haik, "Microwave assisted glycolysis of poly(ethylene terephthalate) catalyzed by 1-butyl-3-methylimidazolium bromide ionic liquid," *Journal of Applied Polymer Science*, vol. 132, no. 12, pp. 41666 (1-7), 14 November 2014, doi: 10.1002/app.41666.
- [28] M. N. Siddiqui, D. S. Achilias, H. H. Redhwi, D. N. Bikiaris, K. K.-A. G. and G. P. Karayannidis, "Hydrolytic depolymerization of PET in a microwave reactor.," *Macromolecular Materials and Engineering*, vol.

- 295, no. 6, pp. 575-584, 15 June 2010, doi: 10.1002/mame.201000050.
- [29] C. Corporation, "CEM," [Online]. Available: <https://cem.com/en/discover-sp>. [Accessed 03 June 2020].
- [30] Y. Takahashi, "Continuous denitration apparatus". United States Patent US5589140A, 31 December 1996.
- [31] M. Lataillade, "Devices for treating human or animal dejections by means of microwaves". United States Patent US5145576A, 08 September 1992.
- [32] Keysight Technologies, Inc., Application Note: Basics of Measuring the Dielectric Properties of Materials, Keysight Technologies, 2017.
- [33] L. Chen, C. Ong, C. Neo, V. Varadan and V. Varadan, *Microwave Electronics: Measurement and Material Characterisation*, England: J. Wiley & Sons, 2004, ISBN: 978-0-470-84492-2.
- [34] Y. H. Hui, *Handbook of food science, technology, and engineering*, USA: Taylor & Francis Group, LLC, 2006, ISBN-13: 978-0849398476 .
- [35] A. Sihvola, "Mixing rules with complex dielectric coefficients.," *Subsurface Sensing Technologies and Applications*, vol. 1, no. 4, pp. 393-415, 2000, doi: 10.1023/A:1026511515005.
- [36] A. V. Goncharenko, V. Z. Lozovski and E. Venger, "Lichteneker's equation: applicability and limitations.," *Optic Communication*, vol. 174, no. 1-4, pp. 19-32, 2000, doi: 10.1016/S0030-4018(99)00695-1.
- [37] A. Nesbitt, P. Navabpour, B. Degamber, C. Nightingale, T. Mann, G. Frnado and R. J. Day, "Development of a microwave calorimeter for simultaneous thermal analysis, infrared spectroscopy and dielectric measurements," *Measurement Science and Technology*, vol. 15, no. 11, pp. 2313-2325, 2004, doi: 10.1088/0957-0233/15/11/018.
- [38] S. Soldatov, T. Kayser, G. Link and J. Jelonnek, "Microwave cavity perturbation technique for high-temperature dielectric measurements," *2013 IEEE MTT-S International Microwave Symposium Digest (MTT)*, pp. 1-4, 06 January 2014, doi: 10.1109/MWSYM.2013.6697793.

-
- [39] J. Baker-Javis, *Transmission/reflection and Short Circuit Line Permittivity Measurements*, USA: NIST Technical Note, 1990.
- [40] E. Kılıç, U. Siart, O. Wiedenmann, U. Faz, R. Ramakrishnan, P. Saal and T. F. Eibert, "Cavity Resonator Measurement of Dielectric Materials Accounting for Wall Losses and a Filling Hole," *IEEE Transactions on Instrumentation and Measurement*, vol. 62, no. 2, pp. 401-407, 2013, doi: 10.1109/TIM.2012.2215072.
- [41] M. D. Janezic and J. Baker-Jarvis, "Full-Wave Analysis of a Split-Cylinder Resonator for Nondestructive Permittivity Measurements," *IEEE Transactions on Microwave Theory and Techniques*, vol. 47, no. 10, pp. 2014-2020, 1999, doi: 10.1109/22.795077.
- [42] K. H. Breeden and J. B. Langley, "Fabry-Perot Cavity for Dielectric Measurements," *THE REVIEW OF SCIENTIFIC INSTRUMENTS*, vol. 40, no. 9, pp. 1162-1163, 1969, doi: 10.1063/1.1684188.
- [43] R. Collin, *Field Theory of Guided Waves*, Wiley-IEEE Press, 1991, ISBN: 9780470544648.
- [44] D. M. Pozar, *Microwave Engineering*, United States of America: John Wiley & Sons, Inc., 2011, ISBN: 978-0-470-63155-3.
- [45] T. Zwick, *Hochfrequenztechnik*, Institute of Radio Frequency Engineering and Electronics, KIT Karlsruhe, 2008.
- [46] A. M. Nicolson and G. F. Ross, "Measurement of the Intrinsic Properties of Materials by Time-Domain Techniques," *IEEE TRANSACTIONS ON INSTRUMENTATION AND MEASUREMENT*, vol. 19, no. 4, pp. 377-382, 1970, doi: 10.1109/TIM.1970.4313932.
- [47] S. S. Stuchly and M. Matuszewski, "A combined total reflection-transmission method in application to dielectric spectroscopy," *IEEE Transactions on Instrumentation and Measurement*, vol. 27, no. 3, pp. 285-288, 1978, doi: 10.1109/TIM.1978.4314682.
- [48] J. M. Catala-Civera, A. J. Canos, F. L. Penaranda-Foix and E. R. Davo, "Accurate determination of the complex permittivity of materials with transmission reflection measurements in partially filled rectangular waveguides.," *IEEE Transactions on Microwave Theory and Techniques*, vol. 51, no. 1, pp. 16-24, 2003, doi: 10.1109/TMTT.2002.806940.

- [49] U. C. Hasar, "Accurate complex permittivity inversion from measurements of a sample partially filling a waveguide aperture.," *IEEE Transactions on Microwave Theory and Techniques*, vol. 58, no. 2, pp. 451-457, 2010, doi: 10.1109/TMTT.2009.2038444.
- [50] M. J. Akhtar and M. Thumm, "Measurement of Complex Permittivity of Cylindrical Objects in the E-Plane of a Rectangular Waveguide," *IEEE Transactions on Geoscience and Remote Sensing*, vol. 51, no. 1, pp. 122-131, 2015, doi: 10.1109/TGRS.2012.2201259.
- [51] J. Krupka and C. Weil, "Recent advances in metrology for the electromagnetic characterization of material at microwave frequency.," 12th International Conference on Microwaves and Radar. MIKON-98. Conference Proceedings (IEEE Cat. No.98EX195), vol. 4, pp. 243-253, 20-22 May 1998, doi: 10.1109/MIKON.1998.738473.
- [52] D. Goudere, M. Giroux and R. G. Bosisi, "Dynamic High Temperature Microwave Complex Permittivity Measurements on Samples Heated Via Microwave Absorption," *Journal of Microwave Power*, 8:1, vol. 8, no. 1, pp. 69-82, 1973, doi: 10.1080/00222739.1973.11689019.
- [53] W. Xi and W. R. Tinga, "Microwave heating and characterization of machinable ceramics," *MRS Proceedings*, vol. 269, no. 569, 25 February 1991, doi: 10.1557/PROC-269-569.
- [54] Y. Nikawa and K. Zhao, "Dynamic Measurement of Complex Permittivity in Microwave Material Using Microwave Power," 2011 IEEE MTT-S International Microwave Symposium, pp. 1-4, 5-10 June 2011, doi: 10.1109/MWSYM.2011.5972978.
- [55] J. M. Catala-Civera, P. Plaza-Gonzalez, J. D. Gutierrez, B. Garcia-Banos and F. L. Penarada-Foix, "Dynamic Measurement of Dielectric Properties of Materials at High Temperature During Microwave Heating in a Dual Mode Cylindrical Cavity," *IEEE Transactions on Microwave Theory and Techniques*, vol. 63, no. 9, pp. 2905-2914, 2015, doi: 10.1109/TMTT.2015.2453263.
- [56] D. Spaseska and M. Civkaroska, "Alkaline hydrolysis of poly(ethylene terephthalate) recycled from the postconsumer soft-drink bottles," *Journal of the University of Chemical Technology and Metallurgy*, vol. 45, no. 4, pp. 379-384, 2010.

- [57] S. Mishra and A. S. Goje, "Chemical Recycling, Kinetics, and Thermodynamics of Alkaline Depolymerization of Waste Poly(Ethylene Terephthalate) (PET)," *Polymer Reaction Engineering*, vol. 11, no. 4, pp. 963-987, 2003, doi: 10.1081/PRE-120026382.
- [58] A. S. Goje, S. A. Thakur, V. R. Diware, S. A. Patil, P. S. Dalwale and S. Mishra, "Hydrolytic Depolymerization of Poly (Ethylene Terephthalate) Waste at High Temperature Under Autogenous Pressure," *Polymer-Plastics Technology and Engineering*, vol. 43, no. 4, pp. 1093-1113, 4 September 2004, doi: 10.1081/PPT-200030031.
- [59] G. Höhne, W. F. Hemminger and H. Flammersheim, *Differential Scanning Calorimetry*, Germany: Springer-Verlag, 2003, ISBN: 978-3-662-03302-9.
- [60] E. Freire, O. L. Mayorga and M. Straume, "Isothermal Titration Calorimetry," *American Chemical Society*, pp. 950A-959A, 15 Sept. 1990, doi: 10.1021/ac00217a002.
- [61] I. Wadsö and R. N. Goldberg, "Standards in Isothermal Microcalorimetry," *Pure and Applied Chemistry*, vol. 73, no. 10, pp. 1625-1639, 01 Jan 2009, doi: 10.1351/pac200173101625.
- [62] G. M. B. Parkes, G. Bond, P. A. Barnes and E. L. Charsley, "Development of a new instrument for performing microwave thermal analysis," *Review of Scientific Instruments*, vol. 71, no. 1, pp. 168-175, 28 December 1999, doi: 10.1063/1.1150179.
- [63] L. Zong, N. Zhou, M. C. Hawley and L. C. Kempel, "A Review of Microwave-Assist Polymer Chemistry (MAPC)," *Journal of Microwave Power and Electromagnetic Energy*, vol. 38, no. 1, pp. 49-74, 14 Jun 2016, doi: 10.1080/08327823.2003.11688487.
- [64] V. Ramopoulos, G. Link, S. Soldatov, T. Spira and J. Jelonnek, "Advanced Dual-Mode Resonator for In-Situ Dielectric Measurements of Lossy Materials," In *Proc. 3rd Global Congress on Microwave Energy Applications*, 25-29 July 2016.
- [65] "Alcoa UltrAlloy® 6020-T8 Aluminum," *MatWeb Material Property Data*, [Online]. Available: <http://www.matweb.com/search/datasheet.aspx?matguid=cae92c0029764c1c9df27beea579cacf>. [Accessed 11 Juli 2020].

- [66] E. Kamenetskii, A. Sadreev and A. Miroschnichenko, *Fano Resonances in Optics and Microwave*, Switzerland: Springer, 2018, ISBN: 978-3-319-99731-5.
- [67] L. Wei-Na and W. Jun-Hong, "Effective permittivity of alcohol + water mixtures as influenced by concentration," *Journal of Chemical and Pharmaceutical Research*, vol. 6, no. 7, pp. 1432-1434, 2014, ISSN: 0975-7384 .
- [68] R. Barlow, *Statistics, A guide to the use of statistical methods in the physical sciences*, John Wiley & Sons, 1989, ISBN: 978-0-471-92295-7.
- [69] V. Ramopoulos, G. Link, S. Soldatov and J. Jelonnek, "Development of an Advanced Microwave Calorimeter for Monitoring of Chemical Reactions," In Proc. 51ST Annual Microwave Power Symposium (IMPI 51), 20-22 June 2017.
- [70] "www.ingenieurkurse.de," [Online]. Available: <https://www.ingenieurkurse.de/waermeuebertragung-waermeleitung/waermeleitung-in-einem-feststoff/stationaere-waermeleitung/waermeleitung-durch-eine-zyllindrische-wand.html>. [Accessed 24 01 2020].
- [71] R. Karwa, *Heat and Mass Transfer*, Singapore: Springer, 2020, ISBN: 978-981-10-1557-1.
- [72] M. J. Moran, H. N. Shapiro, D. D. Boettner and M. B. Bailey, *Fundamentals of engineering thermodynamics*, USA: Wiley, 2014, ISBN: 978-1-119-39138-8.
- [73] Heraeus, "Base Materials Heraeus Conamic," March 2020. [Online]. Available: https://www.heraeus.com/media/media/hca/doc_hca/products_and_solutions_8/BaseMaterials_Image_EN.pdf. [Accessed 30 August 2020].
- [74] "Specific Heat Capacity Table," [Online]. Available: http://www2.ucdsb.on.ca/tiss/stretton/database/Specific_Heat_Capacity_Table.html. [Accessed 24 Juli 2020].
- [75] P. S. Express, "https://epos.henkel.com/tm/cat#!," 10 06 2015. [Online]. Available: <https://epos.henkel.com/media/225c242f95e9f73f0019f5ad1516237e/>

- Pattex_Stabilit_Express/tds_pattex_diy_2komponentenkleber_pse13_1160252_de.pdf. [Accessed 9 02 2020].
- [76] C. Corcione, F. Freuli and M. Frigione, "Cold-Curing Structural Epoxy Resins: Analysis of the Curing Reaction as a Function of Curing Time and Thickness," *Materials (Basel)*, vol. 7, no. 9, p. 6832–6842, 22 Sep 2014, doi: 10.3390/ma7096832.
- [77] M. U. Calculator, "www.anritsu.com," 24 04 2008. [Online]. Available: <https://www.anritsu.com/en-US/test-measurement/support/downloads/software/dwl003263>. [Accessed 13 02 2020].
- [78] K. Technologies, "keysight.com," 30 October 2018. [Online]. Available: <http://literature.cdn.keysight.com/litweb/pdf/N5224-90002.pdf>. [Accessed 18 Feb. 2020].
- [79] Ingenieurbüro Dr.-Ing. Georg Kronawitter, "PID-Regelung - Grundlagen & mehr," 01 06 2020. [Online]. Available: <http://www.control-technology.de/ct/pid01.html>. [Accessed 2020 08 22].
- [80] "literature.cdn.keysight.com," April 1993. [Online]. Available: <http://literature.cdn.keysight.com/litweb/pdf/85070-90009.pdf>. [Accessed 2019 06 06].
- [81] H. Packard, HP 85070B Dielectric Probe Kit User Manual, 1997.
- [82] A. Metaxas and R. Meredith, *Industrial Microwave Heating*, vol. 1, United Kingdom: Short Run Press Ltd., Exeter, 1983, ISBN: 0906048893.
- [83] V. Ramopoulos, S. Soldatov, G. Link, T. Kayser, M. Gehringer and J. Jelonnek, "Microwave system for in-situ dielectric and calorimetric measurements in a wide temperature range using a TE111-mode cavity," 2015 IEEE MTT-S International Microwave Symposium, pp. 1-4, 17-22 May 2015, doi: 10.1109/MWSYM.2015.7166906.
- [84] "Eintragung zu Polyethylenterephthalat in der GESTIS-Stoffdatenbank," Institut für Arbeitsschutz der Deutschen Gesetzlichen Unfallversicherung, [Online]. Available: [http://gestis.itrust.de/nxt/gateway.dll/gestis_de/012060.xml?f=templates\\$fn=default.htm\\$3.0](http://gestis.itrust.de/nxt/gateway.dll/gestis_de/012060.xml?f=templates$fn=default.htm$3.0). [Accessed 16 08 2020].

- [85] "Eintragung zu Ethylenglykol in der GESTIS-Stoffdatenbank," Institut für Arbeitsschutz der Deutschen Gesetzlichen Unfallversicherung, [Online]. Available: [http://gestis.itrust.de/nxt/gateway.dll/gestis_de/012060.xml?f=template&fn=default.htm\\$3.0](http://gestis.itrust.de/nxt/gateway.dll/gestis_de/012060.xml?f=template&fn=default.htm$3.0). [Accessed 16 08 2020].
- [86] "Eintrag zu Natriumhydroxid in der GESTIS-Stoffdatenbank," Institut für Arbeitsschutz der Deutschen Gesetzlichen Unfallversicherung, [Online]. Available: [gestis.itrust.de/nxt/gateway.dll/gestis_de/001270.xml?f=template&fn=default.htm\\$3.0](http://gestis.itrust.de/nxt/gateway.dll/gestis_de/001270.xml?f=template&fn=default.htm$3.0). [Accessed 16 08 2020].
- [87] E. P. Management, "Conductance Data For Commonly Used Chemicals," ROSEMOUNT Analytical, 2010.
- [88] A. Ling-Wei Woo, PhD Thesis: Conductance Studies of Concentrated Solutions of Sodium Hydroxide and Potassium Hydroxide Electrolytes, South Dakota State University: Electronic Theses and Dissertations. 3516., 1968.
- [89] R. Analytical, "Conductance Data For Commonly Used Chemicals," EMERSON Process Management, USA, 2010.
- [90] C.-Y. K. a. W.-H. C. Ben-Zu Wan, "Kinetics of Depolymerization of Poly(ethylene terephthalate) in a Potassium Hydroxide Solution," *Industrial & Engineering Chemistry Research*, vol. 40, no. 2, pp. 509-514, 2001, doi: 10.1021/ie0005304.
- [91] S. H. Shahcheraghi, G. R. Khayati and M. Ranjbar, "An advanced reaction model determination methodology in solid-state kinetics based on Arrhenius parameters variation," *J Therm Anal Calorim*, vol. 122, pp. 175-188, 15 May 2015, doi: 10.1007/s10973-015-4708-8.
- [92] R. Hardis, J. L. P. Jessop, F. E. Peters and M. R. Kessler, "Cure kinetics characterization and monitoring of an epoxy resin using DSC, Raman spectroscopy, and DEA," *Composites Part A: Applied Science and Manufacturing*, vol. 49, no. A, pp. 100-108, 2013, doi: 10.1016/j.compositesa.2013.01.021.
- [93] C. R. Bagshaw, Order of Reaction. In: Roberts G.C.K. (eds) *Encyclopedia of Biophysics*, Berlin, Heidelberg: Springer, 2013, doi: 10.1007/978-3-642-16712-6_575.

- [94] K. J. Laidler, "The Development of the Arrhenius Equation," *Journal of Chemical Education*, vol. 61, no. 6, pp. 494-498, 1 June 1984, doi: 10.1021/ed061p494.
- [95] V. Ramopoulos, G. Link, S. Soldatov and J. Jelonnek, "Industrial scale microwave applicator for high temperature alkaline hydrolysis of PET," *International Journal of Microwave and Wireless Technologies*, vol. 10, no. 5-6, 22 May 2018, doi: 10.1017/S1759078718000727.
- [96] "Kunststoffedirekt; Technisches Datenblatt," [Online]. Available: <https://kunststoffedirekt.de/media/pdf/cf/1b/01/PET-Polyethylenterephthalat.pdf>. [Accessed 16 08 2020].
- [97] "Das Periodensystem der Elemente online; Natriumhydroxid, NaOH," [Online]. Available: <http://www.periodensystem-online.de/index.php?el=11&id=compound&cpid=917>. [Accessed 17 08 2020].
- [98] V. Józsa and R. Kovács, *Solving Problems in Thermal Engineering*, Switzerland: Springer, 2020, ISBN: 978-3-030-33474-1.
- [99] "www.mtc.de," Micro Tech Components GmbH, [Online]. Available: <https://www.mtc.de/en/emc-metal-parts/contact-springs#node-1109>. [Accessed 18 08 2020].
- [100] "RUBBER COMPOUNDS. SILICONE COMPOUNDS.," Gummiwerk Kraiburg GmbH & Co. KG, [Online]. Available: <https://www.kraiburg-rubber-compounds.com/produkte-maerkte/#1519383430331-f0456ef1-2180>. [Accessed 10 Januar 2020].
- [101] European Commission, "Winners of the 2018 Innovation Radar Prize," 12 December 2018. [Online]. Available: <https://ec.europa.eu/digital-single-market/en/news/winners-2018-innovation-radar-prize>. [Accessed 31 August 2020].
- [102] V. V. Daniel, *Dielectric relaxation*, London: Academic Press, 1967.

List of own publications

- [I] N. Li, G. Link, T. Wang, V. Ramopoulos, D. Neumaier, J. Hofele, M. Walter and J. Jelonnek, "Path-designed 3D printing for topological optimized continuous carbon fibre reinforced composite structures," *Composites Part B: Engineering*, vol. 182, 2020, doi: 10.1016/j.compositesb.2019.107612.
- [II] V. Ramopoulos, S. Soldatov, G. Link and J. Jelonnek, "Dielectric Measurements Setup of Double Layer Laminates," In Proc. 17th International Conference on Microwave and High Frequency Heating AMPERE 2019, 9-12 September 2019.
- [III] V. Ramopoulos, S. Soldatov, G. Link and J. Jelonnek, "Test Set for Dielectric Measurements of Double Layer Laminates," In Proc. 53ST Annual Microwave Power Symposium (IMPI 53), 18-20 June 2019.
- [IV] V. Ramopoulos, G. Link, S. Soldatov and J. Jelonnek, "Modular Microwave Applicator Design for Homogeneous Heating of Tubular Chemical Reactors at Industrial Scale," In Proc. Progress In Electromagnetics Research Symposium (PIERS), 1-4 August 2018.
- [V] S. Soldatov, G. Link, D. Neumaier, V. Ramopoulos and J. Jelonnek, "Investigation on Orthogonal Antenna Configurations for Large Scale Microwave Ovens," In Proc. 52ST Annual Microwave Power Symposium (IMPI 52), 26-28 June 2018.
- [VI] V. Ramopoulos, G. Link, S. Soldatov and J. Jelonnek, "Industrial scale microwave applicator for high temperature alkaline hydrolysis of PET," *International Journal of Microwave and Wireless Technologies*, vol. 10, no. 5-6, 22 May 2018, doi: 10.1017/S1759078718000727.
- [VII] G. Link and V. Ramopoulos, "Simple Analytical Approach for Industrial Microwave Applicator Design," In special issue on *Chemical Engineering & Processing: Process Intensification*, vol. 125, pp. 334-342, March 2017, doi: 10.1016/j.cep.2017.12.015.
- [VIII] V. Ramopoulos, G. Link, S. Soldatov and J. Jelonnek, "Industrial Scale Microwave Applicator for High Temperature Alkaline Hydrolysis of PET," 2017 47th European Microwave Conference

- (EuMC), pp. 930-933, 10-12 Oct. 2017, doi: 10.23919/EuMC.2017.82309.
- [IX] V. Ramopoulos, G. Link, S. Soldatov and J. Jelonnek, "Development of an Advanced Microwave Calorimeter for Monitoring of Chemical Reactions," In Proc. 51ST Annual Microwave Power Symposium (IMPI 51), 20-22 June 2017.
- [X] V. Ramopoulos, G. Link, S. Soldatov, T. Spira and J. Jelonnek, "Advanced Dual-Mode Resonator for In-Situ Dielectric Measurements of Lossy Materials," In Proc. 3rd Global Congress on Microwave Energy Applications, 25-29 July 2016.
- [XI] G. Link, V. Ramopoulos and J. Jelonnek, "Principles of design for industrial microwave applicators," In Proc. 15th International Conference on Microwave and High Frequency Heating, 14-17 September 2015.
- [XII] S. Betz, F. Köster and V. Ramopoulos, "Energy and Time Efficient Microwave Curing for CFRP Parts Manufactured by Filament Winding," Material Science Forum, Vols. 825-826, pp. 741-748, July 2015, doi: 10.4028/www.scientific.net/MSF.825-826.741.
- [XIII] V. Ramopoulos, S. Soldatov, G. Link, T. Kayser, M. Gehringer and J. Jelonnek, "Microwave system for in-situ dielectric and calorimetric measurements in a wide temperature range using a TE₁₁₁-mode cavity," 2015 IEEE MTT-S International Microwave Symposium, pp. 1-4, 17-22 May 2015, doi: 10.1109/MWSYM.2015.7166906.
- [XIV] V. Ramopoulos, S. Soldatov, G. Link, T. Kayser and J. Jelonnek, "System for in-situ dielectric and calorimetric measurements during microwave curing of resins," 2015 German Microwave Conference, pp. 29-32, 16-18 March 2015, doi: 10.1109/GEMIC.2015.7107744.
- [XV] V. Ramopoulos, S. Soldatov, G. Link, T. Kayser and J. Jelonnek, "Design and Development of a System for In-Situ Dielectric and Calorimetric Measurements during Microwave curing of Resins," In Proc. 16th Seminar Computer Modeling in Microwave Power Engineering, May 2014.

Acknowledgment

The presented work was performed during my time as research assistant at the Institute for Pulsed Power and Microwave Technology (IHM) at the Karlsruhe Institute of Technology (KIT). First of all I would like to thank Prof. Dr.-Ing. John Jelonnek for giving me the opportunity to contribute to the very exciting research on material process technology with microwaves and for his steady support at the Institute for Pulsed Power and Microwave Technology (IHM) at KIT. Moreover, due to the continuous and intensive support he has given me during my work at the institute. Sincere thanks also to Prof. Dr.-Ing. Thorsten Gerdes for volunteering as Co-Referee of this thesis. I would like to express my deep gratitude to Prof. Dr. rer. nat. Dr. h.c. Manfred Thumm for the supportive and motivating involvement in my work.

I am furthermore grateful to Dr. Guido Link and Dr. Sergey Soldatov for their continuous support, constructive comments and advices during my PhD work. Many thanks to Paolo Stefano Care, Julia Hofele, Dominik Neumaier, Dr. Benjamin Lepers, Dr. Thorsten Kayser, Dr. Chuanren Wu, Dr. Sebastian Ruess, Dr. Parth Kalaria, Dr. Joachim Franck and Dr. Nanya Li without our discussions and our friendship, this thesis would have been much more difficult to write.

Furthermore I would like to warmly thank to Volker Nuss, Thomas Seitz and Stefan Layer for technical discussions and manufacturing of the experimental set-up. Without their support, all the experiments would not be possible. To Martina Huber, Melanie Mai and Kevin Paulus for their administrative and technical support. Thanks also go to all other IHM colleagues for the friendly and collegial atmosphere at our institute. A big thanks goes to my parents for their continuous support in all phases of my life. Many thanks also to my sister and her wonderful family for the great times and motivating support.

- Band 1 **MATTHIAS BERINGER**
Design Studies towards a 4 MW 170 GHz Coaxial-Cavity Gyrotron.
ISBN 978-3-86644-663-2
- Band 2 **JENS FLAMM**
Diffraction and Scattering in Launchers of
Quasi-Optical Mode Converters for Gyrotrons.
ISBN 978-3-86644-822-3
- Band 3 **MATTIA DEL GIACCO**
Investigation of Fretting Wear of Cladding Materials in Liquid Lead.
ISBN 978-3-86644-960-2
- Band 4 **AMITAVO ROY CHOUDHURY**
Investigations of After Cavity Interaction in Gyrotrons
Including the Effect of Non-uniform Magnetic Field.
ISBN 978-3-7315-0129-9
- Band 5 **MICHAEL BETZ**
The CERN Resonant WISP Search (CROWS).
ISBN 978-3-7315-0199-2
- Band 6 **ANDREAS SCHLAICH**
Time-dependent spectrum analysis of high power gyrotrons.
ISBN 978-3-7315-0375-0
- Band 7 **DHIDIK PRASTIYANTO**
Temperature- and Time-Dependent Dielectric Measurements
and Modelling on Curing of Polymer Composites.
ISBN 978-3-7315-0424-5
- Band 8 **YIMING SUN**
Adaptive and Intelligent Temperature Control of Microwave
Heating Systems with Multiple Sources.
ISBN 978-3-7315-0467-2

- Band 9 **JIANGHUA ZHANG**
Influence of Emitter surface roughness and Emission inhomogeneity
on Efficiency and stability of high power Fusion gyrotrons.
ISBN 978-3-7315-0578-5
- Band 10 **ANTON MALYGIN**
Design and Experimental Investigation of a Second Harmonic 20 kW Class
28 GHz Gyrotron for Evaluation of New Emitter Technologies.
ISBN 978-3-7315-0584-6
- Band 11 **JOACHIM FRANCK**
Systematic Study of Key Components for a Coaxial-Cavity
Gyrotron for DEMO.
ISBN 978-3-7315-0652-2
- Band 12 **PARTH CHANDULAL KALARIA**
Feasibility and Operational Limits for a 236 GHz Hollow-Cavity
Gyrotron for DEMO.
ISBN 978-3-7315-0717-8
- Band 13 **CHUANREN WU**
Conceptual Studies of Multistage Depressed Collectors for Gyrotrons.
ISBN 978-3-7315-0934-9
- Band 14 **MARTIN HOCHBERG**
A high-voltage pulsed power modulator
for fast-rising arbitrary waveforms.
ISBN 978-3-7315-0958-5
- Band 15 **SEBASTIAN RUESS**
Pushing the KIT 2 MW Coaxial-Cavity Short-Pulse
Gyrotron Towards a DEMO Relevant Design.
ISBN 978-3-7315-1024-6
- Band 16 **VASILEIOS RAMOPOULOS**
Energy-efficient, scalable and modular industrial microwave
applicator for high temperature alkaline hydrolysis of PET.
ISBN 978-3-7315-1099-4



Karlsruher Forschungsberichte aus dem
Institut für Hochleistungsimpuls- und Mikrowellentechnik

Herausgeber: Prof. Dr.-Ing. John Jelonnek

By using microwave heating, the alkaline hydrolysis of polyethylene terephthalate (PET) can be significantly accelerated from about 3 hours to less than 10 minutes, while the reaction takes place at lower temperatures under microwave conditions. However, the benefits have only been demonstrated on a laboratory scale to date. This has led to the need to develop a suitable industrial microwave reactor to enable industrial application of this reaction. For the first time, this work presents a novel industrial microwave applicator at 2.45 GHz with homogeneous distribution to support the alkaline hydrolysis of PET, which allows an efficient and continuous operation. In addition, an innovative dielectric and calorimetric measurements setup is presented. Furthermore, the modelling of the reaction kinetics based on the measured dielectric parameters is presented.

Vasileios Ramopoulos received the B. Eng. degree from Karlsruhe Institute of Technology (KIT) in 2012 and the M.Sc. degree from Karlsruhe Institute of Technology (KIT) in 2014. In 2014, he joined the Institute for Pulsed Power and Microwave Technology (IHM) as a research assistant, where he finished his work in 2021.

ISSN 2192-2764

ISBN 978-3-7315-1099-4

